ISTANBUL TECHNICAL UNIVERSITY ★ GRADUATE SCHOOL

SYNTHESIS OF THIENOTHIOPHENE BASED MATERIALS AND INVESTIGATION OF THEIR ELECTRONIC AND OPTOELECTRONIC PROPERTIES

M.Sc. THESIS

Esra SAHIN

Department of Chemistry

Chemistry Programme

AUGUST 2025

ISTANBUL TECHNICAL UNIVERSITY ★ GRADUATE SCHOOL

SYNTHESIS OF THIENOTHIOPHENE BASED MATERIALS AND INVESTIGATION OF THEIR ELECTRONIC AND OPTOELECTRONIC PROPERTIES

M.Sc. THESIS

Esra SAHIN
(509231258)

Department of Chemistry

Chemistry Programme

Thesis Advisor: Prof. Dr. Turan OZTURK

AUGUST 2025

ISTANBUL TEKNİK ÜNİVERSİTESİ ★ LİSANSÜSTÜ EĞİTİM ENSTİTÜSÜ

TİYENOTİYOFEN BAZLI MALZEMELERİN SENTEZİ VE ELEKTRONİK VE OPTOELEKTRONİK ÖZELLİKLERİNİN ARAŞTIRILMASI

YÜKSEK LİSANS TEZİ

Esra ŞAHİN
(509231258)

Kimya Anabilim Dalı

Kimya Programı

Tez Danışmanı: Prof. Dr. Turan ÖZTÜRK

AĞUSTOS 2025

Esra Sahin, a M.Sc. student of ITU Graduate School student ID 509231258, successfully defended the thesis entitled “SYNTHESIS OF THIENOTHIOPHENE BASED MATERIALS AND INVESTIGATION OF THEIR ELECTRONIC AND OPTOELECTRONIC PROPERTIES”, which she prepared after fulfilling the requirements specified in the associated legislations, before the jury whose signatures are below.

Thesis Advisor :	**Prof. Dr. Turan OZTURK** İstanbul Technical University	.....
Jury Members :	**Assoc. Prof. Dr. Abdullah AYDOGAN** Istanbul Technical University	.....
	Prof. Dr. Mehmet S. EROGLU Marmara University	.....

Date of Submission : 5 August 2025
Date of Defense : 20 August 2025

To my mom,

FOREWORD

First and foremost, I would like to express my sincere gratitude to Prof. Dr. Turan OZTURK for giving me the opportunity to work in his research group and for all the inspiration, advice, endless support, and everything he taught me. I am truly grateful to have been able to work with him.

I would like to express my deepest thanks to Assoc. Prof. Dr. Erdal ERTAS for his valuable guidance, motivation, and contributions to my academic development throughout my graduate education.

I would like to express my thanks to Dr. Recep ISCI, who has become a mentor to me. I am so thankful to him for his guidance, encouragement, invaluable assistance and friendship at every step of this journey.

I would also like to thank my friends and coworkers, Serra Ebru OZTURK, Asena KASIKCI, Dilara GUNTURKUN ISCI, Emine Busra KUCUK, Melis UNAL, Golfamsadat HODA, Onuralp DENIZOGLU, Levent Bugra BOL, and the all research group members for their kind help and friendship.

I would like to thank my beloved friends Ilkem and Zeynep for always being there whenever I needed them. I am so grateful to have them in my life. Furthermore, I am also grateful to Nursima, Hasret, Ragıp, Banu, Fatma, Elif Nur, Aysenur, Busra, Rıdvan, Feyzanur and all my friends, whose names I can't mention, for their support, valuable friendships, and making my university years bearable. Thank you for being my friends.

I would also like to thank Prof. Dr. Mehmet EROGLU, Dr. Koray B. DONMEZ, and Dr. Armagan ATSAY for the assistance they provided and contributions to my thesis.

I would like to thank the Scientific and Technological Research Council of Turkey (TÜBİTAK) (Projects No. 122Z568 and 124Z353), the Research Fund of Istanbul Technical University (ITU BAP) (Projects No. TYLB-2023-45051 and TGA-2023-45124), and Unsped Global Lojistik, Turkey, for their financial support.

Lastly and most importantly, I would like to express my endless thanks to my mom, Kevser SAHIN, who never lost her trust and belief in me for even a second in her life, and who stood behind every decision I made. I couldn't have accomplished any of this without her. I am also grateful to my father, Ziver SAHIN, my brothers Emin and Muhammed SAHIN for making me the person I am today. I will always remember their love and support.

Finally, to my cat Tursu, thank you for reminding me to pause, stretch, and occasionally delete entire paragraphs with a single paw. Your presence made even the most stressful moments bearable. I'm so grateful to have you.

August 2025

Esra SAHIN
(Chemist)

TABLE OF CONTENTS

Page

ABBREVIATIONS

ACN : Acetonitrile
AFM : Atomic Force Microscopy
BET : Brunauer–Emmett–Teller (BET) Theory
$CDCl_3$: Deuterated Chloroform
CV : Cyclic Voltammetry
DCM : Dichloromethane
DMF : N,N-Dimethylformamide
EDOT : 3,4-Ethylenedioxythiophene
EIS : Electrochemical Impedance Spectrometry
Et_2O : Diethyl Ether
$FeCl_3$: Iron(III)chloride
GCE : Glassy Carbon Electrode
GDC : Galvanostatic Charge Discharge
H_3PO_4 : Phosphoric Acid
HCl : Hydrochloric Acid
HOMO : Highest Occupied Molecular Orbital
ICT : Intramolecular Charge Transfer
K_2CO_3 : Potassium carbonate
KOH : Potassium hydroxide
LDA : Lithium diisopropylamide
LUMO : Lowest Unoccupied Molecular Orbital
MeOH : Methanol
NBS : N-Bromosuccinimide
***n*-BuLi** : *n*-Butyllithium
NMR : Nuclear Magnetic Resonance
OFET : Organic Field Effect Transistor
OLED : Organic Light Emitting Diode
OPV : Ogranic Photovoltaic
OSC : Organic Semiconductor
OTFT : Organic Thin Film Transistor

$P(o\text{-}tol)_3$: Tri(o-tolyl)phosphine

PCE : Power Conversion Efficiency

$Pd(PPh_3)_4$: Tetrakis(triphenylphosphine)palladium(0)

$Pd_2(dba)_3$: Tris(dibenzylideneacetone)dipalladium(0)

POP : Porous Organic Polymer

PPA : Polyphosphoric Acid

S_8 : Elementary Sulfur

SEM : Scanning Electron Microscope

SWCNT : Single-Walled Carbon Nanotube

$TBAPF_6$: Tetrabutylammonium hexafluorophosphate

TGA : Thermogravimetric Analysis

Th : Thiophene

THF : Tetrahydrofuran

TMEDA : N,N,N',N',-Tetramethylethylenediamine

TMS : Tetramethylsilane

TPA : Triphenylamine

TT : Thienothiophene

UV-Vis : Ultraviolet-Visible

SYMBOLS

°C	**:** Degree Celsius
A	**:** Ampere
Å	**:** Angstrom
C	**:** Capacitance
cm^2	**:** Centimeter Square
E_{elec}	**:** Electronic Band Gap
E_g	**:** Band Gap
$E_{onset, ox}$	**:** Oxidaiton Onset Potential
E_{opt}	**:** Optic Band Gap
E_{ox}	**:** Oxidaiton Potential
eV	**:** Electron Volt
F	**:** Farad
h	**:** Hour
Hz	**:** Frequency
I	**:** Current
kg	**:** Kilogram
m^2	**:** Meter Square
mg	**:** Miligram
nm	**:** Nanometer
P	**:** Pressure
R	**:** Resistance
s	**:** Second
T	**:** Temperature
t	**:** Time
V	**:** Potential
W	**:** Watt
λ	**:** Wavelength
µm	**:** Micrometer

LIST OF TABLES

Page

LIST OF FIGURES

Page

SYNTHESIS OF THIENOTHIOPHENE BASED MATERIALS AND INVESTIGATION OF THEIR ELECTRONIC AND OPTOELECTRONIC PROPERTIES

SUMMARY

Conjugated organic materials have emerged as key components in the development of next-generation optoelectronic devices, including organic photovoltaics (OPVs), organic light-emitting diodes (OLEDs), organic field-effect transistors (OFETs), supercapacitors, and various sensor systems. Among π-conjugated building blocks, thiophene and its derivatives have shown outstanding performance due to their structural tunability, high electron density, excellent thermal stability, and ease of functionalization. Thienothiophenes (TTs), particularly the thieno[3,2-*b*]thiophene isomer, represent one of the most rigid and planar π-extended fused thiophene systems. Their flat molecular structure enhances π–π stacking interactions, reduces band gaps, and improves charge transport characteristics, making them ideal scaffolds for organic semiconductor design.

In this study, two novel TT-based π-conjugated molecules were designed and synthesized: TT-Th3-TPA3 and TT-EDOT3-TPA3. These molecules contain triphenylamine (TPA) and 3,4-ethylenedioxythiophene (EDOT) moieties as electron-donating groups, which are introduced by Suzuki and Stille cross-coupling processes, respectively. To further enhance their processability and electrochemical performance, TT-based π-systems were hybridized with single-walled carbon nanotubes (SWCNTs) through non-covalent interactions, yielding binder-free, flexible hybrid films. Additionally, TT's polymeric analogs were synthesized via Stille coupling and electropolymerization strategies.

All synthesized materials were thoroughly characterized using various techniques. Monomer structural characterization was achieved by ^{1}H NMR spectroscopy, while optic properties were studied using UV-Vis and fluorescence spectroscopy. Cyclic voltammetry (CV) was used to analyze electrochemical behaviors, while SEM and AFM were used to investigate morphological characteristics. The TT-based molecules, TT-Th3-TPA3 and TT-EDOT3-TPA3, exhibited strong light absorption in the visible region, significant bathochromic shifts, and relatively low optical band gaps (2.33 and 2.36 eV, respectively), along with large Stokes shifts.

Electrochemical polymerization of TT-Th in an optimal potential window (0.0–1.6 V) successfully yielded stable polymer films with significantly enhanced electrochemical activity. Subsequent CV analysis revealed that although the redox process involves a measurable diffusion-controlled contribution, the strong linearity of log(current) vs. log(scan rate) plots, with slopes close to unity, confirms that the charge storage mechanism is predominantly surface-controlled and capacitive in nature. These findings highlight the polymer film's potential for high-rate energy storage applications. Furthermore, P(TT-EDOT) exhibited a high BET surface area of 152 m^2/g and uniform microporosity, supported by its rough, porous morphology observed

in SEM images, indicating its suitability for applications requiring efficient ion transport, such as supercapacitors or sensing systems.

Hybrid films based on TT and SWCNTs were evaluated for supercapacitor applications. The electrochemical studies showed high specific capacitance, low internal resistance, and excellent charge-discharge cycling stability, confirming their suitability for energy storage devices. In particular, TT-EDOT3-TPA3–SWCNT films demonstrated superior performance, attributed to the enhanced π-electron delocalization and strong interfacial interactions with the nanotubes. Furthermore, TT-EDOT3-TPA3–SWCNT film thermal analysis revealed high stability, with decomposition temperatures above 400°C.

This research highlights the promising role of TT-based π-conjugated systems in the field of organic electronics. The successful synthesis of functionalized TT-derivatives and their integration into hybrid nanostructures and porous organic polymers provides a versatile platform for applications in optoelectronics and energy storage technologies. These findings contribute to the further development of high-performance, solution-processable organic semiconductors.

TİYENOTİYOFEN BAZLI MALZEMELERİN SENTEZİ VE ELEKTRONİK VE OPTOELEKTRONİK ÖZELLİKLERİNİN ARAŞTIRILMASI

ÖZET

Organik yarıiletkenler (OSC'ler), π-konjuge sistemler içeren karbon bazlı küçük moleküller veya polimerlerdir. Bu yapı, elektronların molekül boyunca delokalize olmasına olanak tanıyarak yarıiletken davranış sergilemelerini sağlar. Mekanik esneklik, düşük üretim maliyeti, kimyasal olarak modifiye edilebilme ve çözelti bazlı işlenebilirlik gibi avantajları sayesinde, son yıllarda elektronik, optoelektronik ve enerji depolama teknolojilerinde büyük ilgi görmektedirler. Yük taşıma kapasiteleri, π-konjugasyonun sağladığı geniş delokalizasyon ile doğrudan ilişkilidir. OSC'ler; fotovoltaik hücreler, organik alan etkili transistörler (OFET), elektrokromik cihazlar ve süperkapasitörler gibi birçok uygulama için umut vadeden malzemelerdir. Bu nedenle, yapı–özellik ilişkilerinin anlaşılması ve yeni fonksiyonel yapıların tasarlanması, hem temel bilimsel çalışmalar hem de teknolojik uygulamalar açısından büyük önem taşımaktadır.

Bu yüksek lisans tezinde, organik yarı iletken özellik gösteren yeni konjuge malzemelerin tasarımı ve sentezi gerçekleştirilmiş; bu malzemelerin elektronik ve optoelektronik uygulamalardaki potansiyelleri detaylı olarak araştırılmıştır. Çalışmanın ana amacı, tiyenotiyofen (TT) temel yapısını içeren yeni organik moleküllerin ve polimerlerin geliştirilerek, bu yapıların enerji depolama ve iletim özellikleri açısından performanslarının ortaya konulmasıdır. Tiyenotiyofen yapısı, düzlemsel ve rijit konfigürasyonu, geniş π-konjugasyonu, elektronca zengin karakteri ve kimyasal kararlılığı ile dikkat çeken bir çekirdek yapı olup, özellikle düşük band aralığına sahip yarı iletkenlerin tasarımında yaygın olarak kullanılmaktadır.

Çalışmanın ilk bölümünde, tiyenotiyofen çekirdekli hedef moleküllerin sentezi gerçekleştirilmiştir. Bu kapsamda, tiyeno[3,2-*b*]tiyofen izomeri üzerine yapılandırılmış üçlü bromlanmış ara bileşik 5 sentezlenmiş ve bu yapı üzerinden iki farklı son ürün hazırlanmıştır. Suzuki çapraz kenetlenme reaksiyonu ile TT-Th$_3$-TPA$_3$ bileşiği elde edilmiştir. Aynı şekilde, Stille çapraz bağlama reaksiyonu ile TT-EDOT$_3$-TPA$_3$ yapısı hazırlanmıştır. Her iki yapı da, yoğun π-konjugasyonlu sistemler olarak tasarlanmış ve hem optik hem de elektroaktif özellikler sergileyecek şekilde geliştirilmiştir.

Sentezlenen bu monomerik yapıların yanında, polimerik yapılar da sentezlenerek elde edilen yapının işlenebilirliğinin ve iletkenliğinin arttırılması hedeflenmiştir. Stille polimerizasyonu kullanılarak TT-Th ile EDOT ünitelerinin çapraz bağlanması ile yeni bir polimer yapı olan P(TT-EDOT) elde edilmiştir. Bu yapının yanında, yine TT-Th ünitesi kullanılarak elektropolimerizasyon tekniği ile de polimer film oluşturulmuş ve bu filmin karakterizasyonu yapılmıştır.

Bu çalışmanın önemli bir diğer boyutu ise, sentezlenen π-konjuge moleküllerin tek duvarlı karbon nanotüpler (SWCNT) ile etkileştirilmesi yoluyla hibrit sistemlerin

geliştirilmesidir. Özellikle SWCNT'lerin yüksek yüzey alanı, mükemmel elektriksel iletkenliği ve mekanik dayanıklılığı sayesinde, TT-Th3-TPA3 ve TT-EDOT3-TPA3 yapılarla fiziksel olarak birleştirilerek esnek ve bağlayıcı içermeyen hibrit filmler elde edilmiştir. Bu nanohibrit yapıların hazırlanmasında, çözeltide uzun süreli karıştırma ve ultrasonikasyon gibi non-kovalent fonksiyonelleştirme yöntemleri kullanılmıştır. Bağlayıcı içermeyen bu sistemler, daha düşük direnç, daha yüksek iletkenlik ve homojen dağılım gibi avantajlara sahiptir.

Yapılan sentezlerin ardından, elde edilen tüm yapılar çok yönlü karakterizasyon teknikleri ile analiz edilmiştir. Proton NMR spektroskopisi ile yapısal doğrulama yapılmış; UV-Vis spektroskopisi ile absorpsiyon karakteristikleri belirlenmiş; floresans spektroskopisi ile emisyon ilişkisi incelenmiştir. Elektrokimyasal davranışlar, döngülü voltametri (CV) kullanılarak değerlendirilmiş, HOMO-LUMO enerji düzeyleri tahmin edilmiş ve redoks özellikleri gözlemlenmiştir. Ayrıca, termogravimetrik analiz (TGA) ile bileşiklerin ve hibrit filmlerin ısıl dayanıklılıkları ölçülmüş, elde edilen polimer ve hibrit filmlerin yüzey morfolojileri ise SEM, BET ve AFM analizleriyle incelenmiştir.

Elde edilen hibrit filmlerin enerji depolama alanındaki uygulama potansiyelleri, özellikle süperkapasitör cihazlarında test edilmiştir. Bu amaçla CV, galvanostatik şarj-deşarj (GCD) ve elektrokimyasal empedans spektroskopisi (EIS) gibi yöntemlerle özgül kapasitans, enerji yoğunluğu, güç yoğunluğu ve döngüsel kararlılık gibi parametreler incelenmiştir. CV analizleri, elektrotların hızlı yük-boşaltma döngülerine adapte olabildiğini göstermiştir. GCD sonuçları, uzun süreli kullanımda performans kaybının oldukça düşük olduğunu ortaya koymuştur. EIS ölçümleri ise elektrot-elektrolit arayüzünün düşük direnç gösterdiğini ve yüksek iletim kapasitesine sahip olduğunu doğrulamıştır.

Sonuçlar, sentezlenen TT-tabanlı yapılar ve bu yapıların hibrit formlarının hem optik hem de elektroaktif özellikler bakımından oldukça başarılı olduğunu göstermektedir. TT-Th3-TPA3 yapısı nispeten daha yüksek HOMO düzeylerine sahipken, TT-EDOT3-TPA3 bileşiği daha düşük optik band aralığı ile dikkat çekmektedir. Her iki yapı da, elektron verici gruplar içermesi sebebiyle yük taşınımını kolaylaştırmakta ve yüksek iletkenlik değerleri sergilemektedir. Ayrıca, karbon nanotüpler ile oluşturulan hibrit filmler, esneklikleri ve mekanik dayanıklılıkları sayesinde uygulama alanında önemli avantajlar sunmaktadır. Elde edilen özgül kapasitans değerleri literatürdeki benzer yapılardan daha yüksek olup, bu durum geliştirilen yapıların süperkapasitör elektrotu olarak kullanılabilirliğini desteklemektedir.

Bu tez çalışması, tiyenotiyofen (TT) çekirdeği temelinde tasarlanan yeni π-konjuge sistemlerle, organik elektronik ve enerji depolama teknolojilerinde kullanılabilecek yüksek performanslı malzemelerin geliştirilmesine katkı sunmaktadır. Fonksiyonelleştirilmiş TT türevlerinin başarıyla sentezlenmesi ve bu yapıların tek duvarlı karbon nanotüplerle (SWCNT) hibrit nanoyapılara ve gözenekli organik polimerlere entegre edilmesi, hem temel bilimsel bilgiye katkı sağlamakta hem de uygulamaya yönelik çok yönlü ve esnek bir platform sunmaktadır. Geliştirilen bu malzemeler, özellikle organik ışık yayan diyotlar (OLED), organik alan etkili transistörler (OFET), organik güneş pilleri (OPV) ve süperkapasitörler gibi cihazlarda kullanılabilecek potansiyele sahiptir. Ayrıca bağlayıcı içermeyen hibrit yapıların esnek ve hafif olması, bu malzemeleri giyilebilir elektronik ve taşınabilir enerji sistemleri gibi modern teknolojilere uyumlu hâle getirmektedir. Elde edilen bulgular, çözeltiyle

işlenebilir organik yarıiletkenlerin geliştirilmesine yönelik önemli bir adım niteliğindedir.

Gelecekteki çalışmalar, bu materyallerin farklı cihaz mimarilerinde doğrudan uygulanması ve performanslarının optimize edilmesi üzerine odaklanabilir. Ayrıca, farklı elektron donör veya akseptör gruplarının TT iskelelerine entegre edilmesiyle, optik ve elektrokimyasal özelliklerin daha da ayarlanabilmesi mümkündür. Hibrit materyallerin uzun dönemli kararlılıkları ve üretim ölçeklenebilirliği gibi pratik konular da gelecekteki araştırmaların önemli odak noktaları olabilir. Bu araştırmalar, organik elektronik alanında daha yenilikçi ve yüksek performanslı cihazların geliştirilmesine zemin hazırlayacaktır.

1. INTRODUCTION

1.1 Organic Semiconductors

Organic semiconductors (OSCs) are π-conjugated organic materials that exhibit electrical conductivities between those of metals and insulators, typically ranging from 10^{-9} to 10^{3} $S \cdot cm^{-1}$. The discovery of photoconduction in solid anthracene in 1906 marked the first study on the conductivity of organic compounds [1]. Since then, OSCs have gained significant attention due to their promising charge transport and electroluminescent properties, making them ideal for use in various organic and hybrid electronic devices such as organic photovoltaic cells (OPVs), organic light-emitting diodes (OLEDs), capacitors, and organic field-effect transistors (OFETs). Over the past decade, the development of high-performance OSCs for applications in plastic electronics has become one of the most dynamic areas of research [1,2]. These materials can be categorized as small molecules or conjugated polymers, both containing delocalized π-electron systems formed by the p_z-orbitals of sp^2-hybridized carbon atoms. The energy difference between the highest occupied molecular orbital (HOMO) and the lowest unoccupied molecular orbital (LUMO), known as the band gap, typically ranges from 1.5 to 3 eV and determines the material's light absorption and emission properties. This gap, which is similar to the valence and conduction bands in inorganic semiconductors, is extremely dependent on molecule conjugation length, packing, and alignment. Furthermore, the choice between small molecules and conjugated polymers significantly affects processing strategies and film morphology, which in turn influence charge transport. Understanding and controlling these structural and electronic parameters is essential for optimizing organic semiconductor performance in optoelectronic devices such as OLEDs, OFETs and OPVs [3,4].

1.2 Conjugated π-Systems

Conjugation refers to the alternating arrangement of single and double bonds within a molecule, resulting in a delocalized π-electron system. This system typically arises

from a backbone of sp^2-hybridized carbon atoms, where the p_z-orbitals are oriented perpendicular to the molecular plane and overlap to form an extended π-network. In such unsaturated structures, the presence of π-electrons facilitates charge delocalization, enabling efficient charge transport [5]**.** Traditionally regarded as insulators, polymers entered a new era in 1977 when Alan G. MacDiarmid, Hideki Shirakawa, and Alan J. Heeger discovered that the electrical conductivity of polyacetylene dramatically increased upon doping—reaching values as high as 10^3 S/cm. This breakthrough challenged conventional thinking and sparked intensive research into conducting polymers. This milestone, later honored with the Nobel Prize in Chemistry in 2000, paved the way for the development of various stable conducting polymers—including polypyrrole (PPy), polythiophene (PTh), polyaniline (PANI), poly(phenylenevinylene) (PPV), poly(para-phenylene) (PPP), and polyfuran (PF)—between the late 1970s and early 1980s [6–8]. Organic conjugated materials include both polymers and small π-conjugated molecules, such as oligomers with defined chain lengths (Figure1.1). These structures differ in terms of molecular weight, processing methods, and degrees of order, yet all derive their semiconducting behavior from conjugation [9]. π-conjugated small molecules, oligomers and polymers with planar backbones have attracted considerable interest due to their tunable electronic properties and potential applications in a variety of optoelectronic devices, including OLEDs, OFETS, OTFTs, and OPVs [9–11].

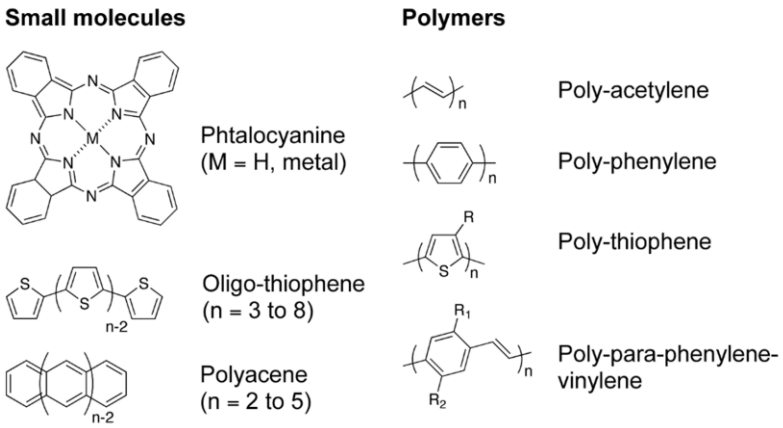

Figure 1.1 : Some examples of conjugated small molecules and polymers.

1.3 Electronic Conductivity and Band Gap in π-Conjugated Systems

Materials are classified as conductors, semiconductors, and insulators based on their ability to carry electricity. Insulators have no ability to conduct electric current,

whereas conducting materials have quite high conductivity. Depending on the circumstances, semiconductor materials have the ability to both conduct and block electricity. Figure 1.2 shows that conjugated polymers exhibit a broad conductivity range, which is influenced by their type and doping level [12].

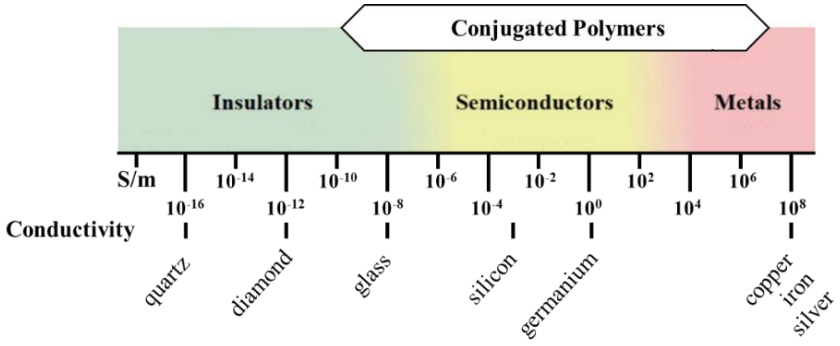

Figure 1.2 : Conductivity range of conjugated polymers.

The band gap (E_g) of a material is defined as the energy difference between HOMO and the LUMO, and is typically reported in electronvolt (eV). E_g and the location of the highest occupied and lowest unoccupied bands are essential properties of semiconductor materials. The HOMO and LUMO, respectively, bands are known as the valence and conduction bands in inorganic semiconductors. [13–15]. The difference in band gap sizes between conductors, semiconductors, and insulators are shown in Figure 1.3. Conductors do not have a band gap since their valence and conduction bands overlap. However, in insulators, the band gap between the valence and conduction bands is so high that electrons are unable to transfer energy from the valence to the conduction band. Furthermore, semiconductors have a small energy gap between their valence and conduction bands. Electrons can jump from valence band to conduction band, although not as easily as they can in conductors.

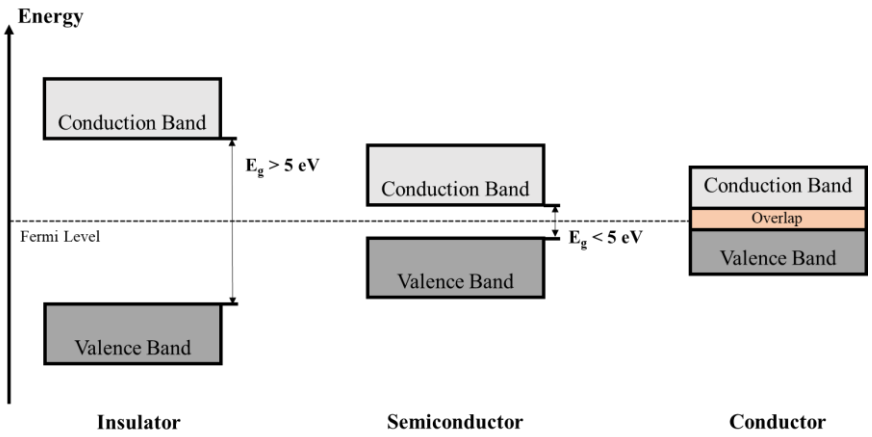

Figure 1.3 : Band energy diagram of insulators, semiconductors and conductors.

The ability to adjust the band gap and position of HOMO and LUMO levels by using synthetic routes depending on the proper molecular design is one of the advantages of semiconducting polymers. In contrast to inorganic semiconductors, the electrical and optical characteristics of polymeric semiconductors can be significantly changed by small alterations in their chemical structure [16–18].

1.4 Thienothiophenes

The simplest fused ring oligothiophene is thienothiophene (TT), which contains two thiophene units and has 4 structural isomers (Figure 1.4). These are: thieno[2,3-*b*]thiophene (1), thieno[3,2-*b*]thiophene (2), thieno[3,4-*b*]thiophene (3), thieno[3,4-*c*]thiophene (4). Thieno[3,2-*b*]thiophene (2) and thieno[3,4-*b*]thiophene (3) provide conjugated systems with low band gaps, but thieno[2,3-*b*]thiophene (1) gives a cross-conjugated system that cuts the conjugation and expands the band gap. The least stable isomer, which is thieno[3,4-*c*]thiophene (4), formed by two equivalent thiophene rings sharing a 3,4-bond, has a narrow HOMO-LUMO range and is unstable. Among these 4 isomers, the order of stability is 1 ≈ 2 > 3 > 4. The other three isomers are stable compounds and the chemistry of these compounds has been studied for many years [19, 20].

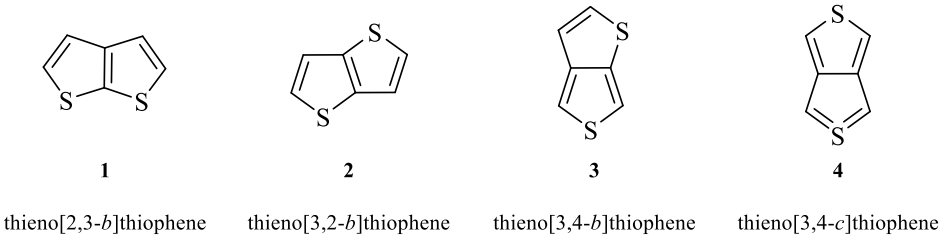

Figure 1.4 : Isomers of thienothiophenes.

Compared to thiophenes, fused thiophenes have more rigid structures with an extended π-conjugation. This might be used to increase intermolecular interactions in the solid state and change the band gap of organic materials. Because of their electron-rich structures, TTs can create conjugated organic semiconductors with narrow band gaps. Thieno[3,2-*b*]thiophene's flat, good electron delocalized skeleton, rigidity, electron-rich structure, intermolecular S···S interactions, and chemical stability have made it a valuable building block of many conjugated polymers in organic materials. Consequently, its electron-rich properties make TT a promising candidate for the development of conjugated polymers with low band gaps, which are crucial for

applications in energy-related fields such as organic solar cells, OLEDs, OFETs and capacitors [21–34].

1.5 3,4-Ethylenedioxythiophene

3,4-Ethylenedioxythiophene (EDOT) is a widely studied electron-rich monomer and a prominent representative of thiophene-based heterocyclic compounds (Figure 1.5). As a derivative of thiophene, it features a fused ethylenedioxy group, which enhances both its electronic conjugation and structural stability. The oxygen atoms in the ethylenedioxy ring increase the electron density on the thiophene core, thereby strengthening its electron-donating character. The rigid and planar nature of EDOT also promotes close packing and efficient π–π stacking interactions in the solid state, which facilitates improved charge transport. Thanks to its unique electronic structure and high reactivity, EDOT has become a key and widely adaptable unit in the molecular design of functional π-conjugated systems with tunable electrochemical and optical stability, conductivity and lower band gap properties. These features make EDOT-based materials highly attractive for use in organic electronics, electrochromic devices, and energy storage systems [35–40].

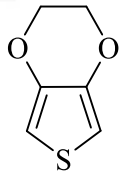

3,4-Ethylenedioxythiophene

Figure 1.5 : Chemical structure of 3,4-ethylenedioxythiophene

1.6 Triphenylamines

Triphenylamine (TPA) is a prototypical and basic example of the triarylamine (TAA) family. Its central nitrogen atom is linked to three carbon atoms through sp^2 hybridization, and its C-N bond has a length of 1,42 Å and C-N-C bond angle of 120°. The three phenyl units, which form a propeller-like structure when bonded to a nitrogen atom, have a torsional angle of 41.7° with respect to the plane defined by the three C-N bonds. TPA is a strong electron-donating unit because its ionization potential, 6.80 eV, is lower than that of many other inorganic and organic compounds. Its nonplanar structure is useful for limiting intermolecular aggregation and organizing

amorphous structures, which are highly desirable for optical applications since such compounds may produce dependable and practical thin films with uniform morphology and homogeneous properties. It is efficient to increase the material properties by changing the TPA unit with different substituents. Particularly, alkoxy-derived TPAs are extensively employed in the design of various materials because they increase the ability to donate electrons, which affects the HOMO and LUMO energy levels and lowers band gaps [41–44].

Ullmann coupling, one of the most common methods used for the synthesis of substituted or unsubstituted TPA, occurs by the reaction of iodobenzene and aniline derivatives in the presence of copper iodide, phenanthroline and potassium hydroxide (Figure 1.6). Iodobenzene and aniline can be produced from the ortho, meta, or para locations of the TPA ring, depending on its functional group. In general, the photophysical characteristics of TPA structures with functional groups are superior, since the addition of electron donor substituents to the para locations of TPA rings increases the ring's capacity to transfer electrons [45, 46].

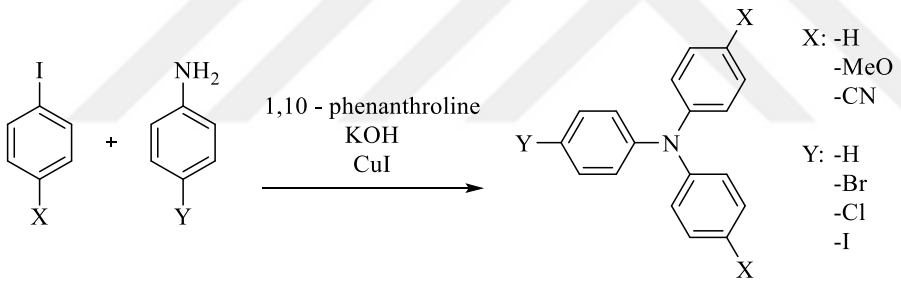

Figure 1.6 : TPA and its derivatives' synthesis.

1.7 Applications of Organic Electronics in Material Chemistry

Among the materials researches in the last few years, the most frequently discussed topic is material chemistry. Material chemistry is the use of chemistry to design and synthesize compounds that can be used due to their magnetic, optical, structural and catalytic properties. Organic electronic materials used in this field have been an increasing focus of attention, especially in the fields of chemistry and physics. In addition, π-conjugated materials with thiophene are particularly interesting due to their flexibility, low cost, excellent charge carrier mobility, and environmental durability. Thienothiophenes have started to be used in modern technology by examining their optical and electrical properties with the developing technology. Conjugated cyclic systems containing sulfur are generally charge transfer complexes. Due to these

properties, it is used in the construction of organic conductive, magnetic and photosensitivity receptors and in optoelectronic devices. Thienothiophenes are molecules with symmetrical structures and are favorite compounds in the construction of organic semiconductors. In material chemistry, conductive thienothiophenes with stable conjugated heterocyclic structure are used in the development of various devices in the field of energy. Some of these are OPVs, OLEDs, OFETs, Porous Polymers, and Capacitors.

1.7.1 Organic photovoltaics

In its simplest definition, a photovoltaic cell or organic solar cell is a system that converts sunlight into electrical energy. Polymeric solar cells are becoming a promising alternative to renewable and clean energy as they can be applied to large areas at low cost on inexpensive and lightweight substrates. Poor charge carrier generation and unbalanced charge transfer cause OPVs with a single-component active layer to have very low power conversion efficiency (PCE). Photovoltaic devices containing molecular and polymeric active layers had PCE of only 10-5% in the early 1970s and only 0.5% in the early 1990s. This number rises to over 20% today [47–50].

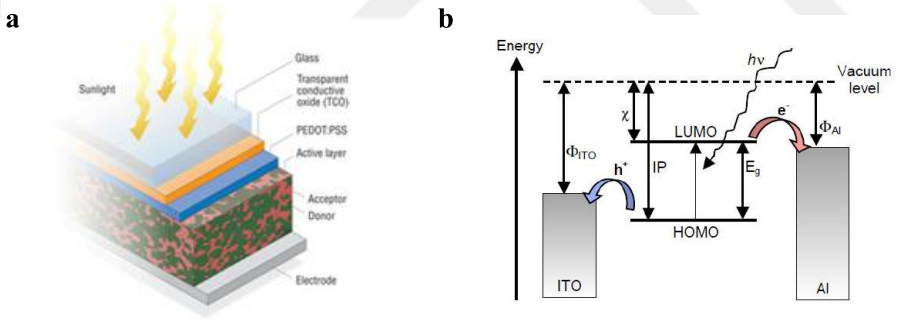

Figure 1.7 : Device structure (a) and simplified energy diagram of working principle of solar cells (b).

The working principle of the solar cell begins with the transfer of electrons. With this transfer, exciton (electron-hole pair) dissociation takes place, and this event occurs between the contact and the semiconductor or between molecules with different acceptor/donor properties. In organic solar cells, electron and electron holes are generally transported in different regions from each other (Figure 1.7). For a high efficiency of charge collection, there should be no energy barrier between the organic

semiconductor material and the metal electrode. Sometimes the efficiency can be increased by using an additional material to remove this barrier [51].

1.7.2 Organic light-emitting dioedes

OLEDs were first reported as efficient, low-voltage devices having p-n heterostructures used in organic thin films by Kodak employees Tang and Van Slyke in 1987. The technological advancements of OLEDs increased with the discovery of electroluminescent polymers by Cambridge University in 1990 [52].

A device known as an OLED emits light when an external voltage is applied. OLED devices can be divided into two primary categories: those designed with small organic molecules and those designed with organic polymers. OLEDs are an excellent modern light source due to their unique aspects of being flexible, transparent, lightweight, and color-tunable. OLEDs are solid-state semiconductor devices with thicknesses ranging from 100 to 500 nanometers. They consist of an emissive and conducting layer sandwiched between two electrodes and built on a substrate. In the device structure (Figure 1.8), anode used is indium tin oxide (ITO) and the cathode is made of a low-functioning metal. OLEDs start to emit light when a power source applies voltage to devices. Consequently, the organic layers allow electrons to move from the cathode to the anode. The cathode donates electrons to the light-emitting organic layer. The anode attracts electrons from the conduction layer. The circuit is complete when the gaps between the emissive and conductive layers are filled by electrons. Light is produced when an electron fills the hole and releases energy (photon). The form of organic molecule in the emissive layer determines the color of the light that is emitted [53].

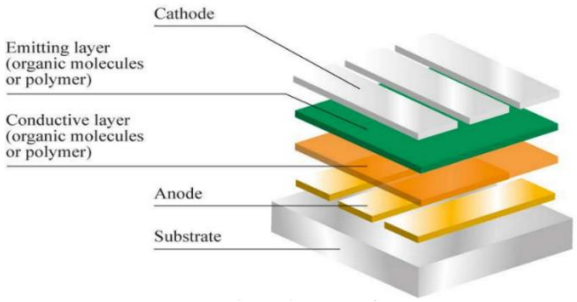

Figure 1.8 : Device structure of OLED.

1.7.3 Organic field effect transistors

A field effect transistor functions similar to a capacitor, with the source and drain electrodes operating as ohmic contacts on one side of the conducting channel.The

voltage applied to the gate electrode, which acts as the second plate of the capacitor, influences the concentration of charge carriers within the channel [54]. An OFET is a three-terminal device with the third terminal controlling the current flow between the other two. The source and drain electrodes are the two specific terminals that control current, while the gate electrode, which regulates current flow between the source and drain, is the third terminal [55]. Depending on how the layers have been stacked, these layers are usually configured in one of four device structures (Figure 1.9): bottom gate (BG) with bottom contacts (BC) (a), bottom gate (BG) with top contacts (TC) (b), top gate (TG) with bottom contacts (BC) (c), and top gate (TG) with top contacts (TC) (d). Each of these four configurations has its own set of benefits and drawbacks, and the selection of a structure is closely tied to the intended objectives [56].

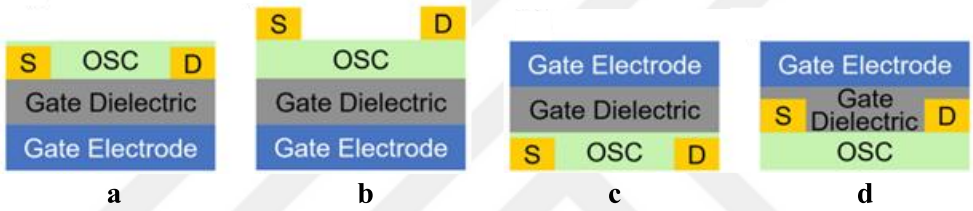

Figure 1.9 : OFET device structures: (a) BG, BC; (b) BG, TC; (c) TG, BC; and (d) TG, TC [56].

1.7.4 Porous organic polymers

Porous structures have long existed in nature, as seen in materials like charcoal, biological tissues, and rocks. The term "porous" describes materials that contain interconnected, permanent voids, which allow for the transport of gases or liquids. According to IUPAC classification, porous materials are divided by pore size into microporous (smaller than 2 nm), mesoporous (between 2 and 50 nm), and macroporous (higher than 50 nm) categories. Over the past two decades, advanced porous materials have received increasing attention due to their potential in a wide range of scientific and technological applications [57, 58]. Among these, porous organic polymers (POPs) have emerged as a particularly promising class owing to their light-weight nature, superior porosity, high surface areas, low densities, excellent thermal and chemical stability, and environmentally benign composition based on light elements such as carbon, nitrogen, and oxygen [59–61]. POPs can be broadly divided into two categories: crystalline structures, such as covalent organic frameworks (COFs), and amorphous structures, such as conjugated microporous polymers (CMPs),

polymers of intrinsic microporosity (PIMs), conjugated microporous polymers (HCPs), and porous aromatic frameworks (PAFs) (Figure 1.10). The π-conjugated backbones of many POPs and their compatibility to post-synthetic functionalization allow for precise control over pore size, surface chemistry, and electronic properties [59, 62]. Because of these characteristics, POPs are excellent choices for a variety of uses, including as energy storage and conversion, gas storage and separation, heterogeneous catalysis, photoelectric conversion, and chemical and biosensing [63].

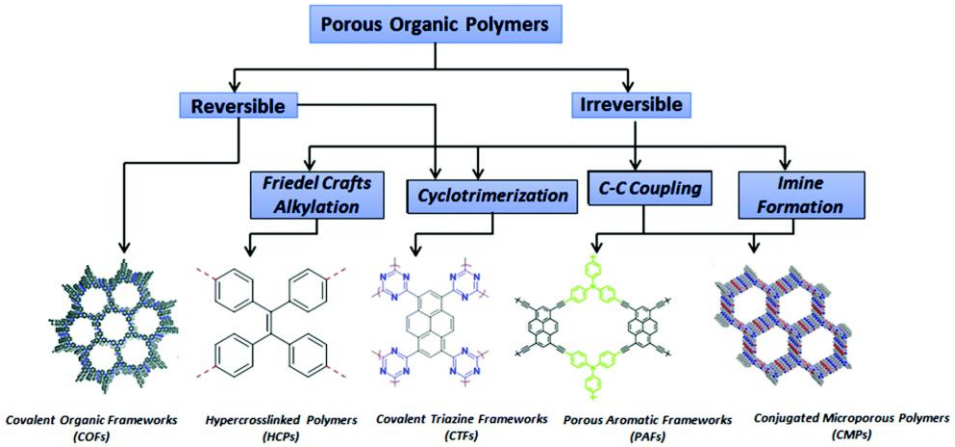

Figure 1.10 : Types of porous organic polymer frameworks and their coupling formation chemistries.

1.7.5 Capacitors

A capacitor is a passive device that stores energy electrostatically instead of chemically. It includes two parallel electrodes (plates) separated by a dielectric. A potential difference (voltage) between the electrodes charges the capacitor by forcing positive and negative charges to flow toward the surface of electrodes with opposing polarities. When charged, a capacitor connected into a circuit will function shortly as a voltage source [64]. Capacitors can vary in shape and size. However, the basic structure is fixed and consists of two conductors carrying equal amounts of opposite charges. Among the various applications of capacitors, there are applications such as storing electrical potential energy, delaying voltage changes that occur when combined with resistors, separating unwanted frequency signals [65].

1.7.5.1 Supercapacitors

The ability to store a remarkably high specific capacitance, long life cycle, high power density, low maintenance, no memory effect, and safety make electrochemical supercapacitors—also referred to as supercapacitors, ultracapacitors, or

electrochemical double-layer capacitors—particularly notable. [66–68]. In a typical supercapacitor setup, there are usually three key components; electrodes, electrolytes, separators and current collectors. The textural and morphological characteristics at the interface between the electrolyte and the material greatly impede capacitance when the material's bulk has restricted access to the electrolyte. Consequently, it is vital to explore a new category of electrode materials to achieve superior performance in supercapacitors [69, 70].

Numerous nanomaterials, including carbon nanostructures, have been investigated as potential electrodes for supercapacitors due to their large surface area, high electrical conductivity and stability in electrochemical environments [71, 72]. Carbon nanomaterials, such as carbon nanotubes, graphene, activated carbon and carbon nanocages, are the most commonly researched and applied materials for supercapacitor electrodes [73]. Carbon nanotubes (CNTs) are one-dimensional nanostructures that are extensively used and among the most promising candidates for energy storage applications. CNTs have a high surface area, a large surface-to-weight ratio and offer excellent storage capacity. Thanks to sp^2 hybridization in carbon-carbon (C-C) bonds, CNTs exhibit extraordinary electrical, thermal and mechanical properties [74, 75]. Carbon nanotubes (CNTs) are categorized into two structural types; (i) multi-walled carbon nanotubes (MWCNTs), consisting of multiple concentric graphene cylinders with an interlayer spacing around 0.34 nm, and (ii) single-walled carbon nanotubes (SWCNTs), formed by rolling a single graphene sheet into a seamless cylindrical tube (Figure 1.11) [76].

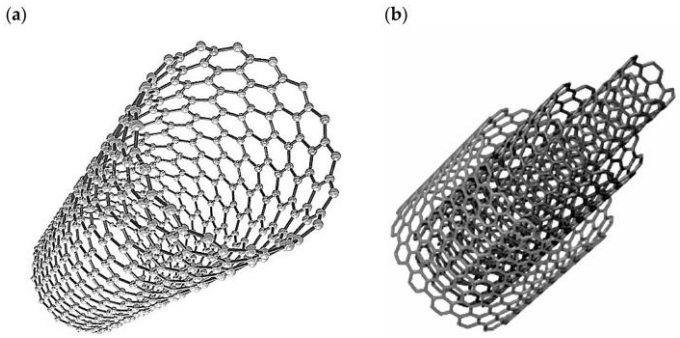

Figure 1.11 : Schematic of carbon nanotube's structure: (a) single-walled nanotube; (b) multi-walled nanotube [77].

The capacitance characteristics of CNT systems are influenced by various factors, including the number of graphene layers, type of electrode material, composition of the electrolyte solution and arrangement of the CNT layer. Pristine CNTs have a

relatively low specific capacitance, typically ranging from 2 to 45 Fg^{-1} for SWCNTs and from 3 to 74 Fg^{-1} for MWCNTs [78, 79]. Although both SWCNTs and MWCNTs exhibit excellent conductivity, SWCNTs offer greater advantages for supercapacitor applications. This is primarily due to their superior surface area, higher conductivity and better interconnectivity compared to MWCNTs [80]. To enhance the properties of SWCNTs, there has been an increasing attention on developing cost-effective and industrially viable modification techniques. These methods are broadly categorized into two types; (i) covalent (chemical) functionalization and (ii) non-covalent (physical) functionalization of SWCNT sidewalls [76, 81]. Non-covalent functionalization is particularly advantageous over covalent methods as it preserves the sp^2-to-sp^3 hybridization, the intrinsic conjugation and homogeneity of the SWCNT surface, which can otherwise be disrupted by covalent modifications such as halogenation and acylation reactions. The features of these hybrids can be customized by a variety of non-covalent modification techniques, such as hydrogen bonding, π-electrons or heteroatom-rich bonding agents, polymer wrapping, π-π interactions, electron pull-push complexes, and van der Waals forces [82, 83]. By leveraging these non-covalent modification techniques, the properties of SWCNT-conjugated semiconductor hybrids are improved for specific applications in multiple fields, such as electronics, energy storage, sensors and optoelectronics [84, 85].

1.8 Cross-Coupling Reactions

Palladium (Pd)-catalyzed cross-coupling reactions such as Suzuki, Stille, Heck, Negishi, and Sonogashira have become vital for the formation of carbon–carbon and carbon–heteroatom bonds in modern organic synthesis [86]. The mechanism and reaction conditions of cross-coupling reactions might differ based on the type of organometallic reagent used (Figure 1.12) [87]. Suzuki-Miyaura cross-coupling reactions, which involve organoboron reagents, require the use of an additional base. Organoboron reagents are one of the most important C-C bond formation processes due to their many advantages, such as low toxicity, inertness to water and other solvents, tolerance to various functional groups, and thermal stability. Contrariwise, organostannane reagent reactions are known as Stille cross-coupling reactions and do not require additional base. Organostannane reagents are widely used due to their

availability and air-moisture stability. However, the toxicity of organostannane reagents is a significant drawback. [88].

The general catalytic cycle for cross-coupling reactions includes i) oxidative addition, ii) transmetalation, and iii) reductive elimination. Catalytic performance depends on the properties of the metal reactant and the transition metal (Figure 1.13) [89].

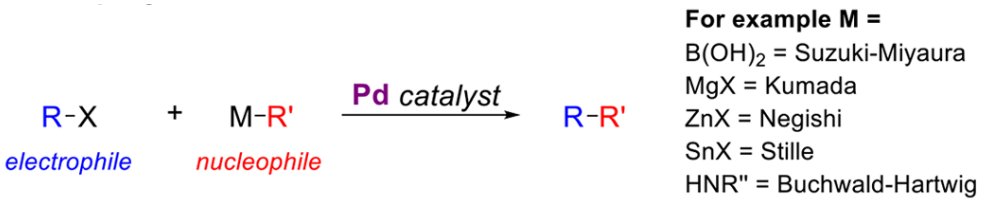

Figure 1.12 : Overview of cross-coupling reactions in general.

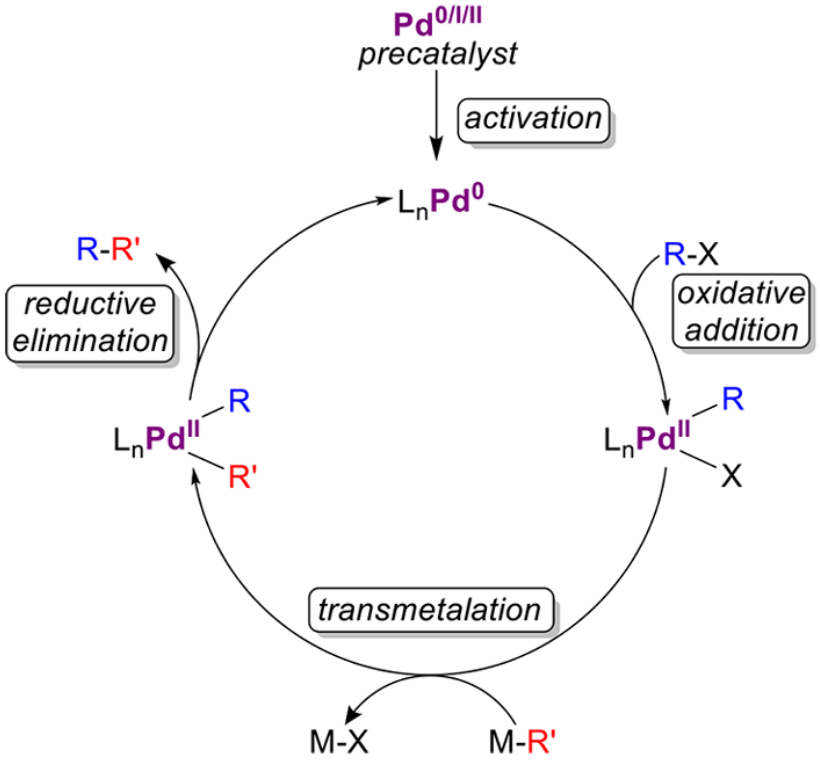

Figure 1.13 : Catalytic cycle for cross-coupling reactions in general.

2. EXPERIMENTAL

2.1 Materials

3-Bromothiophene (97%, Across), 2-Bromothiophene (98% Alfa-Aesar), *n*-Butyllithium (2.5 M in hexane, Across), tributyltin chloride (96%, Sigma-Aldrich), tetrakis(triphenylphosphine)palladium(0) ($Pd(PPh_4)_3$) (99%, Sigma-Aldrich), tris-(dibenzylideneacetone)dipalladium(0)($Pd_2(dba)_3$) (97%, Across), tri(o-tolyl)phosphine ($P(o\text{-}tol)_3$, 97%, TCI) polyphosphoric acid (PPA, 115% H_3PO_4 basis, Sigma-Aldrich), LDA (1M in THF/hexane,Sigma-Aldrich), and NBS (99%, Sigma-Aldrich) were obtained from commercial sources and used without further purification unless otherwise mentioned. Dry THF and toluene were obtained *via* distillation over sodium/benzophenone. Dichloromethane (Aldrich) was used as received. Sodium bicarbonate ($NaHCO_3$), sodium sulfate (Na_2SO_4), sulfur (S_8) and tetrabutylammonium hexafluorophosphate ($TBAPF_6$) were purchased from Merck.

2.2 Equipments

^1H NMR spectra was recorded on a Varian model NMR spectrometer (500 MHz), chemical shifts of which were reported in ppm downfield from tetramethyl silane (TMS). UV-Vis absorption spectra were obtained using a HITACHI U-0080D spectrophotometer. Fluorescence spectra were recorded on a HITACHI F4500 fluorescence spectrophotometer. Electropolymerizaiton and cyclic voltammetry (CV) measurements of polymers were performed using a VersaStat 3, Autolab PGSTAT204, Autolab VIONIC (INTELLO), Gamry 600 potentiostats. Platinum (Pt) wire electrode was used as counter, glassy carbon electrode (GCE) was used as working and a silver (Ag) electrode was used as a reference electrode. All electrochemical experiments of the hybrid materials were performed using a PARSTAT MC1000 potentiostat galvanostat from Amatek, USA, with a two-electrode split cell setup. Electrodes, each 10 mm in diameter, were cut with a punch and weighed. The split cell was then assembled, using cellulose acetate as a separator and H_3PO_4 solution (85%) as an electrolyte. The working electrode was first placed into

the cell, followed by the electrolyte-soaked separator on top of it. The counter electrode, identical to the working electrode, was then added, and the cell was sealed. Testing began after the cell's open circuit potential stabilized at a constant value. The employed test methods included cyclic voltammetry (CV), galvanostatic charge-discharge (GCD) and electrochemical impedance spectroscopy (EIS).

2.3 Synthesis of Monomers

2.3.1 General synthetic outline

3-Bromothiophene **1** was lithiated with *n*-butyllithium at −78 °C, which was followed by addition of elemental sulfur and then the α-bromoketone **2** to yield the corresponding monoketone **3**, ring closure reaction of which in the presence of PPA in refluxing chlorobenzene gave 3-(thiophen-2-yl)thieno[3,2-*b*]thiophene **4**. The three brominated 2,5-dibromo-3-(5-bromothiophen-2-yl)thieno[3,2-*b*]thiophene **5** was obtained through selective three bromination of **4** using NBS at -10 °C in DMF. The boronated triphenylamine **7** was constructed in a one-pot two-step reaction by lithiation of 4,4'-dimethoxytriphenylamine (**6**) with *n*-butyllithium at -78 °C and then addition of 2-isopropoxy-4,4,5,5-tetramethyl-1,3,2-dioxaborolane. Its Suzuki coupling reaction with 2-bromothiophene (**8**) produced the thiophene extended TPA, **9**. Its boronated derivative **10** was constructed treating **9** with *n*-butyllithium and then addition of 2-isopropoxy-4,4,5,5-tetramethyl-1,3,2-dioxaborolane. The EDOT based compounds were obtained using similar procedures. EDOT (**11**) was boronated by lithiation with *n*-butyllithium and addition of 2-isopropoxy-4,4,5,5-tetramethyl-1,3,2-dioxaborolane to gave the compound **12**, and its Suzuki coupling reaction with compound **6** produced the EDOT extended TPA (**13**). Its stannylated derivaitve **14** was constracted treating **13** with *n*-butyllithium and then addition of tributyltin chloride. Distannylated EDOT **15** was constructed treating **11** with TMEDA and *n*-buthyllithium and then addition of tributhyltinchloride (Figure 2.1 and Figure 2.2).

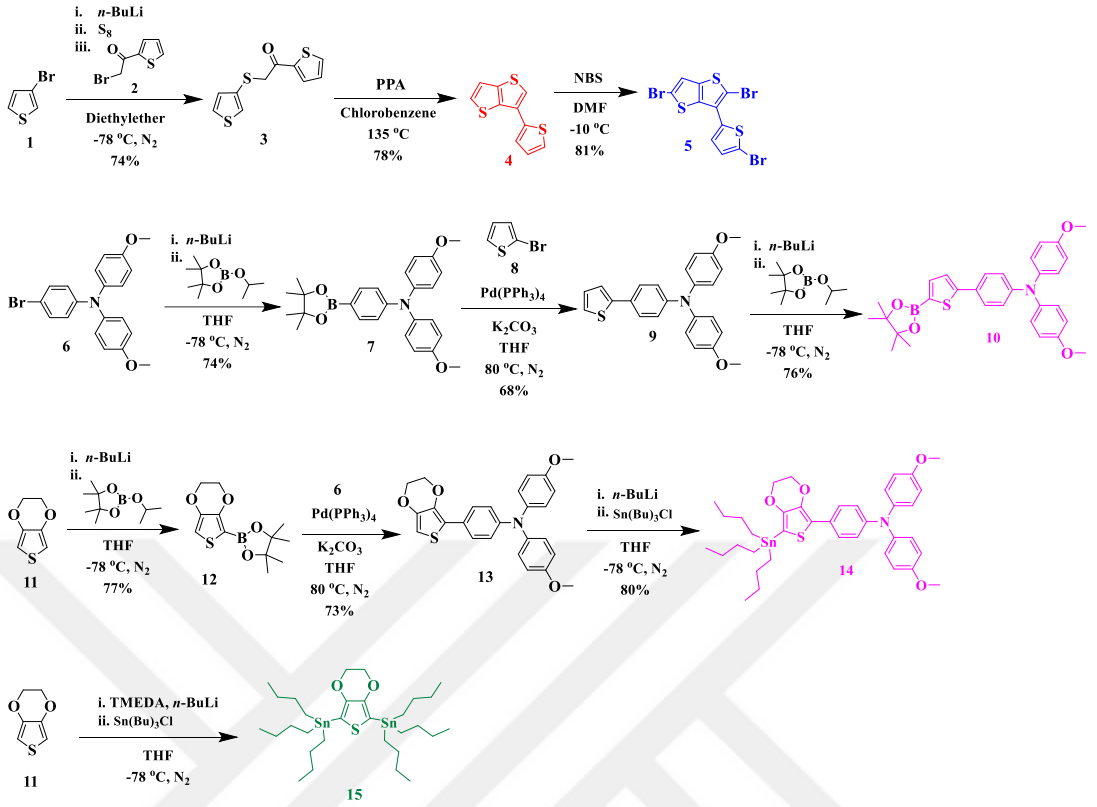

Figure 2.1 : Synthetic pathway of monomers.

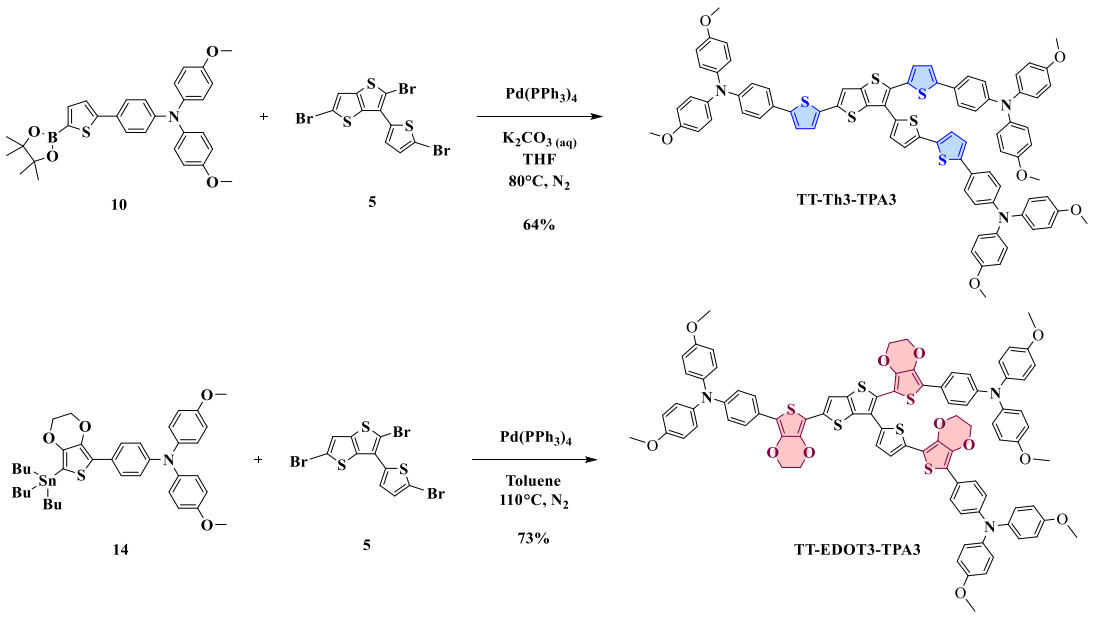

Figure 2.2 : Synthetic pathway of **TT-Th3-TPA3** and **TT-EDOT3-TPA3**.

2.3.2 Synthesis of 1-(thiophen-2-yl)-2-(thiophen-3-ylthio)ethan-1-one (3)

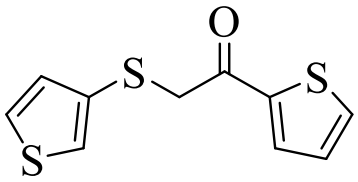

Figure 2.3 : Molecular structure of 1-(thiophen-2-yl)-2-(thiophen-3-ylthio)ethan-1-one.

To a solution of 3-bromothiophene **1** (1.0 g, 6.134 mmol) in dry diethyl ether (50 mL) was added *n*-butyllithium (2.9 mL, 7.36 mmol) dropwise at -78 °C, under nitrogen atmosphere. After the reaction was stirred for 45 min, elemental sulfur (S_8) (0.21 g, 6.44 mmol) was added, and the mixture was further stirred for 45 min. Then, 2-bromo-1-(thiophen-2-yl)ethan-1-one 2 (1.32 g, 6.44 mmol) was introduced portion wise into the mixture. After adding α-haloketone, the temperature was brought to room temperature. Stirring was continued overnight and the reaction was quenched with water. The solution was extracted with dichloromethane and the organic layer was washed with $NaHCO_3$ (10%) and water. The organic layer was dried over Na_2SO_4, filtered and the solvent was evaporated under reduced pressure. The crude product was purified by flash column chromatography eluting with a mixture of *n*-hexane:CH_2Cl_2 (3:1) to give the title compound **3** (Figure 2.3) (1.13 g, 74%). ^{1}H NMR (500 MHz, $CDCl_3$) δ 7.65 (d, *J* = 4.4 Hz, 2H), 7.30-7.28 (m, 2H), 7.10 (t, *J* = 4.4 Hz, 1H), 7.06 (dd, *J* = 4.1, 2.2 Hz, 1H), 4.05 (s, 2H).

2.3.3 Synthesis of 3-(thiophen-2-yl)thieno[3,2-*b*])thiophene (4)

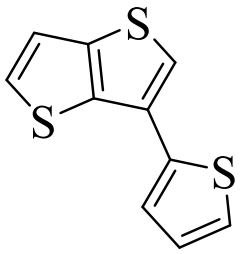

Figure 2.4 : Molecular structure of 3-(thiophen-2-yl)thieno[3,2-*b*])thiophene.

To a solution of polyphosphoric acid (PPA) (4.0 g, 41.61 mmol) in chlorobenzene (7 mL) at 135 °C was added 3 (1.0 g, 4.16 mmol), dissolved in chlorobenzene (6 mL) dropwise. The reaction was heated at this temperature for 7 h, after which the mixture was extracted with CH_2Cl_2, sodium bicarbonate solution and water. The organic layer was dried over Na_2SO_4, filtered and the solvent was evaporated under reduced

pressure. The residue was purified by column chromatography eluting with n-hexane to obtain the title compound **4** (Figure 2.4) (0.72 g, 78%). ^{1}H NMR (500 MHz, $CDCl_3$) δ 7.53 (d, *J*=1.6 Hz, 1H), 7.49-7.47 (m, 2H), 7.33 (dd, *J* = 5.2, 1.3 Hz, 2H), 7.18 (dd, *J* = 5.2, 3.5 Hz, 1H).

2.3.4 Synthesis of 2,5-dibromo-3-(5-bromothiophen-2-yl)thieno[3,2-*b*]thiophene (5)

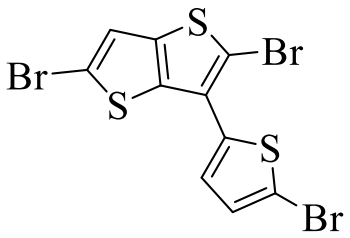

Figure 2.5 : Molecular structure of 2,5-dibromo-3-(5-bromothiophen-2-yl)thieno[3,2-*b*]thiophene.

To a solution of 4 (0.4 g, 1.799 mmol) dissolved in DMF (5 mL) was added NBS (1.06 g, 8.94 mmol) at -10 °C in dark. After the reaction was stirred for 12 h at the same temperature, the mixture was poured into water (50 mL) and left in the cold for 20 minutes to settle. Then, extraction was performed with sodium bicarbonate solution, dried with sodium sulfate, filtered and the solvent was completely evaporated. The precipitate was filtrated and purified by column chromatography eluting with *n*-hexane to obtain 2,5-dibromo-3-(5-bromothiophen-2-yl)thieno[3,2-*b*]thiophene **5** (Figure 2.5) (0.67 g, 81%). ^{1}H NMR (500 MHz, $CDCl_3$) δ 7.29 (d, *J* = 4.0 Hz, 1H), 7.23 (s, 1H), 7.14 (d, *J* = 3.9 Hz, 1H).

2.3.5 Synthesis of 4-methoxy-N-(4-methoxyphenyl)-N-(4-(4,4,5,5-tetramethyl-1,3,2-dioxaborolan-2-yl)phenyl)aniline (7)

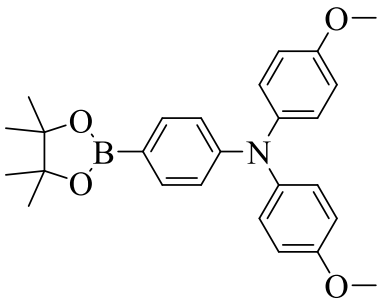

Figure 2.6 : Molecular structure of 4-methoxy-N-(4-methoxyphenyl)-N-(4-(4,4,5,5-tetramethyl-1,3,2-dioxaborolan-2-yl)phenyl)aniline.

To a solution of 6 (1.0 g, 2.6 mmol) in dry THF (50 mL) was added *n*-BuLi (2.1 mL, 2.5 M, 5.2 mmol) dropwise at -78 °C, under nitrogen atmosphere. After the reaction

was stirred for 45 min, 2-isopropoxy-4,4,5,5-tetramethyl-1,3,2-dioxaborolan (1.6 mL, 7.8 mmol) was introduced portion wise into the mixture. The reaction was stirred for 12 h at room temperature and, then, quenched with water. The mixture was extracted with CH_2Cl_2, sodium bicarbonate solution, brine and water. The organic layer was dried over Na_2SO_4, filtered and the solvent was evaporated under reduced pressure. The crude product was purified by flash column chromatography eluting with a mixture of *n*-hexane: CH_2Cl_2 (7:1) to obtain the title compound **7** (Figure 2.6) (0.83 g, 74%). ^{1}H NMR (500 MHz, $CDCl_3$) δ 7.61 (d, *J* = 8.3 Hz, 2H), 7.08 (d, *J* = 8.8 Hz, 4H), 6.88 (d, *J* = 8.4 Hz, 2H), 6.84 (d, *J* = 8.8 Hz, 4H), 3.81 (s, 6H), 1.33 (s, 12H).

2.3.6 Synthesis of 4-methoxy-N-(4-methoxyphenyl)-N-(4-(thiophen-2-yl)phenyl) aniline (9)

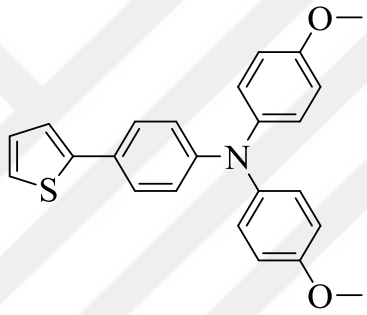

Figure 2.7 : Molecular structure of 4-methoxy-N-(4-methoxyphenyl)-N-(4-(thiophen-2-yl)phenyl)aniline.

To a mixture of **7** (0.78 g, 1.81 mmol) and **8** (0.27 g, 1.65 mmol), dissolved in THF (25 ml) and degassed for 45 min with N_2, was added K_2CO_3 (5 mL, 2M) and $Pd(PPh_3)_4$ (0.165 mmol). The mixture was then saturated with N_2, and the sealed reaction flask was stirred at 80 °C for 48 h, after which the crude product was filtered through celite, extracted with sodium carbonate and dichloromethane. The organic layer was dried over sodium sulfate, filtered, and the solvent was evaporated under reduced pressure. The crude product was purified by flash column chromatography eluting with a mixture of *n*-hexane:CH_2Cl_2 (8:1) to give the title compound **9** (Figure 2.7) (0.44 g, 68%) as a pale-yellow oil. ^{1}H NMR (500 MHz, $CDCl_3$) δ 7.42 (d, *J* = 8.7 Hz, 2H), 7.21–7.18 (m, 2H), 7.09 (d, *J* = 8.9 Hz, 4H), 7.05 (dd, *J* = 5.0, 3.7 Hz, 1H), 6.94 (d, *J* = 8.7 Hz, 2H), 6.85 (d, *J* = 9.0 Hz, 4H), 3.82 (s, 6H).

2.3.7 Synthesis of 4-methoxy-N-(4-methoxyphenyl)-N-(4-(5-(4,4,5,5-tetramethyl-1,3,2-dioxaborolan-2-yl)thiophen-2-yl)phenyl)aniline (10)

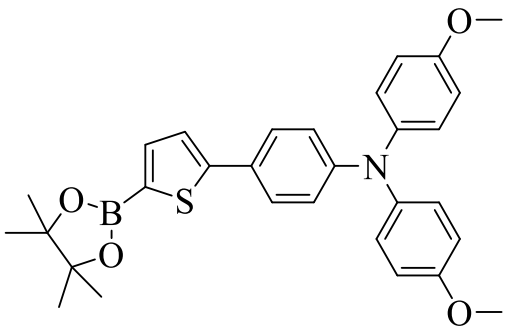

Figure 2.8 : Molecular structure of 4-methoxy-N-(4-methoxyphenyl)-N-(4-(5-(4,4,5,5-tetramethyl-1,3,2-dioxaborolan-2-yl)thiophen-2-yl)phenyl)aniline.

To a solution of **9** (0.4 g, 1.034 mmol) in dry THF (50 mL) was added 2.5 M *n*-BuLi (0.62 mL, 1,55 mmol) dropwise at -78 °C, under nitrogen atmosphere. After the reaction was stirred for 45 min, 2-isopropoxy-4,4,5,5-tetramethyl-1,3,2-dioxaborolan (1.6 mL, 3.09 mmol) was introduced portion wise into the mixture. The reaction was stirred for 12 h at room temperature, then, quenched with water. The mixture was extracted with CH_2Cl_2, sodium bicarbonate solution, brine and water. The organic layer was dried over Na_2SO_4, filtered and the solvent was evaporated under reduced pressure. The crude product was purified by flash column chromatography eluting with a mixture of *n*-hexane: CH_2Cl_2 (7:1) to obtain the title compound **10** (Figure 2.8) (0.40 gr, 76%). ^{1}H NMR (500 MHz, $CDCl_3$) δ 7.47 (d, *J* = 8.8 Hz, 2H), 7.10 (dd, *J* = 17.3, 8.7 Hz, 4H), 6.92–6.82 (m, 8H), 3.83 (s, 6H), 3.81 (s, 12H).

2.3.8 Synthesis of 2-(2,3-dihydrothieno[3,4-*b*][1,4]dioxin-5-yl)-4,4,5,5-tetramethyl-1,3,2-dioxaborolane (12)

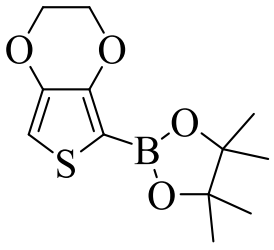

Figure 2.9 : Molecular structure of 2-(2,3-dihydrothieno[3,4-*b*][1,4]dioxin-5-yl)-4,4,5,5-tetramethyl-1,3,2-dioxaborolane.

A solution of 11 (1.0 g, 7 mmol) in dry THF (25 mL) at -78 °C under nitrogen atmosphere was treated with a solution of *n*-BuLi (3.1 mL, 2.5 M, 7.7 mmol). The

temperature of the mixture was maintained at 0 °C for 30 min and, then, cooled to -78 °C to introduce a solution of 2-isopropoxy-4,4,5,5-tetramethyl-1,3,2-dioxaborolane (2,9 mL, 14.2 mmol) in THF (5 mL). The reaction was stirred for 18 h at room temperature, then quenched with a solution of sodium chloride. The product was extracted with diethyl ether, washed with water and dried over sodium sulfate. The product **12** was obtained by precipitation in hexane as a white solid (Figure 2.9) (1.47 g, 77%). ^{1}H NMR (500 MHz, $CDCl_3$) δ 6.63 (s, 1H), 4.33-4.28 (m, 2H), 4.21-4.15 (m, 2H), 1.34 (s, 12H).

2.3.9 Synthesis of 4-(2,3-dihydrothieno[3,4-*b*][1,4]dioxin-5-yl)-N,N-bis(4-methoxy phenyl)aniline (13)

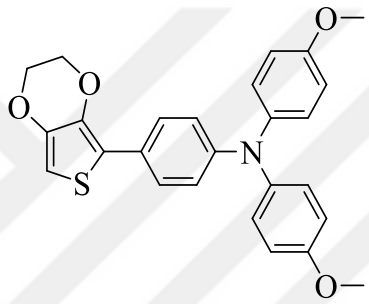

Figure 2.10 : Molecular structure of 4-(2,3-dihydrothieno[3,4-*b*][1,4]dioxin-5-yl)-N,N-bis(4-methoxy phenyl)aniline.

To a mixture of **6** (0.56 g, 0.15 mmol) and **12** (0.45 g, 0.17 mmol), dissolved in THF (25 ml) and degassed for 45 min with N_2, was added K_2CO_3 (5 mL, 2 M) and $Pd(PPh_3)_4$ (0.015 mmol). The mixture was then saturated with N_2, and the sealed reaction flask was stirred at 80 °C for 48 h, after which the crude product was filtered through celite, extracted with sodium carbonate and dichloromethane, dried over sodium sulfate, filtered, and the solvent was evaporated under reduced pressure. The crude product was purified by flash column chromatography eluting with a mixture of *n*-hexane:CH_2Cl_2 (4:1) and, then, recrystallized from methanol to give the titled compound **13** (Figure 2.10) (0.49 g, 73%) as a light brown powder. ^{1}H NMR (500 MHz, $CDCl_3$) δ 7.59 (d, *J* = 8.7 Hz, 2H), 7.25 (d, *J* = 7.5 Hz, 3H), 7.12 (d, *J* = 8.4 Hz, 4H), 7.06 (s, 2H), 7.02 (t, *J* = 7.3 Hz, 2H), 6.26 (s, 1H), 4.32-4.28 (m, 2H), 4.25-4.21 (m, 2H), 3.81 (s, 6H).

2.3.10 Synthesis of 4-methoxy-N-(4-methoxyphenyl)-N-(4-(7-(tributylstannyl)-2,3 dihydrothieno[3,4-*b*][1,4]dioxin-5-yl)phenyl)aniline (14)

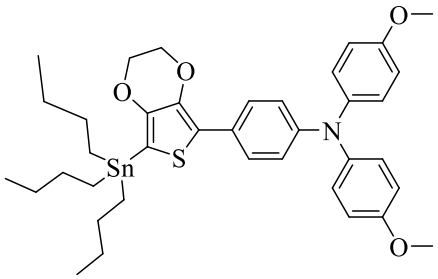

Figure 2.11 : Molecular structure of 4-methoxy-N-(4-methoxyphenyl)-N-(4-(7-(tributylstannyl)-2,3 dihydrothieno[3,4-*b*][1,4]dioxin-5-yl)phenyl)aniline.

To a solution of **13** (0.35 g, 0.79 mmol) in dry THF (30 mL) was added *n*-BuLi (0.7 mL, 1.74 mmol) dropwise at -78 °C, under nitrogen atmosphere. After the reaction was stirred for 1 h, tributyltin chloride (0.55 mL, 2.0 mmol) was introduced portion wise, after which the temperature was brought to room temperature and the stirring was continued overnight. The reaction was then quenched with water and the mixture was extracted with dichloromethane, washed with brine and water. The organic layer was dried over Na_2SO_4, filtered and the solvent was evaporated under reduced pressure. Compound **14** (Figure 2.11) was obtained as a brown liquid after removal of the solvent and used without further purification for the next step.

2.3.11 Synthesis of 5,7-bis(tributylstannyl)-2,3-dihydrothieno[3,4-*b*][1,4]dioxine (15)

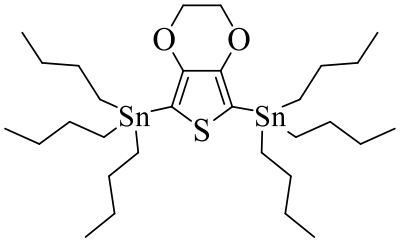

Figure 2.12 : Molecular structure of 5,7-bis(tributylstannyl)-2,3-dihydrothieno[3,4-*b*][1,4]dioxine.

A mixture of **11** (1.0 g, 7 mmol) and 1.05 mL N,N,N',N',-tetramethylethylenediamine (TMEDA) (7 mmol) in dry THF (25 mL) at -78 °C under nitrogen atmosphere was treated with a solution of *n*-BuLi (2.5 mL, 2.5 M, 19.6 mmol). The temperature of the mixture was maintained at 0 °C for 2 h and, then, cooled to -78 °C to introduce a solution of tributhyltin chloride (5.7 mL, 21 mmol). The reaction was stirred for 5 h at room temperature, then quenched with water. The product was extracted with CH_2Cl_2,

washed with water and dried over sodium sulfate, filtered and the solvent was evaporated under reduced pressure. Compound **15** (Figure 2.14)was obtained as a dark liquid after removal of the solvent and used without further purification for the next step.

2.3.12 Synthesis of TT-Th3-TPA3

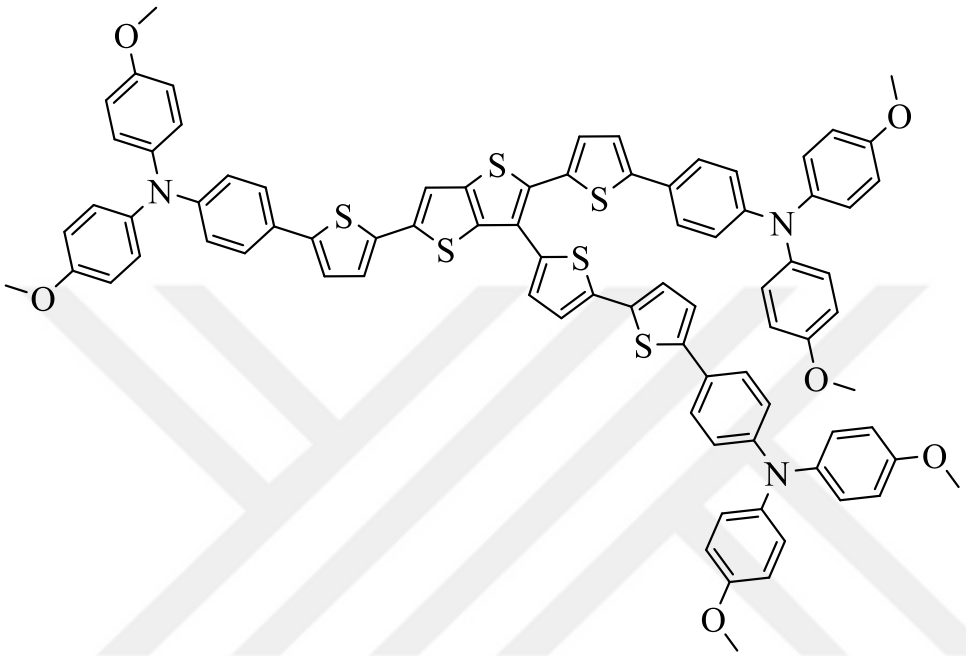

Figure 2.13 : Molecular structure of **TT-Th3-TPA3**.

To a mixture of **5** (0.055 g, 0.12 mmol) and **10** (0.2 g, 0.39 mmol), dissolved in THF (25 ml) degassed for 45 min with N_2, was added K_2CO_3 (5 mL, 2M) and $Pd(PPh_3)_4$ (0.012 mmol). The mixture was saturated with N_2, and the sealed reaction flask was stirred at 80 °C for 48 h, after which the crude product was filtered through celite, extracted with sodium carbonate and dichloromethane, dried over sodium sulfate, filtered and the solvent was evaporated under reduced pressure. The crude product was purified by flash column chromatography eluting with a mixture of *n*-hexane:CH_2Cl_2 (2:1) and recrystallization with *n*-hexane to give the title compound **TT-Th3-TPA3** (Figure 2.12) (0.106 g, 64%) as an orange solid. ^{1}H NMR (600 MHz, THF-d_8) δ 7.50 (s, 1H), 7.45-7.42 (m, 4H), 7.40 (d, *J* = 8.7 Hz, 2H), 7.25 (dd, *J* = 5.6, 3.8 Hz, 2H), 7.22 (d, *J* = 3.7 Hz, 1H), 7.18 (d, *J* = 2.6 Hz, 2H), 7.07-7.01 (m, 10H), 6.89-6.83 (m, 15H), 3.76 (s, 12H), 3.75 (s, 6H).

2.3.13 Synthesis of TT-EDOT3-TPA3

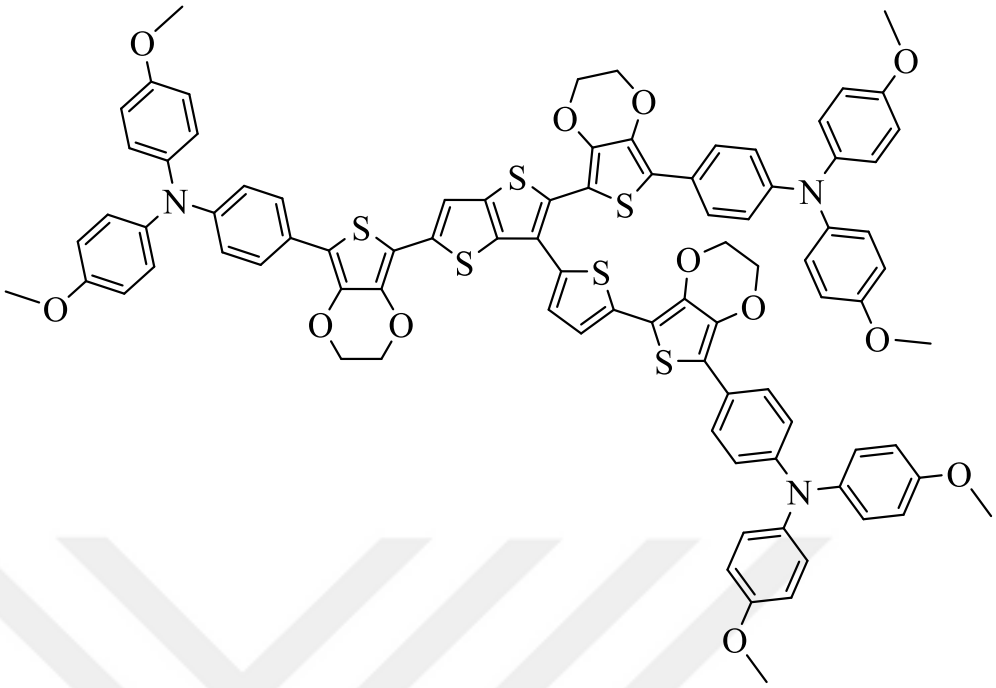

Figure 2.14 : Molecular structure of **TT-EDOT3-TPA3**.

To a mixture of **5** (0.055 g, 12 mmol) and **14** (0.35 g, 48 mmol), dissolved in toluene (30 ml) and degassed for 1 h with N_2, was added Pd $(PPh_3)_4$ (0.015 mmol). The mixture was saturated with N_2 and the sealed reaction flask was stirred at 80 °C for 48 h, after which the crude product was filtered through celite, extracted with sodium carbonate and dichloromethane, dried over sodium sulfate, filtered, and the solvent was evaporated under reduced pressure. The crude product was purified by flash column chromatography eluting with a mixture of *n*-hexane:CH_2Cl_2 (1:2) and recrystallization from hexane to give the titled compound **TT-EDOT3-TPA3** (Figure 2.13) (0.08 g, 73%) as a dark orange powder. ^{1}H NMR (500 MHz, $CDCl_3$) δ 7.60-7.51 (m, 7H), 7.10-7.05 (m, 13H), 6.92 (t, *J* = 7.9 Hz, 8H), 6.84 (d, *J* = 6.2 Hz, 11H), 4.42 (s, 2H), 4.33 (m, 8H), 4.24 (s, 2H), 3.81 (s, 18H).

2.4 Synthesis of Hybrid Films

The hybrids **TT-Th-TPA-SWCNT** and **TT-EDOT-TPA-SWCNT** were obtained as flexible, easily bendable and smooth black nanohybrid films (Figure 2.15) through

stirring of **TT-Th3-TPA3** and **TT-EDOT3-TPA3** with SWCNT, respectively, without using any binding agents in THF at room temperature for 7 days (Figure 2.16).

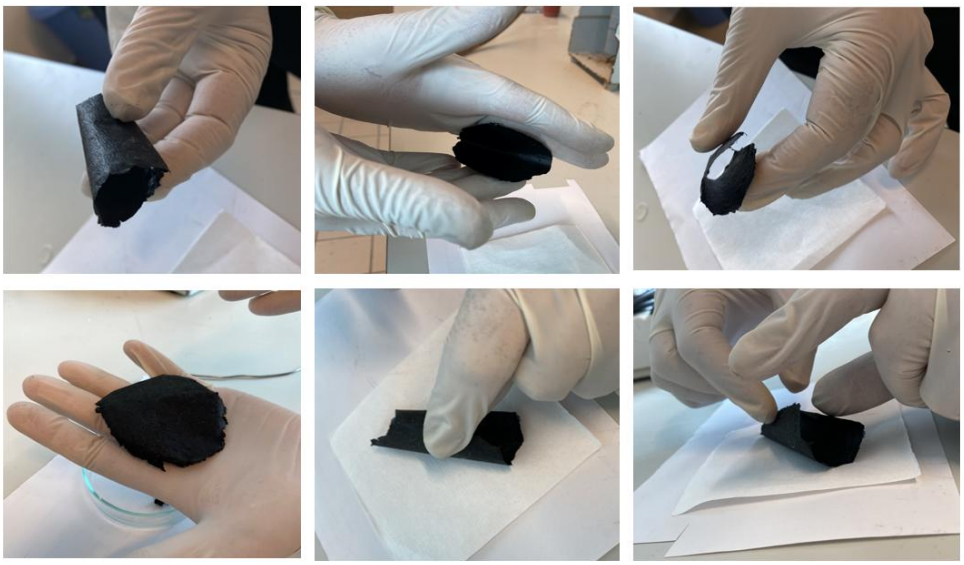

Figure 2.15 : Flexible and bendable images of the obtained hybrid films.**TT-EDOT-TPA-SWCNT** (above) and **TT-Th-TPA-SWCNT** (below).

2.4.1 Synthesis of hybrid TT-Th-TPA-SWCNT

To a round-bottom flask were added CoMoCat SWCNTs (Southwest NanoTechnologies, 10 mg), **TT-Th3-TPA3** (50 mg) (ratio of TT derivative to nanotube: 5, w/w) and dry THF (100 mL). The resulting mixture was sonicated for 30 min in a low-power sonic bath and, then, stirred vigorously for 7 days at room temperature. To remove unattached TT derivatives, the mixture was filtered through a 0.2-μm Teflon membrane and washed with excess THF (Sartorious, PTFE; pore size, 0.2 μm). The recovered black hybrid film was dried under vacuum for 24 h.

2.4.2 Synthesis of hybrid TT-EDOT-TPA-SWCNT

To a round-bottom flask were added CoMoCat SWCNTs (Southwest NanoTechnologies, 10 mg), **TT-EDOT3-TPA3** (50 mg) (ratio of TT derivative to nanotube: 5, w/w) and dry THF (100 mL). The resulting mixture was sonicated for 30 min in a low-power sonic bath and, then, stirred vigorously for 7 days at room temperature. To remove unattached TT derivatives, the mixture was filtered through a 0.2-μm Teflon membrane and washed with excess THF (Sartorious, PTFE; pore size, 0.2 μm). The recovered black hybrid film was dried under vacuum for 24 h.

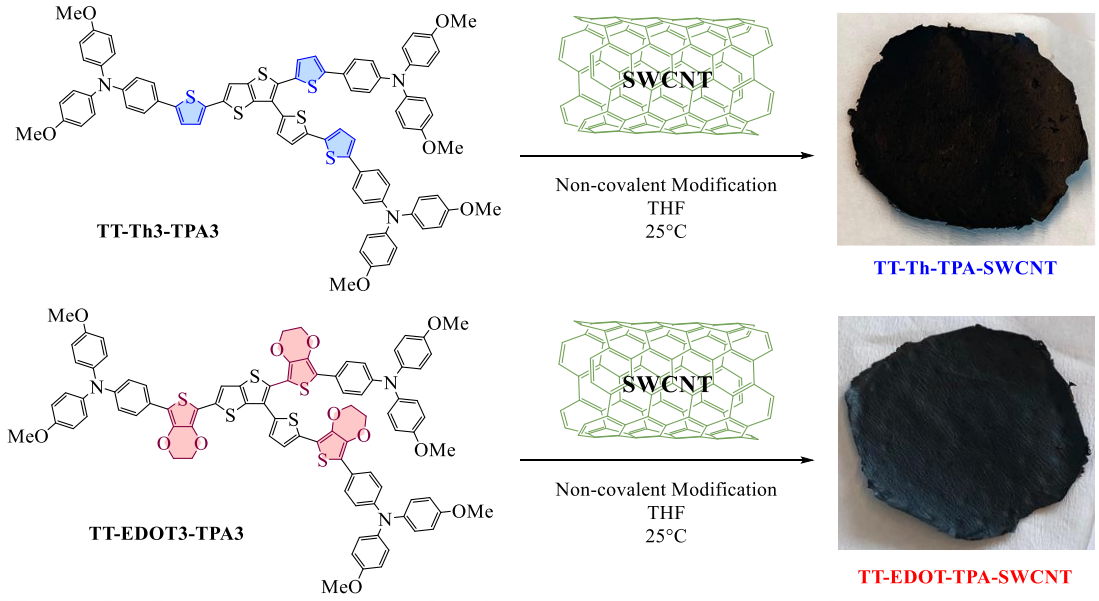

Figure 2.16 : Synthesis of the hybrids TT-Th-TPA-SWCNT and TT-EDOT-TPA-SWCNT.

2.5 Synthesis of Polymers

2.5.1 Polymerization of TT-Th-EDOT

The tribrominated TT-Th (**5**) (0.2 gr) was polymerized with distannylated EDOT (**15**) (0.22 gr) to applying Stille coupling reaction to obtain **P(TT-EDOT)** (Figure 2.17). The polymer precipitated in methanol. The precipitate was filtered and stirred with a solution of MeOH and HCl (1 N) for 1 h. After removal of the solvent, the residue was Soxhlet-extracted with MeOH (24 h), and THF (24 h) to remove oligomers and other small molecular parts. The remaining black solid was dried overnight under vacuum to yield the target compound **P(TT-EDOT)** (88 mg).

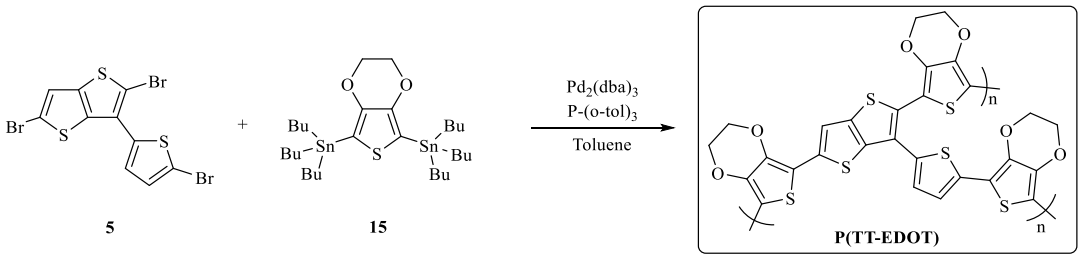

Figure 2.17 : Synthetic route of **P(TT-EDOT)**.

2.5.2 Electropolymerizaiton of TT-Th

Electropolymerization of TT-Th (**4**) was performed by the potentiodynamic method in DCM:ACN (1:1 v/v) mixture, containing 0.1 M $TBAPF_6$ supporting electrolyte. The monomer concentration was prepared as a 1×10^{-3} M mixture and a scan rate of 100

$mV \cdot s^{-1}$ was applied. Electrochemical polymerizations of the monomers were performed in a standard three electrodes system, using a spiral platinum wire as a counter electrode, a silver wire as a pseudo-reference electrode, and a glassy carbon bottom electrode (area = 0.022 cm^2) as a working electrode, to provide a better polymerization stability and deposition on the electrode surface.

The oxidation (E_{ox}) potentials of the monomer were located at 0.94 and 1.42 V, and onset (E_{onset}^{ox}) potentials of the monomer 0.86 and 1.32 V, respectively. Considering this result, electropolymerization was conducted in two different potential ranges, i.e. 0.0–1.1 and 0.0–1.6V (Figure 2.18).

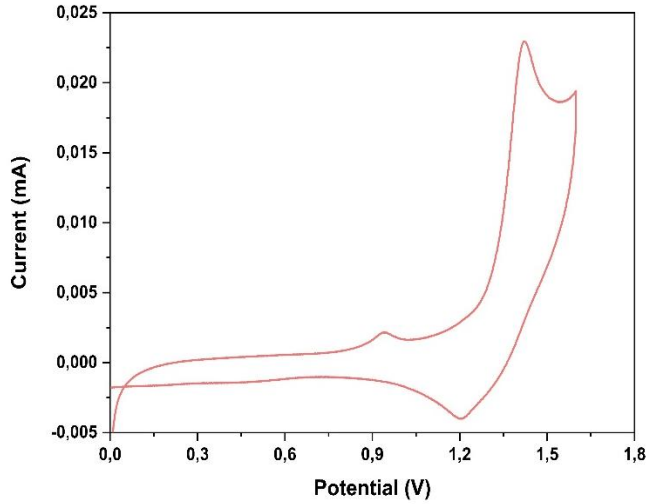

Figure 2.18 : CV of 1×10^{-3} M **TT-Th** in 0.1 M $TBAPF_6$ in DCM/ACN (1:1) and a scan rate of 100 $mV \cdot s^{-1}$ with potential range 0.0–1.6 V.

3. RESULTS AND DISCUSSION

3.1 Mechanism of Reactions

3.1.1 Mechanism of ketone formation

The *n*-BuLi attacks the bromine atom of the 3-bromothiophene, resulting in the formation of lithiated thiophene carbanion salt. With the addition of S_8, the carbanion attacks one S atom of S_8 and breaks the other S-S bond. The broken bond turns over S, resulting in the formation of the S anion. The S anion attacks the thiophene on the carbon adjacent to the attached sulfur, generating the S_7 ring, and the S anion on thiophene is formed with the Li counter atom. Finally, by adding α-bromo to the reaction mixture, the lithiated sulfur anion attacks the carbon of the ketone and bromine is left. As a result, the monoketone form is produced (Figure 3.1)

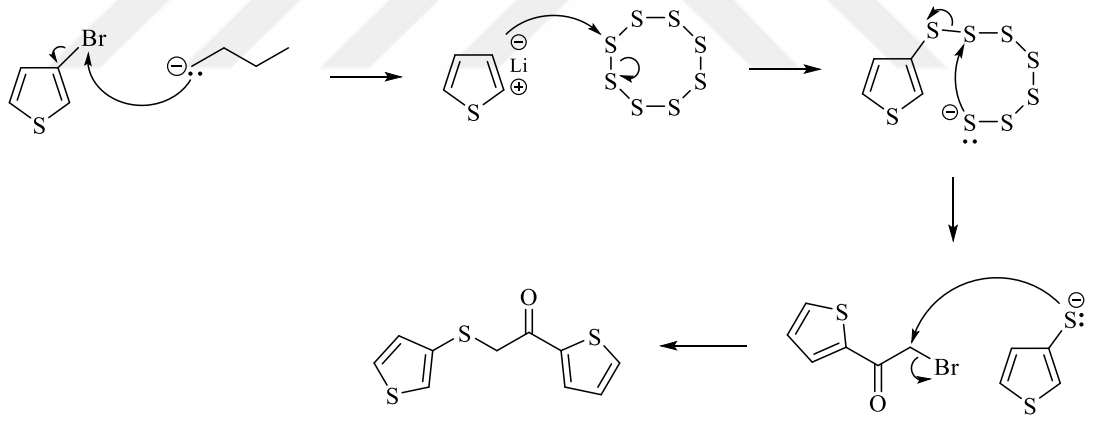

Figure 3.1 : Mechanism of ketone formation.

3.1.2 Ring closure mechanism

Polyphosphoric acid (PPA) promotes intramolecular cyclization at various temperatures and a proton donor for condensation reactions. When a monoketone is heated in the presence of PPA, the ketone attacks a proton from the PPA and TT is formed by intermolecular rearrangement (Figure 3.2).

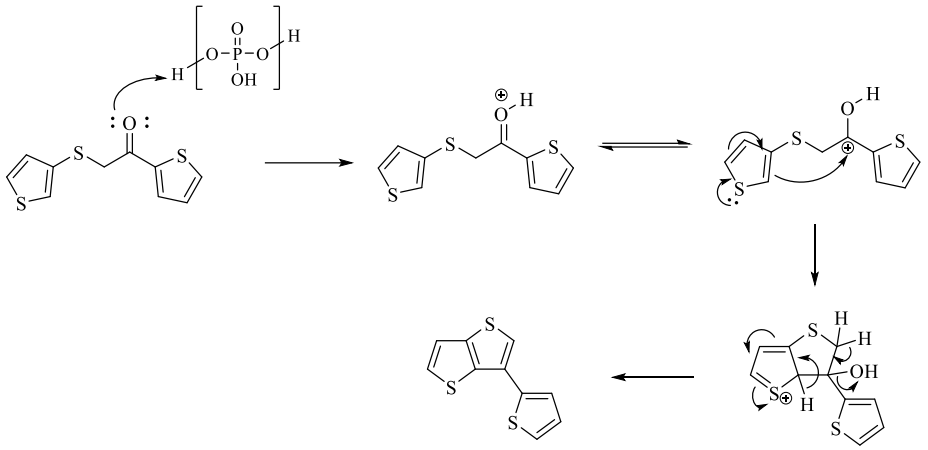

Figure 3.2 : Mechanism of ring closure reaction.

3.1.3 Tribromination mechanism

Nitrogen on NBS is partially negative, bromine is partially positive. For this reason, the N-Br bond is partially polar. Carbon at position 2 on TT is more active than other carbons. This activated carbon attacks the electrophilic bromine and the electrons are placed on the nitrogen. The negatively charged nitrogen attacks the hydrogen in the C-Br bond and the C-H bond is broken. Monobromination occurs with intramolecular rearrangement. In the reaction, mono, di or tribromination is done with the amount of NBS. 3.3 equivalents of NBS brominates the activated carbons on the TT, the carbon at the active position 2 of Th bonded to TT bromines and the tribrominated TT- Th is obtained (Figure 3.3).

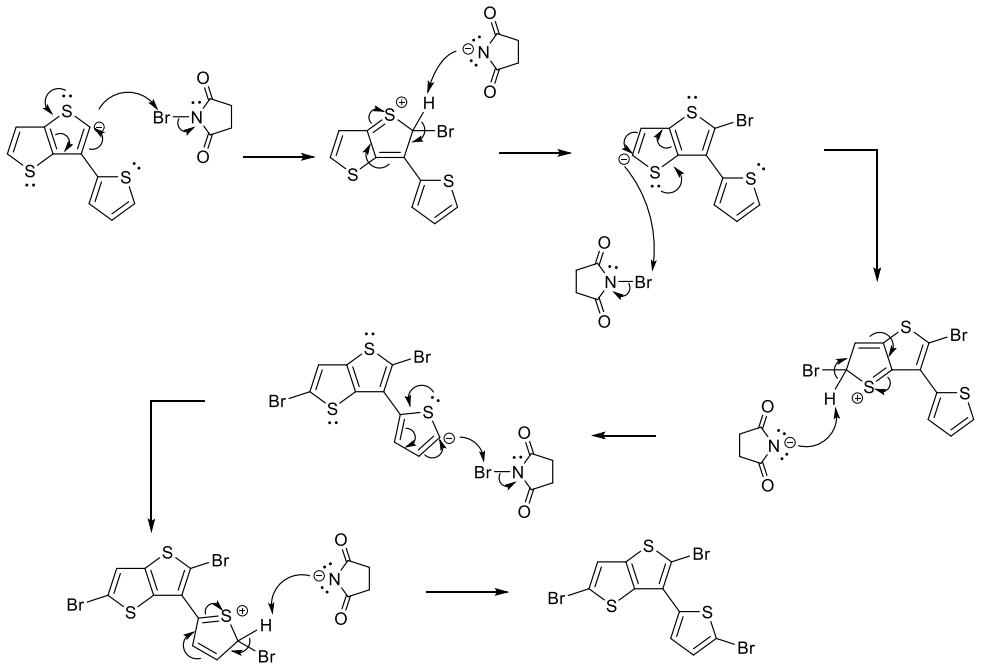

Figure 3.3 : Tribromination mechanism of TT.

3.1.4 Suzuki coupling mechansim

In Suzuki coupling reactions, Pd((PPh$_3$)$_4$) or Pd$_2$(dba)$_3$) are used as catalysts in basic media with K_2CO_3 content. There must be reactants containing brominated and boronated units. It proceeds through 3 main steps in this catalytic cycle: i) oxidative addition, ii) transmethylation and iii) reductive elimination. Reaction mechanism has shown on Figure 3.4**.**

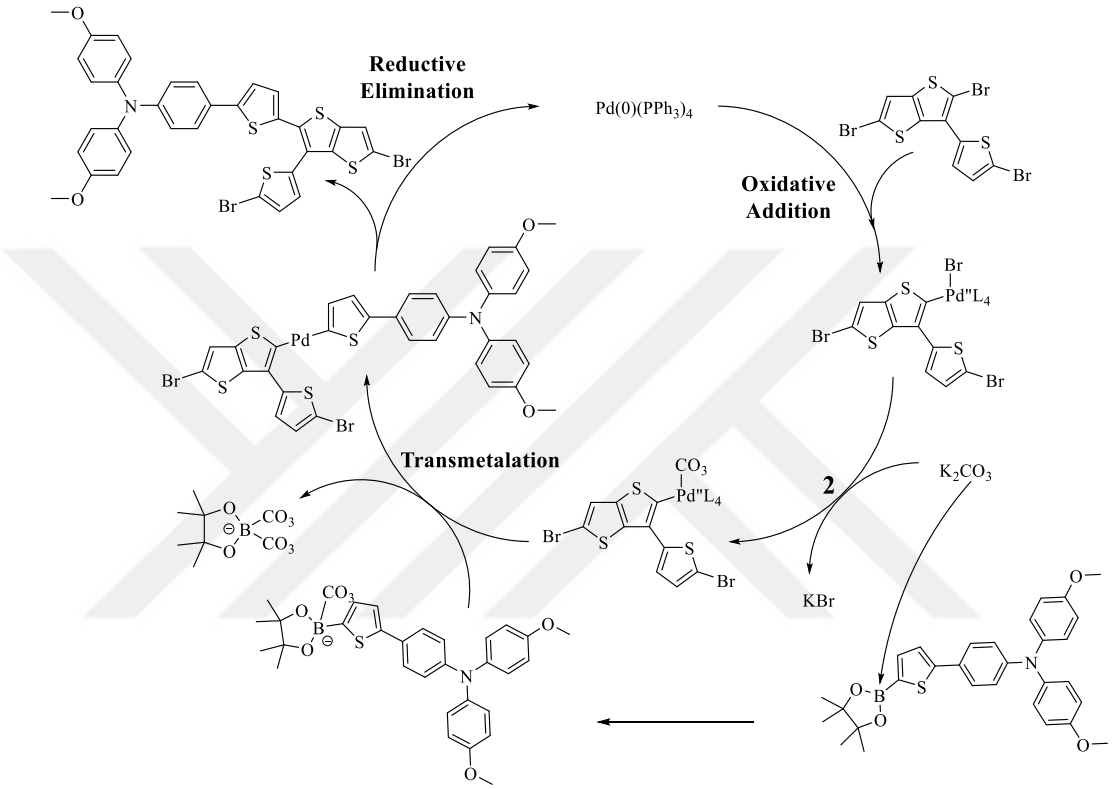

Figure 3.4 : Suzuki coupling reaction mechanism via **TT-Th3-TPA3**.

3.1.5 Stille coupling mechanism

In Stille coupling reactions, Pd$_2$(dba)$_3$ is used as catalysts and P(o-tol)$_3$ is used as ligand. Two organic groups are coupled in this reaction, with one of the groups being an organotin complex also called an organostannane. The other coupling partner comes from a wide range of organic electrophiles. These organostannanes are also resistant to oxygen and water. However, these tin reagents are typically extremely toxic. In most cases, X is a halide, such as Cl, Br, or I . This catalytic cycle consists of three primary steps: i) oxidative addition, ii) transmetalation, and iii) reductive elimination. A Pd(II) complex is formed when the organohalide is added to the Pd(0) oxidatively. Following transmetalation, the R group takes the place of the halide anion on the palladium

complex in the organostannane reagent. Reductive elimination then yields the final coupled product, allowing the catalytic cycle to continue and regenerating the palladium catalyst. Reaction mechanism has shown on Figure 3.5.

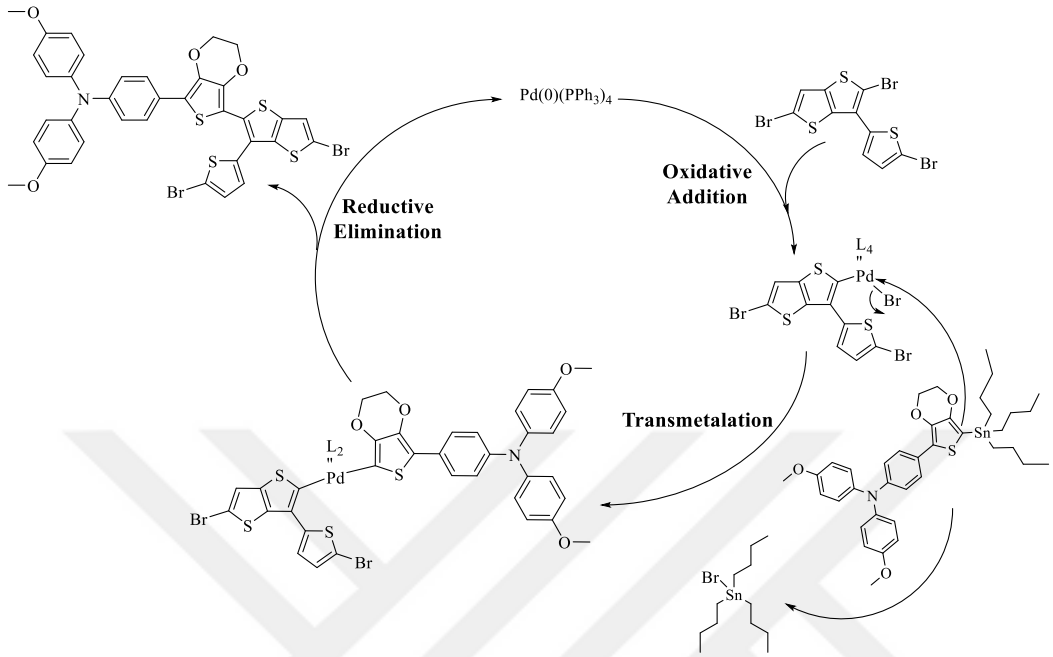

Figure 3.5 : Stille coupling reaction mechanism via **TT-EDOT3-TPA3.**

3.2 Surface Morphologies of P(TT-EDOT)

3.2.1 BET analysis

The BET analysis of P(TT-EDOT) indicated a specific surface area of 152 m^2/g, calculated within the relative pressure range of 0.05–0.3 P/P_o, while the Langmuir surface area was determined to be 255 m^2/g in the 30–220 mbar pressure range. The pore size distribution was found to be in the range of 1.4–1.7 nm, suggesting a predominantly microporous structure. Although the material exhibited a relatively low total pore volume, the high surface area implies efficient ion diffusion and accessibility, making it a promising candidate for applications such as energy storage and electrochemical sensing.

3.2.2 SEM analysis

SEM images of the **P(TT-EDOT)** revealed a rough, porous, and sponge-like morphology with highly irregular surface features (Figure 3.6). At 3 μm the polymer exhibited a sponge-like and rough surface texture with interlinked fine domains, which indicates a highly porous morphology (Figure3.6b). At 1 μm, aggregated and bulky

structures were observed, suggesting partial agglomeration but still preserving surface irregularity (Figure 3.6a). The observed morphology is consistent with BET results and indicates a structure favorable for efficient ion diffusion and electrolyte penetration, which are critical for high-performance supercapacitor and electrocatalytic systems.

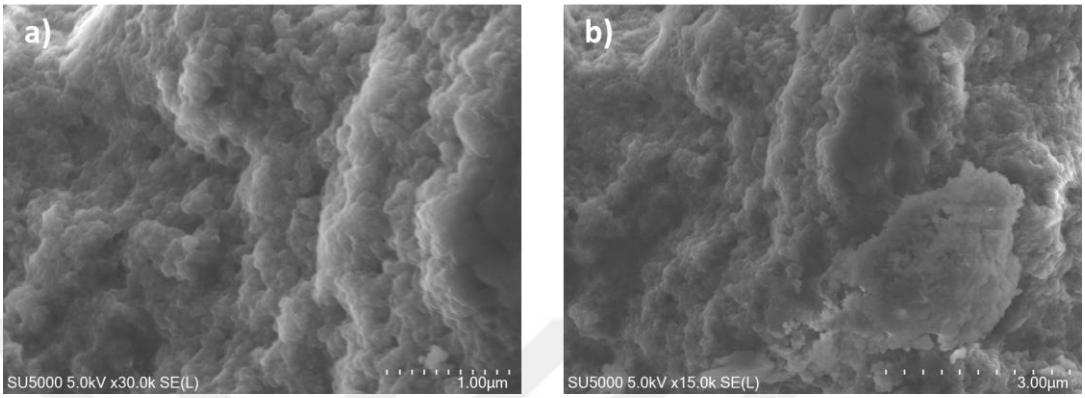

Figure 3.6 : SEM images of **P(TT-EDOT)** at (a) 1 μm and (b) 3 μm.

3.3 Electropolymerization and Electrochemical Characterization of P(TT-Th)

Electrochemical polymerizations of the TT-Th (**4**) was performed in 0.1 M $TBAPF_6$ in ACN:DCM (1:1 v/v), containing 1×10^{-3} M monomer concentration with a scan rate 100 $mV \cdot s^{-1}$, by repetitive cycles at the active range of anodic potentials of the monomer to give the **P(TT-Th)** films (Figure 3.7). For the first range (0.0-1.1 V), no peaks changed on the voltammogram and no film formation was observed on the electrode surface after even 20 cycles (Figure 3.7a and Figure 3.7b). With repeated cycling in the potential range of 0.0–1.6 V, a steady increase in peak currents was observed, indicating the continuous deposition of the monomer onto the electrode surface. The voltammograms revealed that the E_{ox} at 0.94 V and 1.42 V increased with each cycle, confirming the growth of the polymer film on the electrode surface (Figure 3.7c and Figure 3.7d). The last deposition cycles (20th) of the polymer films (Figure 3.7b and Figure 3.7d) indicated that the anodic current of the polymer deposited up to 1.6 V (0.033 mA at 1.42 V) was approximately 82.5 times higher than that of the polymer deposited up to 1.1 V (0.0004 mA at 0.94 V).

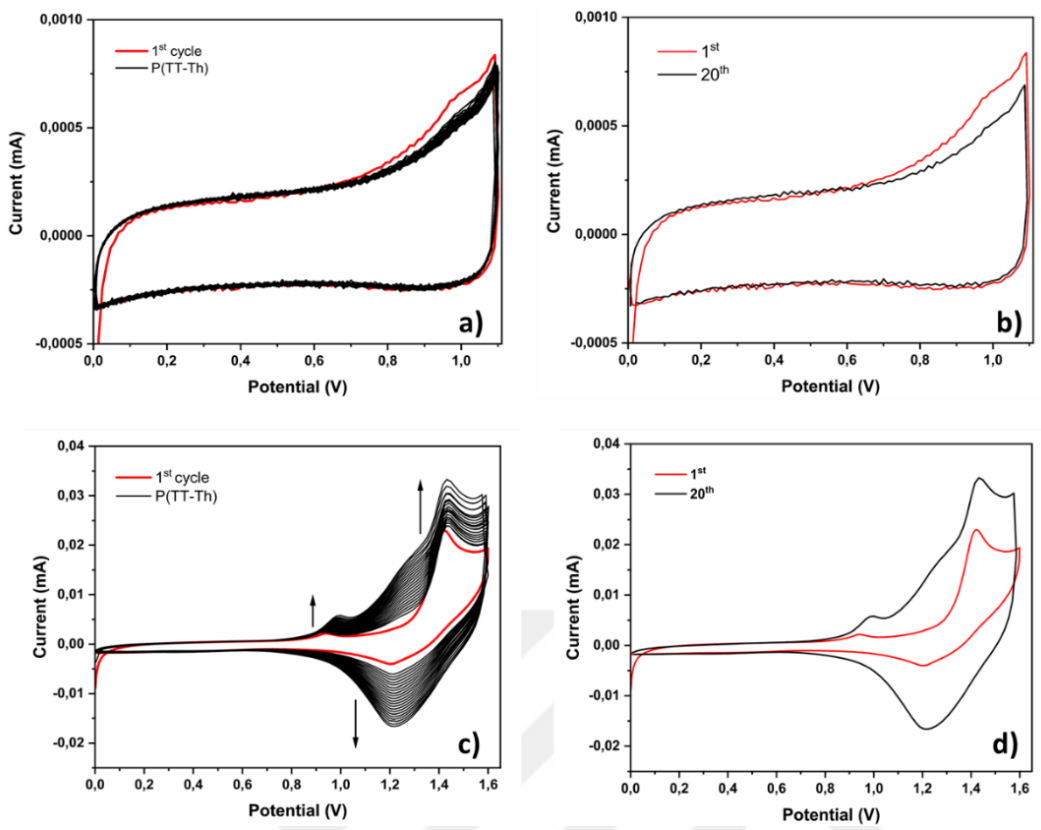

Figure 3.7 : CVs for the polymerization of TT-Th in ACN/DCM (1:1 v/v) containing 0.1 M $TBAPF_6$ at different potential ranges of (a-b) 0.0-1.1 V and (c-d) 0.0-1.6 V, with 100 $mV \cdot s^{-1}$ applied on the GC electrode.

Following electropolymerization, the electrochemical behavior of the resulting polymer films was further examined via CV performed at scan rates ranging from 10 to 1000 $mV \cdot s^{-1}$ in ACN/DCM (1:1 v/v) containing 0.1 M $TBAPF_6$. The CV measurements were performed in the range of 0.0-1.1 V and 0.0-1.6 V, respectively. The polymer film obtained in the narrower potential range (0.0–1.1 V) was not stable, and displayed significantly lower current values across all scan rates, reflecting its limited electrochemical activity (Figure 3.8a). The film synthesized within the 0.0–1.6 V potential range had symmetric anodic and cathodic peak at E_a=1.2 eV. The anodic and cathodic peak current intensities of the polymer within the 0.0-1.6 V potential range increased with the increase in scan rates, which is an indication of ideal capacitive response (Figure 3.8b).

Given that efficient polymer film formation was only achieved within the 0.0–1.6 V potential window, the anodic and cathodic peak current values employed for the analyses presented in Figure 3.9 were exclusively extracted from the electropolymerized sample obtained under these conditions. In order to gain further insight into the charge storage mechanism of the resulting polymer, peak current was

plotted against scan rate, the square root of scan rate, and log(scan rate). The strong linear correlation between peak current and scan rate (R^2 = 0.989 for anodic, 0.996 for cathodic) indicates that the process is largely surface-controlled, consistent with capacitive/psseudocapacitive behavior. The linear dependence of current on the square root of scan rate (R^2 = 0.986 and 0.975, respectively) also suggests that ion diffusion contributes to the overall mechanism. Furthermore, the high correlation coefficients from the log(current) vs. log(scan rate) plots (R^2 = 0.9992 anodic, 0.9976 cathodic) with slopes close to unity confirm that the electrochemical process is predominantly capacitive in nature, with diffusion playing a secondary role.

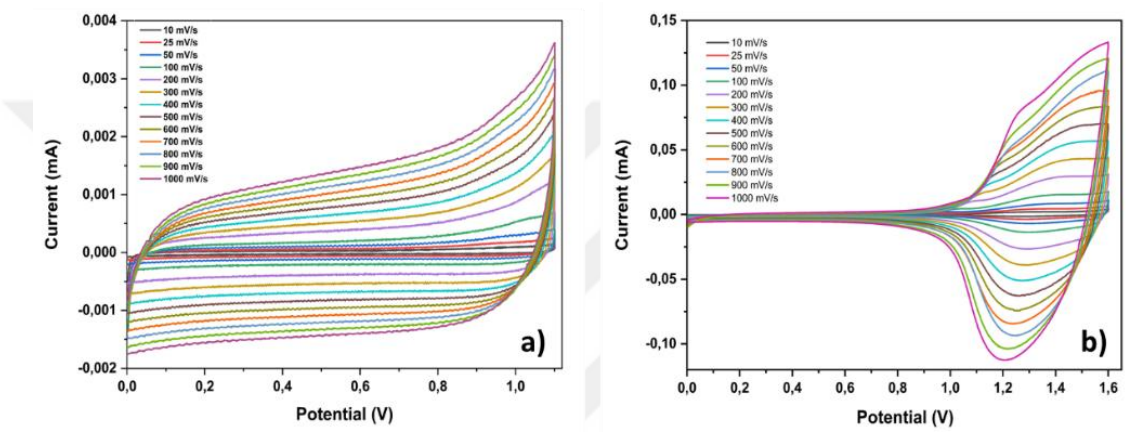

Figure 3.8 : CVs of P(TT-Th) films at different scan rates in ACN/DCM (1:1 v/v) containing 0.1 M $TBAPF_6$ at different potential ranges of (a) 0.0-1.1 V and (b) 0.0-1.6 V.

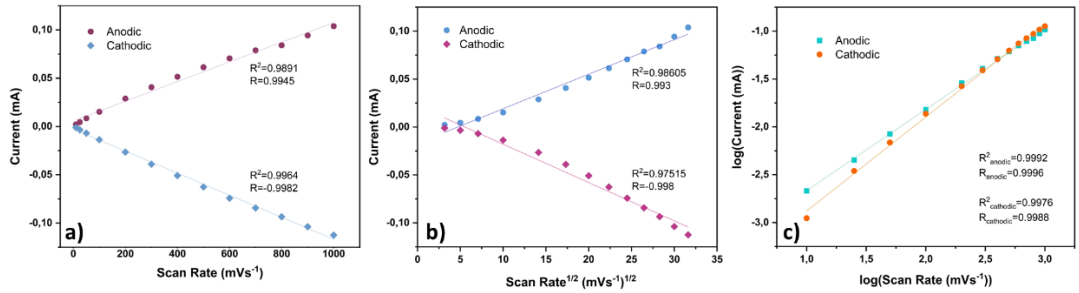

Figure 3.9 : The relationship between (a) current-scan rate (b) current-square root of scan rate, (c) log(current)-log(scan rate) at E_{pa} = 1.42 V and E_{pc} = 1.21 V.

3.4 Optic and Electronic Properties of Monomers

3.4.1 UV-Vis and fluorescence spectrum analysis

Photophysical properties (UV-Vis absorption and emission spectra) of the compounds were investigated in THF solution at room temperature (Table 3.1, Figure 3.10a). The maximum π–π* absorption wavelengths (λ_{max}) of **TT-EDOT3-TPA3** and **TT-Th3-**

TPA3 were measured to be 416 and 431 nm, respectively. From the absorption spectra, the onset maximums of 526 and 531 nm were observed for **TT-EDOT3-TPA3** and **TT-Th3-TPA3**, respectively. Then, the optical band gaps were determined to be 2.33 (**TT-EDOT3-TPA3**) and 2.36 eV (**TT-Th3 TPA3**). The fluorescence measurements in THF displayed emission maxima of 619 (**TT EDOT3-TPA3**) and 616 nm (**TT-Th3-TPA3**) (Table 3.1, Figure 3.10b), demonstrating mega Stokes shifts of 203 and 185 nm, respectively. Both molecules show a Stokes shift higher than 100 nm, indicating that they have a strong intramolecular charge transfer character [34, 60] which could be due to the gaining of more electron donating feature, providing more efficient intramolecular charge-transfer (ICT) between TT and TPA groups. Moreover, mega Stokes shifts of the compounds indicated a fast relaxation from the excited state to the ground state. Thus, owing to ICT, the materials are considered to be optically applicable [90, 91]. In particular, **TT-EDOT3 TPA3** shows a larger Stokes shift (203 nm) compared to **TT-Th3-TPA3** (185 nm) indicating a more effective ICT.

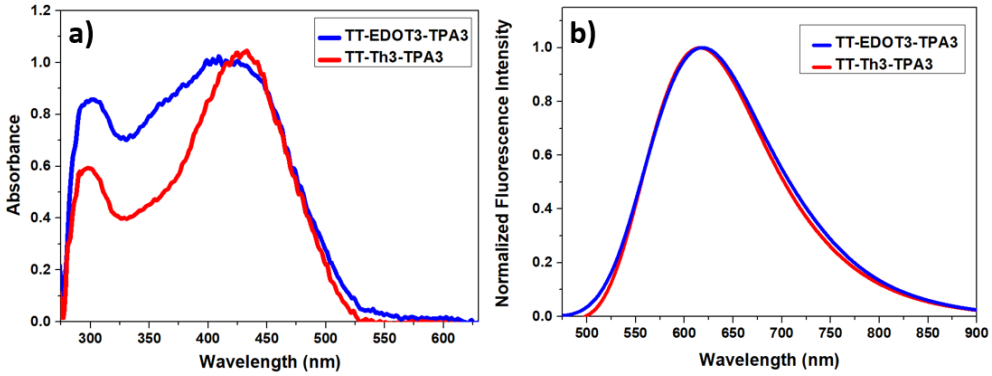

Figure 3.10 : (a) UV-Vis absorption spectra and (b) emission spectra of the **TT-EDOT3-TPA3** and **TT-Th3-TPA3** in THF.

Table 3.1 : Photophysical data of the **TT-EDOT3-TPA3** and **TT-Th3-TPA3**.

Compounds	$\lambda_{abs,\ max}$ [a] (nm)	λ_{onset} [b] (nm)	$\lambda_{fl,\ max}$ [a] (nm)	Stokes Shift (nm)	$E_{g,\ opt}$ [c] (eV)
TT-EDOT3-TPA3	416	526	619	203	2.33
TT-Th3-TPA3	431	531	616	185	2.36

[a] Absorption and emission maximum in THF, [b] Onset of the absorption in THF, [d] $E_{g,\ opt} = hc/\lambda_{onset}$

3.4.2 Electrochemical properties

The HOMO and LUMO energy levels of the two compounds were determined via CV, as shown in Figure 3.11 and summarized in Table 3.2. The electrochemical properties

of **TT-EDOT3-TPA3** and **TT-Th3-TPA3** were investigated using CV in a mixture of ACN:DCM (1:1), with 0.1 M $TBAPF_6$ as the supporting electrolyte. Measurements were conducted at a scan rate of 50 mVs^{-1}, employing platinum wires as the working and counter electrodes, and a silver wire as the reference electrode. HOMO energy levels for **TT-EDOT3-TPA3** and **TT-Th3-TPA3** were calculated to be -5.33 eV and -5.38 eV, respectively, using the equation HOMO = $-(E_{onset, ox} + 4.40)$. LUMO energy levels were then derived from the reduction onset potentials using the formula LUMO = $-(E_{onset, red} + 4.40)$, resulting in values of -3.42 eV for **TT-EDOT3-TPA3** and -3.31 eV for **TT-Th3-TPA3** (Table 3.2). The electronic band gap of TT-EDOT3 TPA3 (1.91 eV) is lower compared to the electronic band gap.

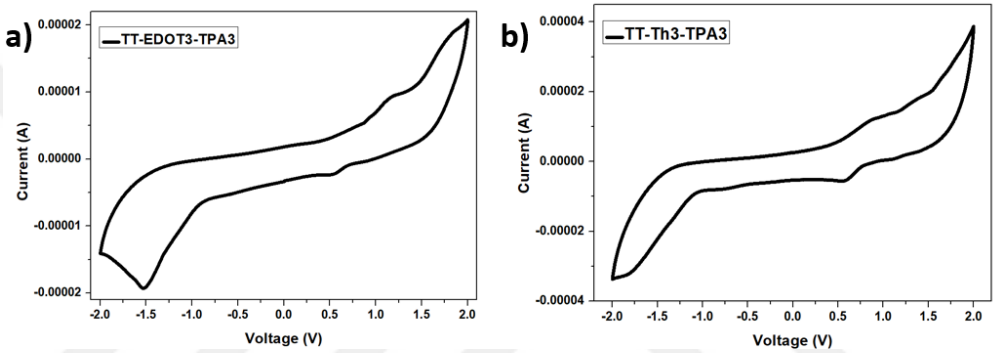

Figure 3.11 : CV spectrum of the **TT-EDOT3-TPA** (a) and **TT-Th3-TPA3** (b).

Table 3.2 : Electrochemical data of the **TT-EDOT3-TPA3** and **TT-Th3-TPA3**.

Compounds	$E_{onset, ox}$ (V)	$E_{onset, red}$ (V)	HOMO[a] (eV)	LUMO[b] (eV)	E_{elec}[c] (eV)
TT-EDOT3-TPA3	0.93	-0.98	-5.33	-3.42	1.91
TT-Th3-TPA3	0.98	-1.09	-5.38	-3.31	2.07

[a] HOMO = $-(E_{onset, ox} + 4.40)$ (eV). [b] LUMO = $-(E_{onset, red} + 4.40)$ (eV). [c] $E_{elec} = |HOMO-LUMO|$

3.5 Thermal Properties of Compounds

The thermal stability of the compounds was evaluated using thermogravimetric analysis (TGA) up to 800 °C, with a heating rate of 10 °C min^{-1} under a nitrogen atmosphere (Figure 3.12). Although both compounds exhibited a similar two-step decomposition profile, their initial decomposition temperatures (corresponding to 5% weight loss) varied depending on their substituents and structural extensions.**TT-EDOT3-TPA3** and **TT-Th3-TPA3** had thermal decomposition temperatures (T_d, 5%) of 422 and 290 °C, respectively. **TT-EDOT3-TPA3** with a longer conjugation and a

strong intramolecular interaction (S···O) between EDOT and TT units displayed the highest thermal stability compared to **TT-Th3-TPA3**. Moreover, with a gradual increase of temperature up to 800 °C, around 58% of **TT-EDOT3-TPA3** and 54% of **TT-Th3-TPA3** remained ash-free, indicating that the compounds have excellent thermal stability despite their small structures, which is a highly desirable parameter for the preparation of a stable and durable electronic material. Morover, the modification ratios were determined from the difference between the thermal mass loss of pristine SWCNT and the hybrid materials as 14.5% (**TT-Th-TPA SWCNT**) and 13.7% (**TT-EDOT-TPA-SWCNT**) (Figure 3.13 and Figure 3.14).

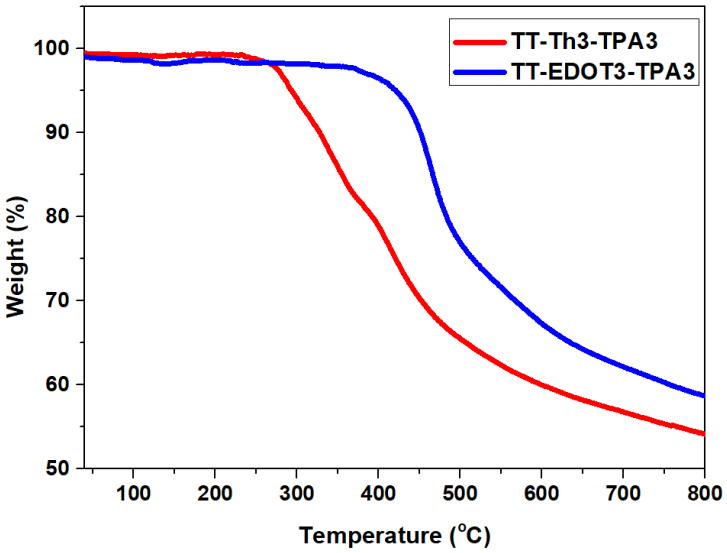

Figure 3.12 : TGA diagram of the **TT-EDOT3-TPA** and **TT-Th3-TPA3.**

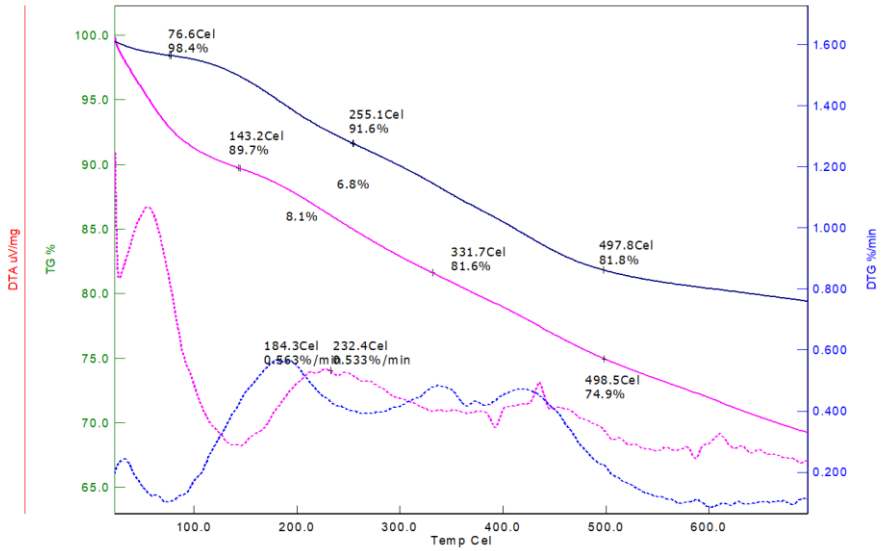

Figure 3.13 : TGA diagram of the **TT-EDOT-TPA-SWCNT** hybrid (blue) and SWCNT (pink).

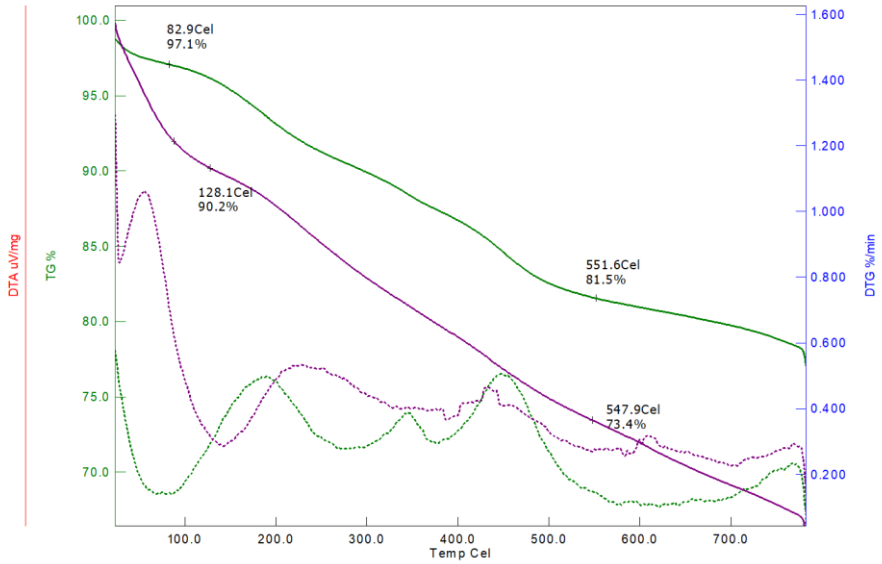

Figure 3.14 : TGA diagram of the **TT-Th-TPA-SWCNT** hybrid (green) and SWCNT (purple).

3.6 Surface Morphology of Hybrid Films

3.6.1 SEM analysis

Surface properties of the hybrid materials were investigated by scanning electron microscopy (SEM). Regarding the SEM images, the hybrid **TT-EDOT-TPA-SWCNT** and **TT-Th-TPA-SWCNT** demonstrated clear interconnected and tangled bundles at different magnifications (Figure 3.15), while the uncoated SWCNT fringes had entanglements with nanometer scaled voids (Figure 3.16a). On the other hand, after modification the voids of SWCNT, it became apparent that the carbon fringes slightly clogged with TT materials, which was considered as an indication for the presence of TTs on the surface of SWCNTs. In addition, while the original uncoated SWCNT is in powder form (Figure 3.16b), the coated SWCNTs were easily dispersed in THF acquiring an excellent film forming property, which could be useful for various opto-electronic applications. In order to further clarify the surface modification of SWCNT with the TT derivatives, the **TT-Th-TPA-SWCNT** and **TT-EDOT-TPA-SWCNT** hybrids were treated with gold nanoparticle solution (2.4 nM), for an Au···S interaction [92, 93]. Clear images of the nanoparticles on the hybrids were demonstrated by scanning electron microscopy (SEM) at 500 nm (Figure 3.17a-b), which indicated clear adsorptions of Au by the sulfur atoms of **TT-Th3-TPA3** and **TT-EDOT3-TPA3** on the SWCNTs.

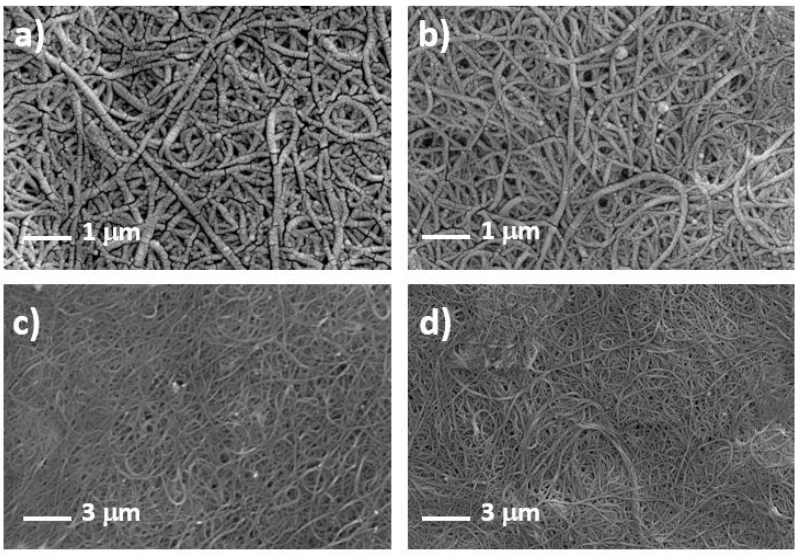

Figure 3.15 : SEM images of (a-c) **TT-Th-TPA-SWCNT** and (b-d) **TT-EDOT-TPA-SWCNT** hybrid films at different magnifications.

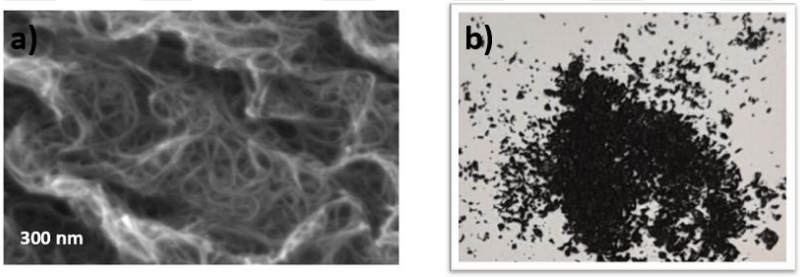

Figure 3.16 : (a) SEM picture of pristine SWCNT at 300 nm and (b) powder form of pristine SWCNT.

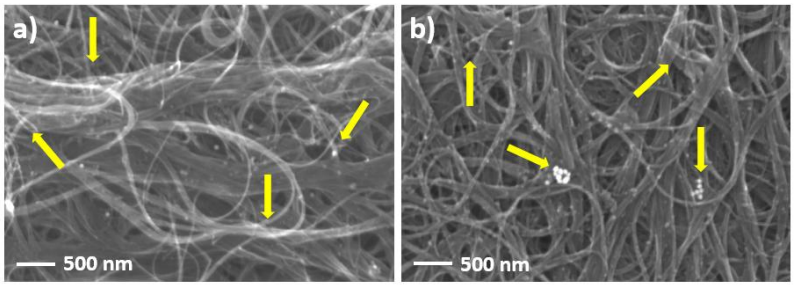

Figure 3.17 : SEM images of the hybrids treated with a gold nanoparticle solution at 500 nm: (a) **TT-Th-TPA-SWCNT** and (b) **TT-EDOT-TPA-SWCNT.**

3.6.2 AFM analysis

Further surface properties of the hybrid nanomaterials were investigated by atomic force microscopy (AFM) (Figure 3.18a-d). RMS roughness, obtained from the cross section of the AFM images, were determined to be 26 nm for **TT-Th-TPA-SWCNT** and 24 nm for **TT-EDOT-TPA-SWCNT**, demonstrating uniform and smooth surface morphologies. Considering our previous studies on flexible film formation between

electron donor groups and SWCNT, formation of the flexible film and these characterizations are consistent with the previous studies [92, 93].

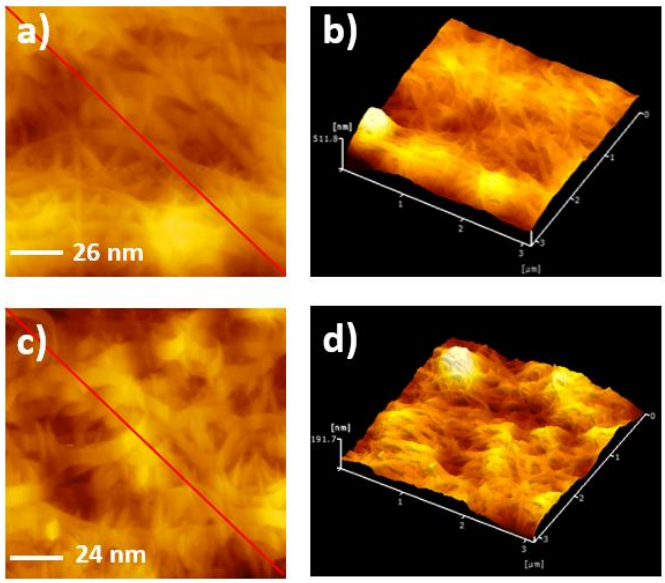

Figure 3.18 : AFM images of (a and b) **TT-Th-TPA-SWCNT** and (c and d) **TT-EDOT-TPA-SWCNT** hybrid films at different magnifications.

3.7 Supercapacitor Studies of Hybrid Films

3.7.1 CV analysis

Cyclic voltammetry (CV) measurements at different scan rates to observe the C-rate capabilities of binder-free and freestanding electrodes were conducted to examine the electrochemical behaviors of the electrodes. Thus, although three cycles were obtained at scan rates of 1000, 750, 500, 250, 100, 75, 50, 25, 10, 5, and 1 $mV.s^{-1}$, the second one is presented for each measurement (Figure 3.19). Even at a high scan rate of 1000 $mV.\ s^{-1}$, **TT-EDOT-TPA-SWCNT** exhibited capacitive behavior, and the area under the curves increased with increasing scan rate (Figure 3.19a), which is an indication of electrode material's potential for a good C-rate performance [94]. Analysis of the voltammogram obtained at 100 $mV{\cdot}s^{-1}$ revealed an oxidation peak at approximately 500 mV and a reduction peak at around 300 mV (Figure 3.19b), which was attributed to the presence of EDOT in the structure. The relatively low current response at low scan rates was due to electric double-layer capacitance, while the improved response at higher scan rates with pseudocapacitive behavior resulted from ongoing redox processes at the electrode–electrolyte interface. Despite this, the CV shape remained well preserved even at high scan rates, demonstrating the device's superior rate

capability [94]. The results indicated that the **TT-EDOT-TPA-SWCNT** electrode performs well across a wide range of current densities with high specific capacitance [92, 95–97].

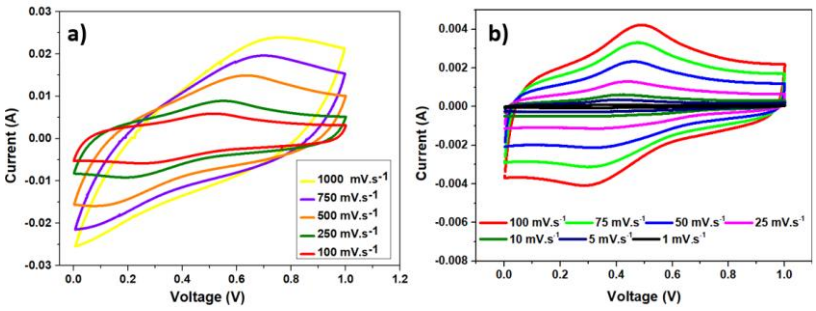

Figure 3.19 : CVs for **TT-EDOT-TPA-SWCNT** obtained at scan rates (a) between 1000 and 100 $mV \cdot s^{-1}$ and (b) between 100 and 1 $mV \cdot s^{-1}$ (electrolyte 85% H_3PO_4, separator: cellulose acetate).

Similar measurements were conducted using an electrochemical cell prepared with the **TT-Th-TPA-SWCNT** electrodes (Figure 3.20). The amount of current delivered by this active material through voltage scanning was not as high as that of the **TT-EDOT-TPA-SWCNT** electrode. On the other hand, while the area under the voltammograms showed a limited increase with increasing scan rate, the voltammograms exhibited bending trends at the minimum and maximum voltage points. This indicates that the **TT-Th-TPA-SWCNT** electrode cannot be charged at high current densities comparable to **TT-EDOT-TPA-SWCNT** [95, 98, 99]. The **TT-Th-TPA-SWCNT** electrode exhibited an oxidation peak at approximately 250 mV at a scan rate of 100 $mV \cdot s^{-1}$, and with decreasing scan rate, there was a decreasing trend in the area under the CV curves compared to measurements conducted at a scan rate of 1 $mV.s^{-1}$. At a scan rate of 1 $mV \cdot s^{-1}$, the shape of the voltammogram became distorted and the electrode did not exhibit capacitive behavior, indicating that, at very low current densities, this electrode active material may not perform effectively.

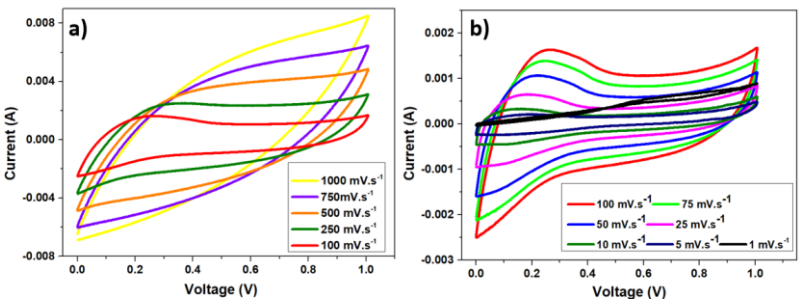

Figure 3.20 : CVs for **TT-Th-TPA-SWCNT** obtained at scan rates (a) between 1000 and 100 $mV.s^{-1}$ and (b) between 100 and 1 $mV.s^{-1}$ (electrolyte 85% H_3PO_4, separator: cellulose acetate).

3.7.2 Specific capacitance

The specific capacitance data calculated from voltammograms of different scan rates are plotted *vs* scan rates to compare the specific capacitance performance of the two-active materials, with the specific capacitances (C_{CV}) calculated using Equation 1 (Figure 3.21a).

$$C_{CV} = \frac{2}{m(WE)k(V_2 - V_1)} \int_{V_1}^{V_2} IdV \quad (1)$$

In equation (1), the term m(WE) (g) signifies the mass of the working electrode that is in contact with the electrolyte. The parameter k represents the scan rate employed in the cyclic voltammetry (CV) measurements. V_1 and V_2 refer to the minimum and maximum voltages, respectively, utilized in the range for determining C_{CV} [100, 101].

While the **TT-EDOT-TPA-SWCNT** electrode exhibited a C_{CV} of 153.8 ± 4.2 $F \cdot g^{-1}$ at a scan rate of 1 $mV \cdot s^{-1}$, the **TT-Th-TPA-SWCNT** electrode did not exhibit capacitive behavior at the same scan rate, thus, no specific capacitance calculation was performed. On the other hand, at a scan rate of 5 $mV \cdot s^{-1}$, **TT-EDOT-TPA-SWCNT** displayed a C_{CV} of 125.5 ± 0.5 $F \cdot g^{-1}$, while **TT-Th-TPA-SWCNT** exhibited a C_{CV} of 81.6 ± 2.3 $F \cdot g^{-1}$. Furthermore, **TT-EDOT-TPA-SWCNT** demonstrated a good C-rate performance with increasing scan rate, achieving approximately 36.6 ± 4.25 $F \cdot g^{-1}$ C_{CV} even at the highest scan rate. In contrast, this value remained considerably lower for the **TT-Th-TPA-SWCNT** electrode, which indicated that **TT-EDOT-TPA-SWCNT** operates across a wide range of current densities, while **TT-Th-TPA-SWCNT** demonstrates performance with a relatively limited C-rate window and capability. Subsequently, EIS measurements were conducted to analyze the resistance behavior offered by the two different cells and compared with the CV results (Figure 3.17b). Both cells exhibited overlapped Nyquist plots, which consisted of two semi-circles and a straight line at approximately 45 degree. To fit both Nyquist plots, an equivalent circuit model was employed using constant phase elements (CPEs) instead of ideal capacitive semi-circles, due to the initial phase angles of the semi-circles in the equivalent circuit. This approach accommodates the characteristics of the electrodes more accurately [102]. The R_s in the equivalent circuit represents the total resistance originating from the electrolyte and the connections between the supercapacitor device and the test equipment [103]. R_{ct-1} and CPE1 represent the charge transfer resistance and the CPE for the electronic transfer processes of the electrode active material. R_{Leak}

is the leakage resistance placed in parallel with CPE2, typically very high and negligible in the circuit and CPE3 represents capacitance, arising from charge transfer processes of SWCNT electrode. Therefore, a second charge transfer resistance (R_{ct-2}), representing the resistance of SWCNT to electron transfer and a CPE3, connected in parallel, were included in the equivalent circuit system. R_{ct-2} originates from the SWCNT present in the flexible and binder-free electrode structure. A Warburg component, connected in series with this resistance, was added to the equivalent circuit to represent mass transfer to signify the diffusion of ions into the porous carbon structure [104]. This equivalent circuit model was used to accurately fit the impedance data obtained from both Nyquist plots. The resistance values obtained for the two different electrodes are given in Table 3.3. As expected, the **TT-EDOT-TPA-SWCNT** electrode exhibited lower R_s, R_{ct-1} and R_{ct-2} values compared to the **TT-Th-TPA-SWCNT** electrode. This indicates that a supercapacitor cell prepared with this electrode displays a better electron transfer capability, which is consistent with the previously obtained CV results. Although symmetric supercapacitor cells were prepared using the same electrolyte for both electrode active materials, the cell prepared with the **TT-EDOT-TPA-SWCNT** electrode exhibited a lower R_s compared to the cell prepared with the **TT-Th-TPA-SWCNT** electrode. As previously mentioned, R_s represents the total resistance originating from the electrolyte and the connections between the potentiostat and the supercapacitor device. We believe this difference reflects the fact that the **TT-EDOT-TPA-SWCNT** electrode, with its higher electrical conductivity, forms a more electrically conductive interface between the potentiostat and the supercapacitor device [105].

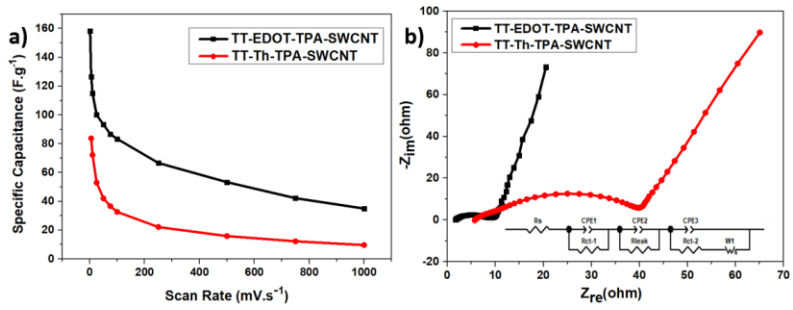

Figure 3.21 : (a) Specific capacitance values obtained at different scan rates (1000, 750, 500, 250, 100, 75, 50, 25, 10, 5, and 1 $mV \cdot s^{-1}$) for **TT-EDOT-TPA-SWCNT** and **TT-Th-TPA-SWCNT** electrodes using 85 % H_3PO_4 electrolyte and cellulose acetate as seperator. (b) Nyquist plots of **TT-EDOT-TPA-SWCNT** and **TT-Th-TPA-SWCNT** electrodes recorded using 85% H_3PO_4 electrolyte and cellulose acetate as seperator over the frequency range of 100000 Hz to 0.1 Hz with an applied AC amplitude of 10 mV.

Table 3.3 : The resistance values calculated from the fitting of the experimentally obtained Nyquist curves using the equivalent circuit model shown in Figure 3.21b.

Materials	EIS			GCD	
	R_s	R_{ct-1}	R_{ct-2}	E ($Wh.kg^{-1}$)	P ($W.kg^{-1}$)
TT-EDOT-TPA-SWCNT	1.6	2.5	5.4	5.19 ± 0.13 ($0.1\ A\cdot g^{-1}$) 2.00 ± 0.12 ($20\ A\cdot g^{-1}$)	50 ($0.1\ A\cdot g^{-1}$) 10000 ($20\ A\cdot g^{-1}$)
TT-Th-TPA-SWCNT	5.8	29.9	3.4	0.2.30 ± 0.14 ($1\ A\cdot g^{-1}$) 0086 ± 0.00058 ($10\ A\cdot g^{-1}$)	500 ($1\ A\cdot g^{-1}$) 5000 ($10\ A\cdot g^{-1)}$

Due to the conjugation in the thiophene structure, π orbital overlap occurs along the backbone of the molecule, which promotes electron transport. Similarly, the electrical conductivity of thiophene structures can be enhanced through chemical modifications. On the other hand, EDOT reduces the effective mass of charge carriers and the HOMO-LUMO gap [106]. The Th and EDOT structures were functionalized as bridging molecules between TT and TPA, with Th in the first hybrid structure and EDOT in the second. The results show that the **TT-EDOT3-TPA3** structure exhibits a lower electronic band gap (1.91 eV) compared to that of **TT-Th3-TPA3** (2.07 eV). This implies that the **TT-EDOT-TPA-SWCNT** electrode can facilitate electron transfer with lower charge transfer resistance within the same electrolyte. Accordingly, the CV and EIS results, obtained in two-electrode cells, corroborate the band gap values previously observed in the three-electrode electrochemical cell. In addition, electron donor and intramolecular O···S interactions of EDOT highly contributed to its capacitive performance as well as its optical properties [107, 108].

The performance difference between the two electrodes is not solely due to the lower electronic band gap provided by EDOT. The enhanced interaction of the **TT-EDOT-TPA-SWCNT** electrode with the aqueous electrolyte further deepens the performance gap between the two active materials. The **TT-EDOT-TPA-SWCNT** electrode exhibits superior wettability in the H_3PO_4 electrolyte, which is clearly reflected in the R_s values obtained from the EIS results. Similarly, the Warburg impedance observed in the Nyquist plots indicates that ions in the electrolyte can achieve more efficient mass transfer to the electrode surface.

3.7.3 GCD measurements

In the subsequent process, GCD measurements were performed at different current densities, and the charge-discharge characteristics of the electrodes were experimentally investigated. Thus, the electrodes were charged and discharged at current densities of 20, 15, 10, 5, 2.5, 2, 1, 0.5, 0.1, and 0.05 $A \cdot g^{-1}$. The specific capacitance (C_{GCD}), energy density (E), and power density (P) values offered by both electrodes at different current densities were calculated using the obtained GCD curves and Equations 2, 3, and 4, respectively. The cells subjected 10 charge-discharge cycles at each current density, and the curves obtained at the 5th cycle for each current density are presented (Figure 3.22a and 3.22b).

$$C_{GCD} = \frac{4I\Delta t}{m\Delta V} \quad (2)$$

$$E = \frac{C_{GCD}\Delta V^2}{3.6x8} \quad (3)$$

$$P = \frac{3600E}{\Delta t} \quad (4)$$

In Equations 2, 3 and 4, I (A) represents the applied current magnitude during the GCD test, Δt (s) denotes the discharge time obtained during the test, m (g) is the total mass of the two electrodes used in the preparation of the cell and ΔV (V) refers to the voltage window (V_2-V_1), in which the charge-discharge process was conducted [109, 110].

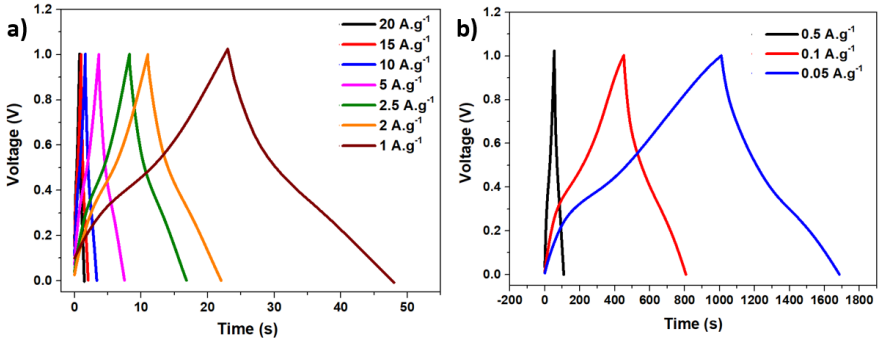

Figure 3.22 : GCD curves for the **TT-EDOT-TPA-SWCNT** electrode at current densities of (a) 20, 15, 10, 5, 2.5, 2, and 1 $A \cdot g^{-1}$ and (b) 0.5, 0.1, and 0.05 $A \cdot g^{-1}$ (electrolyte 85% H_3PO_4, separator: cellulose acetate).

A decrease of charge-discharge time was observed with an increase of current density, yet the **TT-EDOT-TPA-SWCNT** electrode provided consistent charge-discharge curves at all current densities. Except for the 0.05 $A \cdot g^{-1}$ current density, all charge-

discharge tests exhibited Coulombic efficiencies above 95%. The lower efficiency at 0.05 $A \cdot g^{-1}$ was attributed to the difficulty in charging the cell at such a low current density. Nevertheless, the electrode was able to charge and discharge even at this very low current density of 0.05 $A \cdot g^{-1}$. Additionally, the obtained charge-discharge (GCD) curves are highly consistent with the CV results. During charging, a bend representing an oxidation peak took place at around 400 mV, while during discharging, a bend representing a reduction peak was observed at around 300 mV in the GCD curves.

The GCD curves are generally triangular, symmetrical and exhibit charge-discharge behavior over a wide range of current densities, indicating that the **TT-EDOT-TPA-SWCNT** electrode operates with high coulombic efficiency and demonstrates a good C-rate capability. To compare the GCD performances of the **TT-EDOT-TPA-SWCNT** and **TT-Th-TPA-SWCNT** electrodes, the discharge curves obtained at a current density of 1 $A \cdot g^{-1}$ are given in Figure 3.23a. **TT-Th-TPA-SWCNT** exhibited a lower coulombic efficiency compared to the **TT-EDOT-TPA-SWCNT** electrode. Additionally, the discharge curve indicated that the C_{GCD} of **TT-Th-TPA-SWCNT** is not as high as that of the **TT-EDOT-TPA-SWCNT** electrode. The C_{GCD} data calculated from the charge-discharge curves for both electrodes are shown in Figure 3.23b. Using 10 repeated GCD measurements, the average C_{GCD} and standard deviations were calculated for each current density. The calculated standard deviations are presented as error bars along with the mean C_{GCD} values. The **TT-EDOT-TPA-SWCNT** electrode provided a C_{GCD} of approximately 149.7 ± 3.7 $F \cdot g^{-1}$ at a current density of 0.1 $A \cdot g^{-1}$. On the other hand, this current density was insufficient to charge the **TT-Th-TPA-SWCNT** electrode, and no specific capacitance was obtained at this current density. The C_{GCD} values at current density of 0.5 $A \cdot g^{-1}$ for the **TT-EDOT-TPA-SWCNT** and **TT-Th-TPA-SWCNT** electrodes were calculated to be 109.2 ± 1.4 $F \cdot g^{-1}$ and 66.3 ± 3.9 $F \cdot g^{-1}$, respectively. These results displayed a high correlation with the results obtained from CV measurements. Similarly, the **TT-Th-TPA-SWCNT** electrode did not exhibit charge-discharge behavior at current densities of 15 and 20 $A.g^{-1}$, which highlighted the synergistic effect of the components within the **TT-EDOT-TPA-SWCNT** structure, demonstrating its high performance and a good C-rate capability.

Subsequently, a 10000-cycle GCD test was conducted at a current density of 2 $A \cdot g^{-1}$ to examine the stability of the two electrode active materials. The capacity retention

data obtained as a function of cycle number are given in Figure 3.24. The 10000-cycle stability graphs show that the **TT-EDOT-TPA-SWCNT** electrode exhibited approximately a 10% increase in capacity within the first 500 cycles, maintaining nearly the same specific capacity for the remainder of the test. As expected, the **TT-Th-TPA-SWCNT** electrode initially provided a slightly lower specific capacitance compared to the **TT-EDOT-TPA-SWCNT** electrode and displayed a decreasing capacity trend with increasing cycle numbers. These results demonstrated that the **TT-EDOT-TPA-SWCNT** electrode offers an excellent cycling stability, over 95% coulombic efficiency, a high specific capacitance, a good C-rate capability and high energy and power densities. The specific capacitance ($F \cdot g^{-1}$), power density ($W \cdot kg^{-1}$), energy density ($Wh \cdot kg^{-1}$), and capacity retention (%) data obtained with the symmetric supercapacitor cell, prepared using **TT-EDOT-TPA-SWCNT** electrodes, are presented comparatively in Table 3.4.

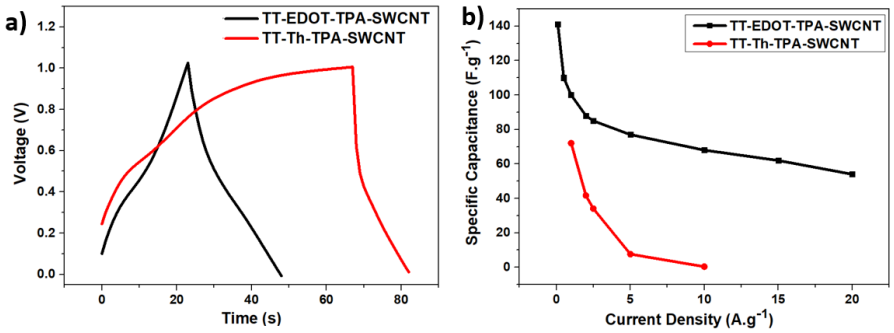

Figure 3.23 : (a) GCD curves for the **TT-EDOT-TPA-SWCNT** and **TT-Th-TPA-SWCNT** electrodes at a current density of 1 $A \cdot g^{-1}$. (b) Specific capacitance values calculated from GCD curves for the **TT-EDOT-TPA-SWCNT** and **TT-Th-TPA-SWCNT** electrodes at different current densities (electrolyte 85% H_3PO_4, separator: cellulose acetate).

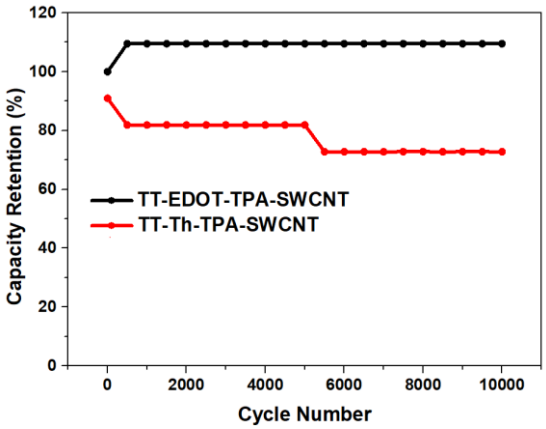

Figure 3.24 : Cycling stability graph for the **TT-EDOT-TPA-SWCNT** and **TT-Th-TPA-SWCNT** electrodesat a current density of 2 $A \cdot g^{-1}$ (in both supercapacitor cells, the electrolyte is 85 wt% H_3PO_4 and the separator is cellulose acetate).

Table 3.4 : The performance indicators obtained with the supercapacitor cell prepared using the **TT-EDOT-TPA-SWCNT** electrode compared with data obtained in some other studies in the literature.

Electrode	Specific Capacitance ($F.g^{-1}$)	Power Density ($W.kg^{-1}$)	Energy Density ($Wh.kg^{-1}$)	Capacity Retention (%)	Ref.
Ti/MoS_2	133 (1 $A.g^{-1}$)	530	11	93% (1000 cyc./ 1 $A.g^{-1}$)	[111]
Porous 3D interconnected carbon framework	65 (0.2 $A.g^{-1}$)	400	12	100% (3000 cyc./ 1 $A.g^{-1}$)	[112]
Mxene/Graphdiyne nanotubes	337.4 (2 $A.g^{-1}$)	750	19.7	88.2% (10000 cyc./ 8 $A.g^{-1}$)	[113]
Paper/Activated carbon	165 (5 $mA.cm^{-2}$)	28.22	6.01	100% (10000 cyc./ 5 $mA.cm^{-2}$)	[114]
PANI/CNF	234 (1 $A.g^{-1}$)	500	32	90% (1000 cyc./ 1 $A.g^{-1}$)	[115]
Ni foams/PPy	38 (0.2 $A.g^{-1}$)	6200	14	82% (2000 cyc./ 1 $A.g^{-1}$)	[116]
CNTs/Nitrogen-doped carbon polyhedral hybrids	135 (5 $mV.s^{-1}$)	250	12	100% (20000 cyc.)	[117]
Graphene/MnO_2/ CNTs	61 (0.1 $A.g^{-1}$)	106	8.9	95% (1000 cyc./ 4 $A.g^{-1}$)	[118]
TT-EDOT-TPA-SWCNT	149.7 ± 3.7 (1 $A.g^{-1}$)	10000 (@20 $A.g^{-1}$) 50 $W.kg^{-1}$ (@0.1 $A.g^{-1}$)	5.19 ± 0.13 (@0.1 $A.g^{-1}$) 2.00 ± 0.12 (@20 $A.g^{-1}$)	110% (10000/ 2 $A.g^{-1}$)	**This work**

3.8 Surface Morphology of Before and After Cycling Test

After the charge-discharge cycling tests, the surface morphology of the **TT-EDOT-TPA-SWCNT** and **TT-Th-TPA-SWCNT** electrodes were re-examined using SEM analysis (Figure 3.25a-d). The SEM images did not show any substantial changes in

the measurements before and after the cycles of GCD testing for both hybrid electrodes. Similar interconnected and tangled bundles are clearly visible before and after 10000 cycles, indicating the high stability of the hybrid electrodes during charge-discharge cycles. On the other hand, when examining the SEM image of the **TT-EDOT-TPA-SWCNT** electrode before GCD, aggregation formations belonging to SWCNT were observed. However, when the morphology of the electrode after 10000 GCD cycling was examined, it was noticed that the aggregated structures disappeared, the morphology became more porous, and it was observed that the **TT-EDOT3-TPA3** molecules are embedded into the CNT framework. SEM images taken prior to the GCD tests reveal that the **TT-EDOT-TPA-SWCNT** electrode exhibits a more integrated structure, with SWCNT nanofibers forming large bundles that appear interconnected and cohesive, although the nanotube network is randomly entangled and shows a relatively disordered distribution. After 10000 GCD cycles, however, partial debonding of the SWCNT bundles is observed, resulting in a more homogeneous distribution and a morphology resembling a three-dimensional mesh. This indicates that the morphology of the electrode changes upon wetting with the acidic media, or alternatively, the electrochemical process itself may have triggered such a morphological transformation on the surface, providing a larger surface area for electrochemical interaction [119, 120]. On the other hand, the absence of any capacity loss after 10000 cycles suggests that the π–π interactions within the electrode structure remain intact and that the electrode retains its structural integrity without degradation. A similar situation is not present in the SEM images of the **TT-Th-TPA-SWCNT** electrodes recorded after 10000 cycles of GCD. This suggests that the increase in porosity of the **TT-EDOT-TPA-SWCNT** electrode and a better adhesion between the **TT-EDOT3-TPA3** molecules with the SWCNT framework after use provides a better electrode-electrolyte interface, which may lead to a decrease in electron transfer resistance. To validate this, we compared the Nyquist plot of the cell subjected to 30 potentiostatic and 90 galvanostatic charge-discharge cycles with that of the freshly prepared cell. The Nyquist plots obtained from the freshly prepared cell and the cell aged for 120 cycles using the **TT-EDOT-TPA-SWCNT** electrodes are presented in Figure 3.26. Although there was no significant change in the R_s, with the increasing number of cycles, the R_{ct} of the electrode showed a notable decrease. This result is in agreement with the 10000-cycle GCD tests performed with the cell prepared using the **TT EDOT-TPA-SWCNT** electrodes and explains why the cell performance improves

during the first few hundred usage cycles. Furthermore, the electrochemical performance of **TT-EDOT TPA-SWCNT** competed with and outperformed many SWCNT based materials as well as other CNT-based materials (Table 3.5).

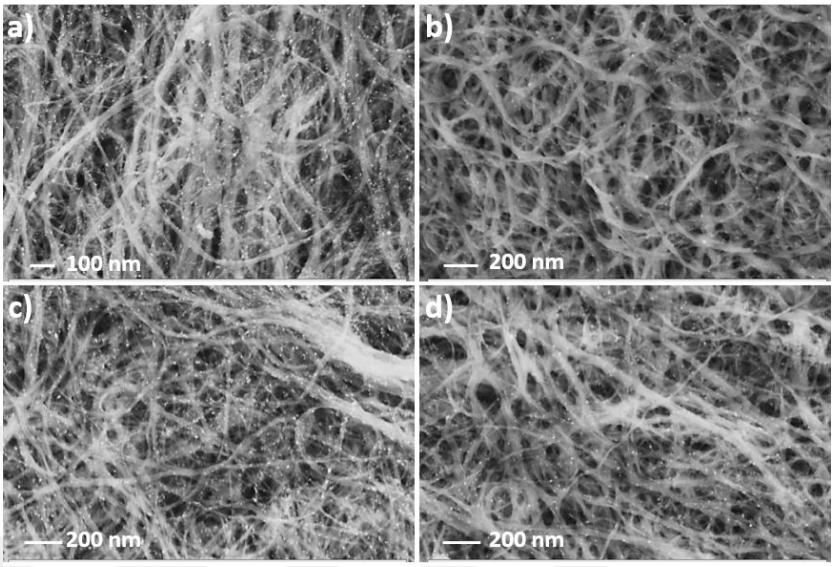

Figure 3.25 : SEM image of the **TT-EDOT-TPA-SWCNT** electrode (a) before 10000 cycles of GCD testing and (b) after 10000 cycles of GCD testing. SEM image of the **TT-Th-TPA-SWCNT** electrode (c) before 10000 cycles of GCD testing and (d) after 10000 cycles of GCD testing (in both supercapacitor cells, the electrolyte is 85 wt% H_3PO_4 and the separator is cellulose acetate).

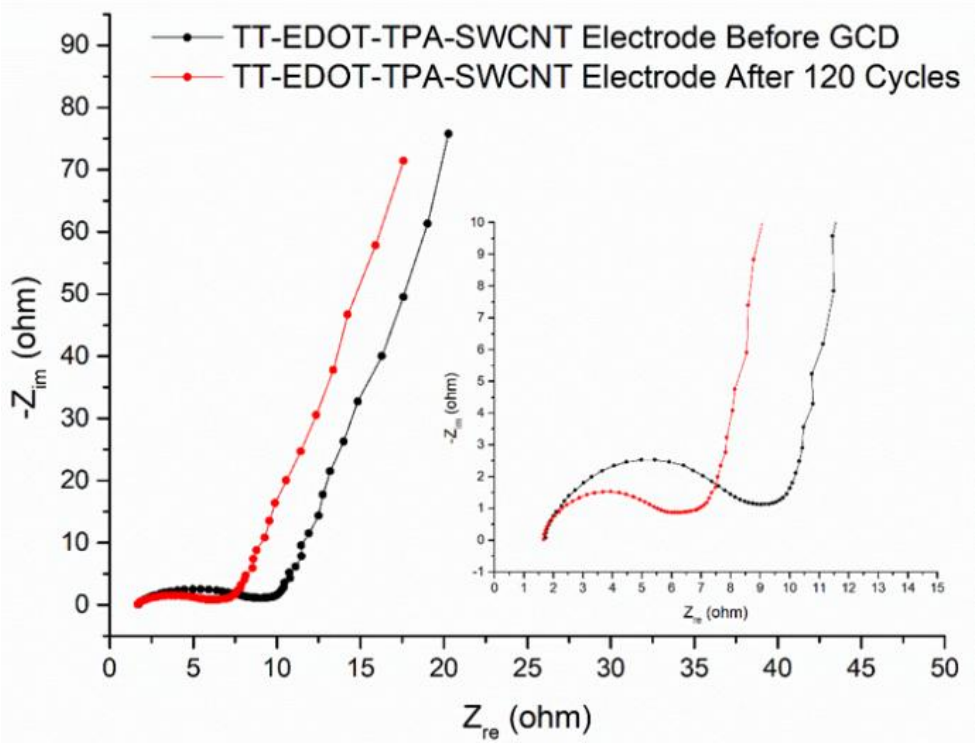

Figure 3.26 : The Nyquist plots of the freshly prepared cell and the cell aged for 120 cycles using **TT-EDOT-TPA-SWCNT** electrodes.

Table 3.5 : Performance comparison of **TT-EDOT-TPA-SWCNT** electrode with SWCNT based supercapacitor electrodes in literature.

Electrode	Specific Capacitance ($F.g^{-1}$)	Power Density ($W.kg^{-1}$)	Energy Density ($Wh.kg^{-1}$)	Capacity Retention (%)	Ref.
SWCNT/ KOH + PPD	162.66 (1 $A.g^{-1}$)	2790	4.23	96.51% (4000 cyc./ 1 $A.g^{-1}$)	[121]
PEDOT-PSS/SWCNTs	104 (0.2 $A.g^{-1}$)	825	7	90% (1000 cyc./ 1 $A.g^{-1}$)	[122]
SWCNT on PDMS	34.2 (0.63 $A.g^{-1}$)	21100	18000	94% (500 cyc./ 1.5 $A.g^{-1}$)	[123]
Graphene/CNT	290.4 (0.5 $A.g^{-1}$)	58.5	62.8	129% (1000 cyc./ 2 $A.g^{-1}$)	[124]
TT-EDOT-TPA-SWCNT	149.7 ± 3.7 (1 $A.g^{-1}$)	10000 (@20 $A.g^{-1}$) 50 $W.kg^{-1}$ (@0.1 $A.g^{-1}$)	5.19 ± 0.13 (@0.1 $A.g^{-1}$) 2.00 ± 0.12 (@20 $A.g^{-1}$)	110% (10000/ 2 $A.g^{-1}$)	**This work**

4. CONCLUSION

In conclusion, we designed and synthesized highly conjugated thienothiophene (TT) based compounds, **TT-EDOT3-TPA3** and **TT-Th3-TPA3**, possessing EDOT, thiophene (Th) and triphenylamine (TPA) units and porous organic polymers P(TT-EDOT) and P(TT-Th).

BET analysis of **P(TT-EDOT)** showed a specific surface area of 152 m^2/g and a Langmuir surface area of 255 m^2/g, with a pore size distribution of 1.4–1.7 nm, indicating microporosity. SEM images revealed a rough, porous, and spongy morphology containing interconnected domains and partially aggregated bulk structures, consistent with its microporous structure.

Electropolymerization of TT-Th, **P(TT-Th)**, yielded no film formation in the 0.0–1.1 V range, whereas steady polymer growth with increasing peak currents was observed in the 0.0–1.6 V range. The voltammograms displayed two oxidation peaks at 0.94 V and 1.42 V. CV analysis showed well-defined and nearly symmetric redox peaks, with peak currents increasing proportionally to the scan rate. The high correlation coefficients obtained from scan rate–dependent and log–log plots confirmed consistent electrochemical behavior, indicating that the charge storage mechanism is predominantly surface-controlled (capacitive/pseudocapacitive), with an additional contribution from diffusion-controlled processes.

The compounds TT-EDOT3-TPA3 and TT-Th3-TPA3 were attached onto single-walled carbon nanotubes (SWCNTs) through noncovalent interactions—namely van der Waals forces, π–π stacking, and S–π interactions—without the need for additional binding agents. This process resulted in the formation of novel hybrid nanomaterials, **TT-EDOT-TPA-SWCNT** and **TT-Th-TPA-SWCNT**, which were obtained as flexible and uniform films. Among them, the **TT-EDOT-TPA-SWCNT** hybrid electrode exhibited outstanding supercapacitor and energy storage performance, including a high specific capacitance of 158 $F \cdot g^{-1}$ at 1 $mV \cdot s^{-1}$, an impressive power density of 10000 $W \cdot kg^{-1}$ at 20 $A \cdot g^{-1}$, and a maximum energy density of 5.32 $Wh \cdot kg^{-1}$

at 0.1 $A \cdot g^{-1}$. Additionally, it demonstrated excellent charge–discharge reversibility and long-term cycling stability, maintaining performance over 10000 cycles. Compared to previously reported free-standing supercapacitor electrodes, **TT-EDOT-TPA-SWCNT** outperformed and competed the performance of many other SWCNT-based hybrid materials in the literature [125–129].

These findings highlight the great potential of TT-based conjugated polymers and their hybrid nanomaterials for advanced energy storage applications and pave the way for future developments in flexible, high-performance supercapacitor devices.

REFERENCES

[1] **Cacialli, F.** (2000). Organic semiconductors for the new millennium. *Philosophical Transactions of the Royal Society of London. Series A: Mathematical, Physical and Engineering Sciences*, ***358***, 173-192.

[2] **Turkoglu, G., Cinar, M. E., & Ozturk, T.** (2019). Thiophene-Based Organic Semiconductors. In *Topics in Current Chemistry Collections* (pp. 79–123). Topics in Current Chemistry Collections.

[3] **Costa, J. C., Taveira, R. J., Lima, C. F., Mendes, A., & Santos, L. M.** (2016). Optical band gaps of organic semiconductor materials. *Optical Materials*, ***58***, 51-60.

[4] **Brütting, W.** (2006). Introduction to the Physics of Organic Semiconductors (pp. 1–14). Physics of Organic Semiconductors.

[5] **Milián-Medina, B., & Gierschner, J.** (2012). π-Conjugation. *Wires Computational Molecular Science*, ***2***, 513–524.

[6] **Namsheer, K., & Rout, C. S**. (2021). Conducting polymers: a comprehensive review on recent advances in synthesis, properties and applications. *RSC advances*, ***11***, 5659-5697.

[7] **Li, Y.** (2015). Conducting polymers. In *Organic optoelectronic materials* (pp. 23-50). Cham: Springer International Publishing.

[8] **Rasmussen, S. C**. (2019). Early history of Conjugated Poly-mers: From their Origins to the Handbook of Conducting Polymers. In J. R. Reynolds, T. A. Skotheim, B. Thompson (Eds.), *Handbook of Conducting Polymers, (*4th ed., pp.1-35).

[9] **Horowitz, G.** (2011). The organic transistor: state-of-the-art and outlook. *The European Physical Journal-Applied Physics*, ***53***, 33602.

[10] **Hoeben, F. J., Jonkheijm, P., Meijer, E. W., & Schenning, A. P.** (2005). About supramolecular assemblies of π-conjugated systems. *Chemical reviews*, ***105***, 1491-1546.

[11] **Hissler, M., Lescop, C., & Réau, R.** (2005). Organophosphorus π-conjugated materials: the rise of a new field. *Journal of Organometallic Chemistry*, ***690***, 2482-2487.

[12] **Picciani, P. H., Medeiros, E. S., Orts, W. J., & Mattoso, L. H.** (2011). Advances in electroactive electrospun nanofibers. In T. Lin (Ed.), Nanofibers-Production, Properties and Functional Applications, (pp. 85-116).

[13] **Scharber, M. C., & Sariciftci, N. S.** (2021). Low band gap conjugated semiconducting polymers. *Advanced Materials Technologies*, ***6***, 2000857.

[14] **Bundgaard, E., & Krebs, F. C.** (2007). Low band gap polymers for organic photovoltaics. *Solar Energy Materials and Solar Cells*, ***91***, 954-985.

[15] **Myers, J. D., & Xue, J.** (2012). Organic semiconductors and their applications in photovoltaic devices. *Polymer Reviews*, ***52***, 1-37.

[16] **Kim, K., Yoo, H., & Lee, E. K.** (2022). New Opportunities for Organic Semiconducting Polymers in Biomedical Applications. *Polymers*, ***14***, 2960.

[17] **Weis, M**. (2025). Organic Semiconducting Polymers in Photonic Devices: From Fundamental Properties to Emerging Applications. *Applied Sciences*, ***15***, 4028.

[18] **Hou, J., Park, M. H., Zhang, S., Yao, Y., Chen, L. M., Li, J. H., & Yang, Y**. (2008). Bandgap and molecular energy level control of conjugated polymer photovoltaic materials based on benzo [1,2-*b*:4,5-*b*′] dithiophene. *Macromolecules*, ***41***, 6012-6018.

[19] **Aihara, J. I.** (2005). Aromaticity and stability of furofurans and thienothiophenes. *Journal of Physical Organic Chemistry*, ***18***, 235-239.

[20] **Cinar, M. E., & Ozturk, T.** (2015). Thienothiophenes, dithienothiophenes, and thienoacenes: syntheses, oligomers, polymers, and properties. *Chemical Reviews*, ***115***, 3036-3140.

[21] **Zhou, B., Dai, T., Zhou, J., Chen, Y., Geng, Y., Lei, P., … Zhou, E.** (2024). Conjugated D–π–A photovoltaic polymers containing thieno[3,2-b]thiophene π-bridge. *Materials Chemistry Frontiers*, ***8***, 1563–1590.

[22] **Turkoglu, G., Cinar, M. E., & Ozturk, T.** (2017). Synthesis and Photophysical and Anion-Sensing Properties of Triarylborane-Substituted Cross-Conjugated and Conjugated Thienothiophenes. *European Journal of Organic Chemistry*, ***31***, 4552-4561.

[23] **Isci, R., Tekin, E., Kaya, K., Piravadili Mucur, S., Gorkem, S. F., & Ozturk, T.** (2020). Tetraphenylethylene substituted thienothiophene and dithienothiophene derivatives: synthesis, optical properties and OLED applications. *J. Mater. Chem. C*, ***8***, 7908–7915.

[24**] Isci, R., Gunturkun, D., Yalin, A. S., & Ozturk, T.** (2021). Copolymers of 4-thieno [3, 2-b] thiophen-3-ylbenzonitrile with anthracene and biphenyl; synthesis, characterization, electronic, optical, and thermal properties. *Journal of Polymer Science*, ***59***, 117-123.

[25] **Amna, B., Isci, R., Siddiqi, H. M., Majewski, L. A., Faraji, S., & Ozturk, T.** (2022). High-performance, low-voltage organic field-effect transistors using thieno[3,2-b]thiophene and benzothiadiazole co-polymers. *J. Mater. Chem. C*, ***10***, 8254–8265.

[26] **Gunturkun, D., Isci, R., Sütay, B., Majewski, L. A., Faraji, S., & Ozturk, T.** (2022). Copolymers of 3-arylthieno[3,2-b]thiophenes bearing different substituents: Synthesis, electronic, optical, sensor and memory properties. *European Polymer Journal*, ***170***, 111167

[27] **Isci, R., Balkan, T., Tafazoli, S., Sutay, B., Eroglu, M. S., & Ozturk, T.** (2022). Thienothiophene and triphenylbenzene based electroactive conjugated

porous polymer for oxygen reduction reaction (ORR). *ACS Applied Energy Materials*, ***5***, 13284-13292.

[28] **Isci, R., Wan, L., Topal, S., Gunturkun, D., Campbell, A. J., & Ozturk, T.** (2022). Solution-processable donor–π–acceptor type thieno[3,2-b]thiophene derivatives; synthesis, photophysical properties and applications. *J. Mater. Chem. C*, ***10***, 10719–10727.

[29] **Ozturk, S. E., Isci, R., Faraji, S., Sütay, B., Majewski, L. A., & Ozturk, T.** (2023). Synthesis, Photophysical properties and OFET application of thienothiophene and benzothiadiazole based Donor-π-Acceptor-π (D-π-A-π) type conjugated polymers. *European Polymer Journal*, ***191***, 112028.

[30] **Gunturkun, D., Isci, R., Faraji, S., Sütay, B., Majewski, L. A., & Ozturk, T.** (2023). Synthesis and characterization of naphthalenediimide-thienothiophene-conjugated polymers for OFET and OPT applications. *J. Mater. Chem. C*, ***11***, 13129–13141.

[31] **Suerkan, A., Isci, R., Ozturk, T., & Yagci, Y.** (2023). Cationic and radical polymerization using a boron-thienothiophene-triphenylamine based D-π-A type photosensitizer under white LED irradiation. *Molecular Systems Design and Engineering*, ***8***, 1319-1326.

[32] **Isci, R., & Ozturk, T**. (2023). A multifunctional thienothiophene member: 4-thieno[3,2-b]thiophen-3-ylbenzonitrile (4-CNPhTT). *TURKISH JOURNAL OF CHEMISTRY*, ***47***, 1239–1248.

[33] **Isci, R., & Ozturk, T.** (2023). Thienothiophene-based organic light-emitting diode: synthesis, photophysical properties and application. *Beilstein Journal of Organic Chemistry*, ***19***, 1849–1857

[34] **Isci, R., Gencosman, E., Yagci, Y., & Ozturk, T.** (2024). Thienothiophene and biphenyl based conjugated porous polymer as a photocatalyst for visible light induced free radical and cationic polymerization. *Journal of Photochemistry and Photobiology A: Chemistry*, ***449***, 115427.

[35] **Melucci, M., Frère, P., Allain, M., Levillain, E., Barbarella, G., & Roncali, J.** (2007). Molecular engineering of hybrid π-conjugated oligomers combining 3, 4-ethylenedioxythiophene (EDOT) and thiophene-S, S-dioxide units. *Tetrahedron*, ***63***, 9774-9783.

[36] **Mo, D., Zhang, J., Deng, K., & Chao, P.** (2025). Unraveling the monomer conjugation length effect on the optoelectronic performances of thiophene-EDOT hybrid electrochromic polymers. *Polymer*, ***319***, 127999.

[37] **Pepitone, M. F., Hardaker, S. S., & Gregory, R. V.** (2003). Synthesis and characterization of photoluminescent 3, 4-ethylenedioxythiophene derivatives. *Chemistry of Materials*, ***15***, 557-563.

[38] **Carbas, B. B., Özbakır, S., & Kaya, Y.** (2023). A comprehensive overview of carbazole-EDOT based electrochromic copolymers: A new candidate for carbazole-EDOT based electrochromic copolymer. *Synthetic Metals*, ***293***, 117298.

[39] **Bendrea, A.-D., Cianga, L., Ailiesei, G.-L., Ursu, E.-L., Göen Colak, D., & Cianga, I.** (2021). 3,4-Ethylenedioxythiophene (EDOT) End-Group Functionalized Poly-ε-caprolactone (PCL): Self-Assembly in Organic Solvents and Its Coincidentally Observed Peculiar Behavior in Thin Film and Protonated Media. *Polymers*, ***13***, 2720.

[40] **Turbiez, M., Frère, P., Allain, M., Videlot, C., Ackermann, J., & Roncali, J.** (2005). Design of organic semiconductors: Tuning the electronic properties of π-conjugated oligothiophenes with the 3, 4-ethylenedioxythiophene (EDOT) building block. *Chemistry–A European Journal*, ***11***, 3742-3752.

[41] **Kothavale, S., & Sekar, N.** (2017). Methoxy supported, deep red emitting mono, bis and tris triphenylamine-isophorone based styryl colorants: Synthesis, photophysical properties, ICT, TICT emission and viscosity sensitivity. *Dyes and Pigments*, ***136***, 116-130.

[42] **Kim, S. H., Choi, J., Sakong, C., Namgoong, J. W., Lee, W., Kim, D. H., ... & Kim, J. P.** (2015). The effect of the number, position, and shape of methoxy groups in triphenylamine donors on the performance of dye-sensitized solar cells. *Dyes and Pigments*, ***113***, 390-401.

[43] **Isci, R., Rahimi Varzeghani, A., Kaya, K., Sutay, B., Tekin, E., & Ozturk, T.** (2022). Triphenylamine/tetraphenylethylene substituted 4-thieno [3, 2-b] thiophen-3-ylbenzonitriles: synthesis, photophysical-electronic properties, and applications. *ACS Sustainable Chemistry & Engineering*, ***10***, 1605-1615.

[44] **Isci, R., Unal, M., Kucukcakir, G., Gurbuz, N. A., Gorkem, S. F., & Ozturk, T.** (2021). Triphenylamine/4, 4′-dimethoxytriphenylamine-functionalized thieno [3, 2-b] thiophene fluorophores with a high quantum efficiency: synthesis and photophysical properties. *The Journal of Physical Chemistry B*, ***125***, 13309-13319.

[45**] Wang, J., Liu, K., Ma, L., & Zhan, X.** (2016). Triarylamine: versatile platform for organic, dye-sensitized, and perovskite solar cells. *Chemical Reviews*, ***116***, 14675-14725.

[46] **Safaei-Ghomi, J., & Akbarzadeh, Z**. (2014). A convenient and efficient synthesis of triarylamine derivatives using CuI nanoparticles. *RSC Advances*, ***4***, 16385-16390.

[47] **Cheng, Y. J., Yang, S. H., & Hsu, C. S.** (2009). Synthesis of conjugated polymers for organic solar cell applications. *Chemical Reviews*, ***109***, 5868-5923.

[48] **Wöhrle, D., & Meissner, D.** (1991). Organic Solar Cells. *Advanced Materials*, ***3***, 129–138.

[49] **Hu, Z., Wang, J., Ma, X., Gao, J., Xu, C., Yang, K., ... & Zhang, F.** (2020). A critical review on semitransparent organic solar cells. *Nano Energy*, ***78***, 105376.

[50] **Liu, B., Qin, J., Luo, Q., and Ma, C.-Q.** (2025). Multifunctional interface engineering enables efficient and stable inverted organic photovoltaics. *Nature Communications*, ***16***.

[51] **Vivek, K., & Agrawal, G.** (2014). Organic Solar Cells: Principles, Mechanism and Recent Developments. *Hypothesis*, ***17***, 18.

[52] **Geffroy, B., Le Roy, P., & Prat, C.** (2006). Organic light-emitting diode (OLED) technology: materials, devices and display technologies. *Polymer International*, ***55***, 572-582.

[53] **Karzazi, Y.** (2014). Organic light emitting diodes: Devices and applications. *J. Mater. Environ. Sci*, ***5***, 1-12.

[54] **Horowitz, G.** (1998). Organic Field-Effect Transistors. *Advanced Materials*, ***10***, 365–377.

[55] **Chauhan, A. K., Jha, P., Aswal, D. K., & Yakhmi, J. V.** (2022). Organic Devices: Fabrication, Applications, and Challenges. *Journal of Electronic Materials*, ***51***, 447–485.

[56] **Lamport, Z. A., Haneef, H. F., Anand, S., Waldrip, M., & Jurchescu, O. D.** (2018). Tutorial: Organic field-effect transistors: Materials, structure and operation. *Journal of Applied Physics*, ***124***.

[57] **Lee, J. S. M., & Cooper, A. I**. (2020). Advances in conjugated microporous polymers. *Chemical Reviews*, ***120***, 2171-2214.

[58] **Thommes, M., Kaneko, K., Neimark, A. V., Olivier, J. P., Rodriguez-Reinoso, F., Rouquerol, J., & Sing, K. S.** (2015). Physisorption of gases, with special reference to the evaluation of surface area and pore size distribution (IUPAC Technical Report). *Pure and Applied Chemistry*, ***87***, 1051-1069.

[59] **Unal, M., Isci, R., Demirtas, I., Ertas, E., Matsuda, W., Ji, S., Tanaka, T., Tsutsui, Y., Seki, S., & Ozturk, T.** (2025). Impact of Doping on Charge Transport Properties in Thienothiophene-Based Organic Porous Polymers. *Macromolecular Materials and Engineering*.

[60] **Unal, M., Isci, R., Demirtas, I., Ertas, E., Paitandi, R. P., Matsuda, W., Seki, S., & Ozturk, T.** (2025). Thienothiophene-Based Organic Porous Polymers Combining Different Linkers and Functional Groups: Design, Synthesis, Photophysical, and Charge Transport Properties. *Asian Journal of Organic Chemistry*.

[61] **Mohamed, M. G., El-Mahdy, A. F. M., Kotp, M. G., & Kuo, S.-W.** (2022). Advances in porous organic polymers: syntheses, structures, and diverse applications. *Materials Advances*, ***3***, 707–733.

[62] **Zhang, T., Xing, G., Chen, W., & Chen, L**. (2020). Porous organic polymers: a promising platform for efficient photocatalysis. *Materials Chemistry Frontiers*, ***4***, 332–353.

[63] **Mohamed, M. G., Atayde Jr, E. C., Matsagar, B. M., Na, J., Yamauchi, Y., Wu, K. C. W., & Kuo, S. W.** (2020). Construction hierarchically mesoporous/microporous materials based on block copolymer and covalent organic framework. *Journal of the Taiwan Institute of Chemical Engineers*, ***112***, 180-192.

[64] **Pandolfo, T., Ruiz, V., Sivakkumar, S., & Nerkar, J.** (2013). General properties of electrochemical capacitors. In Beguin, F. & Frackowiak, E.

(Eds.) *Supercapacitors: materials, systems, and applications*. Wiley-VCH, (pp. 69-109).

[65] **Kar, K. K.** (2020). Handbook of nanocomposite supercapacitor materials II (Vol. 302). Cham: Springer International Publishing.

[66] **Kim, B. K., Sy, S., Yu, A., & Zhang, J.** (2015). Electrochemical supercapacitors for energy storage and conversion. In Handbook of clean energy systems, (pp. 1-25).

[67] **Tsai, K. J., Ni, C. S., Chen, H. Y., & Huang, J. H.** (2020). Single-walled carbon nanotubes/Ni–Co–Mn layered double hydroxide nanohybrids as electrode materials for high-performance hybrid energy storage devices. *Journal of Power Sources*, ***454***, 227912.

[68] **Zhang, S., & Pan, N.** (2015). Supercapacitors performance evaluation. *Advanced Energy Materials*, ***5***, 1401401.

[69] **Pan, H., Li, J., & Feng, Y.** (2010). Carbon nanotubes for supercapacitor. *Nanoscale Research Letters*, ***5***, 654.

[70] **Chen, S., Xing, W., Duan, J., Hu, X., & Qiao, S. Z.** (2013). Nanostructured morphology control for efficient supercapacitor electrodes. *Journal of Materials Chemistry A*, ***1***, 2941-2954.

[71] **Zhu, Z., Garcia-Gancedo, L., Flewitt, A. J., Xie, H., Moussy, F., & Milne, W. I.** (2012). A critical review of glucose biosensors based on carbon nanomaterials: carbon nanotubes and graphene. *Sensors*, ***12***, 5996-6022.

[72] **Hiralal, P., Wang, H., Unalan, H. E., Liu, Y., Rouvala, M., Wei, D., ... & Amaratunga, G. A.** (2011). Enhanced supercapacitors from hierarchical carbon nanotube and nanohorn architectures. *Journal of Materials Chemistry*, ***21***, 17810-17815.

[73] **Zhong, M., Zhang, M., & Li, X.** (2022). Carbon nanomaterials and their composites for supercapacitors. *Carbon Energy*, ***4***, 950–985.

[74] **Zhu, S., Ni, J., & Li, Y.** (2020). Carbon nanotube-based electrodes for flexible supercapacitors. *Nano Research*, ***13***, 1825-1841.

[75] **Iqbal, S., Khatoon, H., Pandit, A. H., & Ahmad, S.** (2019). Recent development of carbon based materials for energy storage devices. *Materials Science for Energy Technologies*, ***2***, 417-428.

[76] **Zhao, Y. L., & Stoddart, J. F.** (2009). Noncovalent functionalization of single-walled carbon nanotubes. *Accounts of Chemical Research*, ***42***, 1161-1171.

[77] **Goldmann, E., Górski, M., & Klemczak, B.** (2021). Recent Advancements in Carbon Nano-Infused Cementitious Composites. *Materials*, ***14***, 5176

[78] **Sivaraman, P., Mishra, S. P., Potphode, D. D., Thakur, A. P., Shashidhara, K., Samui, A. B., & Bhattacharyya, A. R.** (2015). A supercapacitor based on longitudinal unzipping of multi-walled carbon nanotubes for high temperature application. *RSC Advances*, ***5***, 83546-83557.

[79] **Frackowiak, E., Delpeux, S., Jurewicz, K., Szostak, K., Cazorla-Amoros, D., & Beguin, F.** (2002). Enhanced capacitance of carbon nanotubes through chemical activation. *Chemical Physics Letters*, ***361***, 35-41.

[80] **Gupta, V., & Miura, N. (**2006). Influence of the microstructure on the supercapacitive behavior of polyaniline/single-wall carbon nanotube composites. *Journal of Power Sources*, ***157***, 616-620.

[81] **Jeon, I. Y., Chang, D. W., Kumar, N. A., & Baek, J. B.** (2011). Functionalization of carbon nanotubes. In Yellampalli, S. (Ed.) *Carbon Nanotubes-Polymer Nanocomposites*, ***6***, 91-110.

[82] **Georgakilas, V., Tiwari, J. N., Kemp, K. C., Perman, J. A., Bourlinos, A. B., Kim, K. S., & Zboril, R.** (2016). Noncovalent functionalization of graphene and graphene oxide for energy materials, biosensing, catalytic, and biomedical applications. *Chemical Reviews*, ***116***, 5464-5519.

[83] **Norizan, M. N., Moklis, M. H., Demon, S. Z. N., Halim, N. A., Samsuri, A., Mohamad, I. S., ... & Abdullah, N.** (2020). Carbon nanotubes: Functionalisation and their application in chemical sensors. *RSC Advances*, ***10***, 43704-43732.

[84] **Choi, E. Y., Choi, L. W., & Kim, C. K.** (2015). Noncovalent functionalization of multi-walled carbon nanotubes with hydroxyl group-containing pyrene derivatives for their composites with polycarbonate. *Carbon*, ***95***, 91-99.

[85] **Di Crescenzo, A., Ettorre, V., & Fontana, A.** (2014). Non-covalent and reversible functionalization of carbon nanotubes. *Beilstein journal of nanotechnology*, ***5***, 1675-1690.

[86] **Devendar, P., Qu, R. Y., Kang, W. M., He, B., & Yang, G. F.** (2018). Palladium-catalyzed cross-coupling reactions: a powerful tool for the synthesis of agrochemicals. *Journal of Agricultural and Food Chemistry*, ***66***, 8914-8934.

[87] **Campeau, L. C., & Hazari, N.** (2018). Cross-coupling and related reactions: connecting past success to the development of new reactions for the future. *Organometallics*, ***38***, 3-35.

[88] **Nicolaou, K. C., Bulger, P. G., & Sarlah, D**. (2005). Palladium-catalyzed cross-coupling reactions in total synthesis. *Angewandte Chemie International Edition*, *44*, 4442-4489.

[89] **Nolan, S. P., & Navarro, O.** (2007). CC bond formation by cross-coupling. *Comprehensive Organometallic Chemistry III*, ***11***, 1-38.

[90] **Mohd Yusof Chan, N. N., Idris, A., Zainal Abidin, Z. H., Tajuddin, H. A., & Abdullah, Z**. (2021). White light employing luminescent engineered large (mega) Stokes shift molecules: a review. *RSC Advances*, ***11***, 13409–13445.

[91] **Suresha, S., Shilpa, G. M., Vijayalakshmi, A. R., Prabhala, P., Alsuhaibani, A. M., Refat, M. S., & Thippeswamy, M. S.** (2025). Photophysical Studies on Quinoline-Substituted Oxazole Analogues for

Optoelectronic Application: An Experimental and DFT Approach. *Journal of Electronic Materials*, ***54***, 5574–5587.

[92] **Isci, R., Donmez, K. B., Karatepe, N., & Ozturk, T.** (2024). High-Performance Thienothiophene and Single Wall Carbon Nanotube-Based Supercapacitor as a Free-Standing and Flexible Hybrid Energy Storage Material. *ACS Applied Energy Materials*, ***7***, 1488–1494

[93] **Isci, R., Baysak, E., Kesan, G., Minofar, B., Eroglu, M. S., Duygulu, O., Gorkem, S. F., & Ozturk, T.** (2022). Non-covalent modification of single wall carbon nanotubes (SWCNTs) by thienothiophene derivatives. *Nanoscale*, ***14***, 16602–16610.

[94] **Raju, G. S. R., Pavitra, E., Nagaraju, G., Sekhar, S. C., Ghoreishian, S. M., Kwak, C. H., ... & Han, Y. K.** (2018). Rational design of forest-like nickel sulfide hierarchical architectures with ultrahigh areal capacity as a binder-free cathode material for hybrid supercapacitors. *Journal of Materials Chemistry A*, **6**, 13178-13190.

[95] **Long, H., Zeng, W., Wang, H., Qian, M., Liang, Y., & Wang, Z.** (2018). Self-assembled biomolecular 1D nanostructures for aqueous sodium-ion battery. *Advanced Science*, ***5***, 1700634.

[96] **Lima, N., Baptista, A. C., Faustino, B. M. M., Taborda, S., Marques, A., & Ferreira, I**. (2020). Carbon threads sweat-based supercapacitors for electronic textiles. *Scientific Reports*, ***10***.

[97] **Chakrabarti, B. K., Dönmez, K. B., Çobandede, Z., & Low, C. T. J.** (2024). Practical Pouch Cell Supercapacitor Electrodes by Electrophoretic Deposition of Activated Carbon on Nickel Foam. *Chemelectrochem*, ***11***.

[98] **Diantoro, M., Istiqomah, I., Fath, Y. A., Mufti, N., Nasikhudin, N., Meevasana, W., & Alias, Y. B.** (2022). Hierarchical Activated Carbon–MnO2 Composite for Wide Potential Window Asymmetric Supercapacitor Devices in Organic Electrolyte. *Micromachines*, ***13***, 1989.

[99] **Aderyani, S., Flouda, P., Shah, S. A., Green, M. J., Lutkenhaus, J. L., & Ardebili, H.** (2021). Simulation of cyclic voltammetry in structural supercapacitors with pseudocapacitance behavior. *Electrochimica Acta*, ***390***, 138822.

[100] **Cao, X. M., Sun, Z. J., Zhao, S. Y., Wang, B., & Han, Z. B.** (2018). MOF-derived sponge-like hierarchical porous carbon for flexible all-solid-state supercapacitors. *Materials Chemistry Frontiers*, ***2***, 1692-1699.

[101] **Chen, X. Y., Chen, C., Zhang, Z. J., Xie, D. H., & Liu, J. W.** (2013). A general conversion of polyacrylate–metal complexes into porous carbons especially evinced in the case of magnesium polyacrylate. *Journal of Materials Chemistry A*, ***1***, 4017-4025.

[102] **Gateman, S. M., Gharbi, O., De Melo, H. G., Ngo, K., Turmine, M., & Vivier, V.** (2022). On the use of a constant phase element (CPE) in electrochemistry. *Current Opinion in Electrochemistry*, ***36***, 101133.

[103] **Lin, R., Li, Z., Abou El Amaiem, D. I., Zhang, B., Brett, D. J., He, G., & Parkin, I. P.** (2017). A general method for boosting the supercapacitor performance of graphitic carbon nitride/graphene hybrids. *Journal of Materials Chemistry A*, ***5***, 25545-25554.

[104] **Wang, W., Guo, S., Lee, I., Ahmed, K., Zhong, J., Favors, Z., ... & Ozkan, C. S.** (2014). Hydrous ruthenium oxide nanoparticles anchored to graphene and carbon nanotube hybrid foam for supercapacitors. *Scientific Reports*, ***4***, 4452.

[105] **Li, K. B., Shi, D. W., Cai, Z. Y., Zhang, G. L., Huang, Q. A., Liu, D., & Yang, C. P.** (2015). Studies on the equivalent serial resistance of carbon supercapacitor. *Electrochimica Acta*, ***174***, 596-600.

[106] **Famili, M., Grace, I. M., Al-Galiby, Q., Sadeghi, H., & Lambert, C. J.** (2018). Toward High Thermoelectric Performance of Thiophene and Ethylenedioxythiophene (EDOT) Molecular Wires. *Advanced Functional Materials*, ***28***, 1703135.

[107] **Roncali, J., Blanchard, P., & Frère, P.** (2005). 3, 4-Ethylenedioxythiophene (EDOT) as a versatile building block for advanced functional π-conjugated systems. *Journal of Materials Chemistry*, ***15***, 1589-1610.

[108] **Spencer, H. J., Skabara, P. J., Giles, M., McCulloch, I., Coles, S. J., & Hursthouse, M. B.** (2005). The first direct experimental comparison between the hugely contrasting properties of PEDOT and the all-sulfur analogue PEDTT by analogy with well-defined EDTT–EDOT copolymers. *Journal of Materials Chemistry*, ***15***, 4783-4792.

[109] **Yu, J., Fu, N., Zhao, J., Liu, R., Li, F., Du, Y., & Yang, Z.** (2019). High specific capacitance electrode material for supercapacitors based on resin-derived nitrogen-doped porous carbons. *ACS Omega*, ***4***, 15904-15911.

[110] **Turksoy, F., Wallis, J. D., Tunca, U., & Ozturk, T.** (2003). An in depth study of the formation of new tetrathiafulvalene derivatives from 1, 8-diketones. *Tetrahedron*, ***59***, 8107-8116.

[111] **Wang, L., Ma, Y., Yang, M., & Qi, Y.** (2017). Titanium plate supported MoS2 nanosheet arrays for supercapacitor application. *Applied Surface Science*, ***396***, 1466-1471.

[112] **Bello, A., Barzegar, F., Momodu, D., Dangbegnon, J., Taghizadeh, F., & Manyala, N.** (2015). Symmetric supercapacitors based on porous 3D interconnected carbon framework. *Electrochimica Acta*, ***151***, 386-392.

[113] **Wang, Y., Chen, N., Liu, Y., Zhou, X., Pu, B., Qing, Y., ... & Yang, W.** (2022). MXene/Graphdiyne nanotube composite films for Free-Standing and flexible Solid-State supercapacitor. *Chemical Engineering Journal*, ***450***, 138398.

[114] **Chen, J., Xie, J., Jia, C. Q., Song, C., Hu, J., & Li, H.** (2022). Economical preparation of high-performance activated carbon fiber papers as self-supporting supercapacitor electrodes. *Chemical Engineering Journal*, ***450***, 137938.

[115] **Yanilmaz, M., Dirican, M., Asiri, A. M., & Zhang, X.** (2019). Flexible polyaniline-carbon nanofiber supercapacitor electrodes. *Journal of Energy Storage*, ***24***, 100766.

[116] **Yang, X., Lin, Z., Zheng, J., Huang, Y., Chen, B., Mai, Y., & Feng, X.** (2016). Facile template-free synthesis of vertically aligned polypyrrole nanosheets on nickel foams for flexible all-solid-state asymmetric supercapacitors. *Nanoscale*, ***8***, 8650–8657.

[117] **Xu, X., Wang, M., Liu, Y., Li, Y., Lu, T., & Pan, L.** (2016). In situ construction of carbon nanotubes/nitrogen-doped carbon polyhedra hybrids for supercapacitors. *Energy Storage Materials*, ***5***, 132-138.

[118] **Cheng, Y., Lu, S., Zhang, H., Varanasi, C. V., & Liu, J.** (2012). Synergistic effects from graphene and carbon nanotubes enable flexible and robust electrodes for high-performance supercapacitors. *Nano Letters*, ***12***, 4206-4211.

[119] **Li, M., Jiang, D., Du, Z., Yu, S., Ge, X., & He, Y.** (2023). Green modification of single-walled carbon nanotubes dispersion with good dispersibility and long storage stability. *Journal of Nanoparticle Research*, ***25***.

[120] **Clancy, A. J., White, E. R., Tay, H. H., Yau, H. C., & Shaffer, M. S.** (2016). Systematic comparison of conventional and reductive single-walled carbon nanotube purifications. *Carbon*, ***108***, 423-432.

[121] **Yu, H., Wu, J., Lin, J., Fan, L., Huang, M., Lin, Y., ... & Qiu, Z.** (2013). A Reversible Redox Strategy for SWCNT-Based Supercapacitors Using a High-Performance Electrolyte. *ChemPhysChem*, ***14***, 394-399.

[122] **Antiohos, D., Folkes, G., Sherrell, P., Ashraf, S., Wallace, G. G., Aitchison, P., ... & Minett, A. I.** (2011). Compositional effects of PEDOT-PSS/single walled carbon nanotube films on supercapacitor device performance. *Journal of Materials Chemistry*, ***21***, 15987-15994.

[123] **Yuksel, R., Sarioba, Z., Cirpan, A., Hiralal, P., & Unalan, H. E.** (2014). Transparent and flexible supercapacitors with single walled carbon nanotube thin film electrodes. *ACS Applied Materials & Interfaces*, ***6***, 15434-15439.

[124] ***Cheng, Q., Tang, J., Ma, J., Zhang, H., Shinya, N., & Qin, L. C.*** (2011). Graphene and carbon nanotube composite electrodes for supercapacitors with ultra-high energy density. *Physical Chemistry Chemical Physics*, ***13***, 17615-17624.

[125] **Xia, H., Hong, C., Li, B., Zhao, B., Lin, Z., Zheng, M., Savilov, S. V., & Aldoshin, S. M.** (2015). Facile Synthesis of Hematite Quantum-Dot/Functionalized Graphene-Sheet Composites as Advanced Anode Materials for Asymmetric Supercapacitors. *Advanced Functional Materials*, ***25***, 627–635.

[126] **Campbell, P. G., Merrill, M. D., Wood, B. C., Montalvo, E., Worsley, M. A., Baumann, T. F., & Biener, J.** (2014). Battery/supercapacitor hybrid via non-covalent functionalization of graphene macro-assemblies. *Journal of Materials Chemistry A*, ***2***, 17764-17770.

[127] **Zhang, Y., Zhang, H., Jiang, F., Zhou, W., Wang, R., Xu, J., Duan, X., Wu, Y., & Ding, Y.** (2020). Electrochemical assembly of homogenized poly(3,4-ethylenedioxythiophene methanol)/SWCNT nano-networks and their high performances for supercapacitor electrodes. *Ionics*, ***26***, 3631–3642.

[128] **Wu, G., Tan, P., Wang, D., Li, Z., Peng, L., Hu, Y., Wang, C., Zhu, W., Chen, S., & Chen, W.** (2017). High-performance Supercapacitors Based on Electrochemical-induced Vertical-aligned Carbon Nanotubes and Polyaniline Nanocomposite Electrodes. *Scientific Reports*, ***7***, 43676.

[129] **Yoon, J., Lee, J., & Hur, J.** (2018). Stretchable Supercapacitors Based on Carbon Nanotubes-Deposited Rubber Polymer Nanofibers Electrodes with High Tolerance against Strain. *Nanomaterials*, ***8***, 541**.**

APPENDICES

APPENDIX A: ^{1}H NMR characterizations of compounds.

APPENDIX B: Statement text.

APPENDIX A: ^{1}H NMR characterizations of compounds.

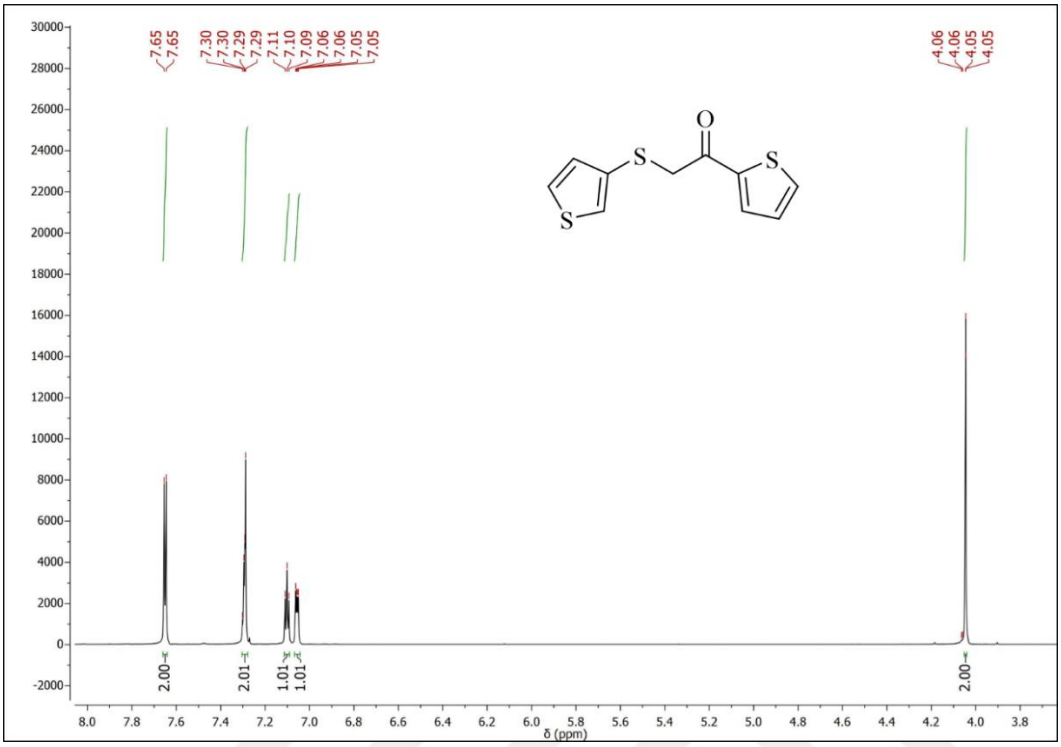

Figure A.1 : ^{1}H-NMR spectra of **3** in $CDCl_3$.

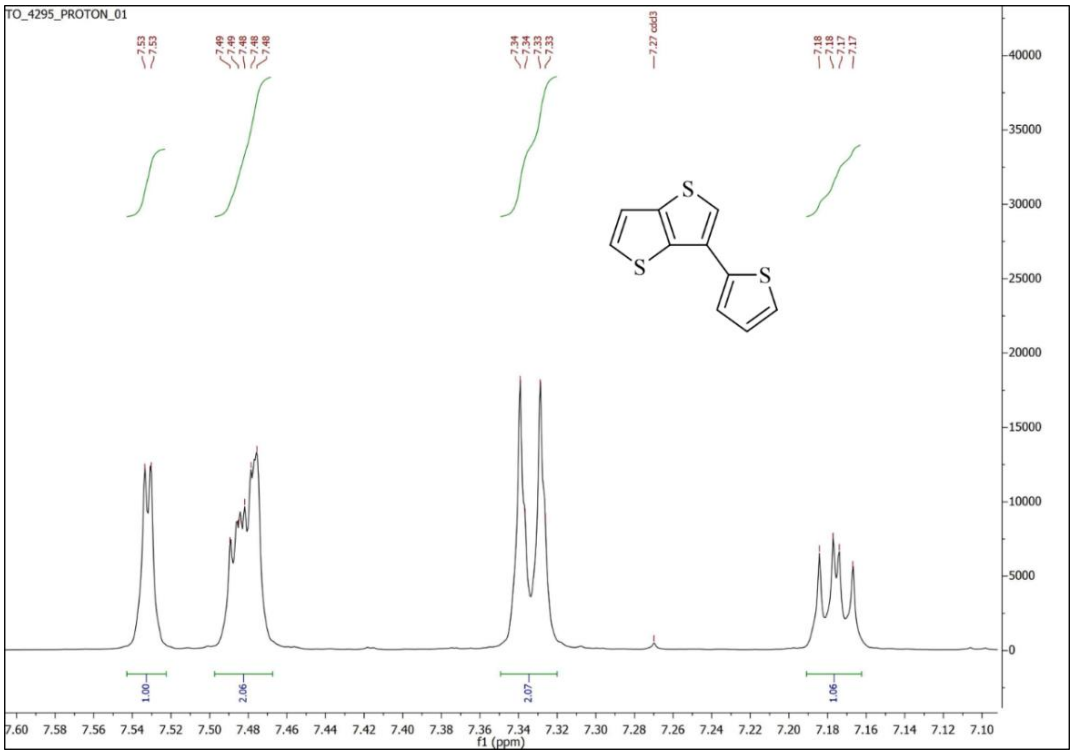

Figure A.2 : ^{1}H-NMR spectra of **4** in $CDCl_3$.

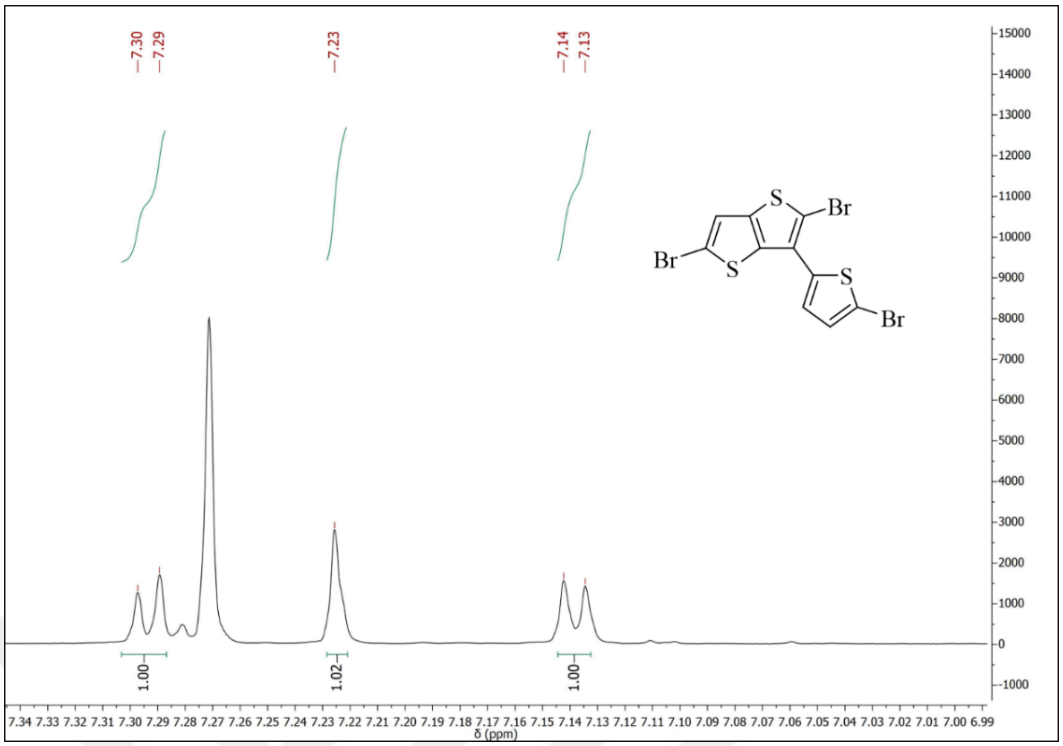

Figure A.3 : ^{1}H-NMR spectra of **5** in $CDCl_3$.

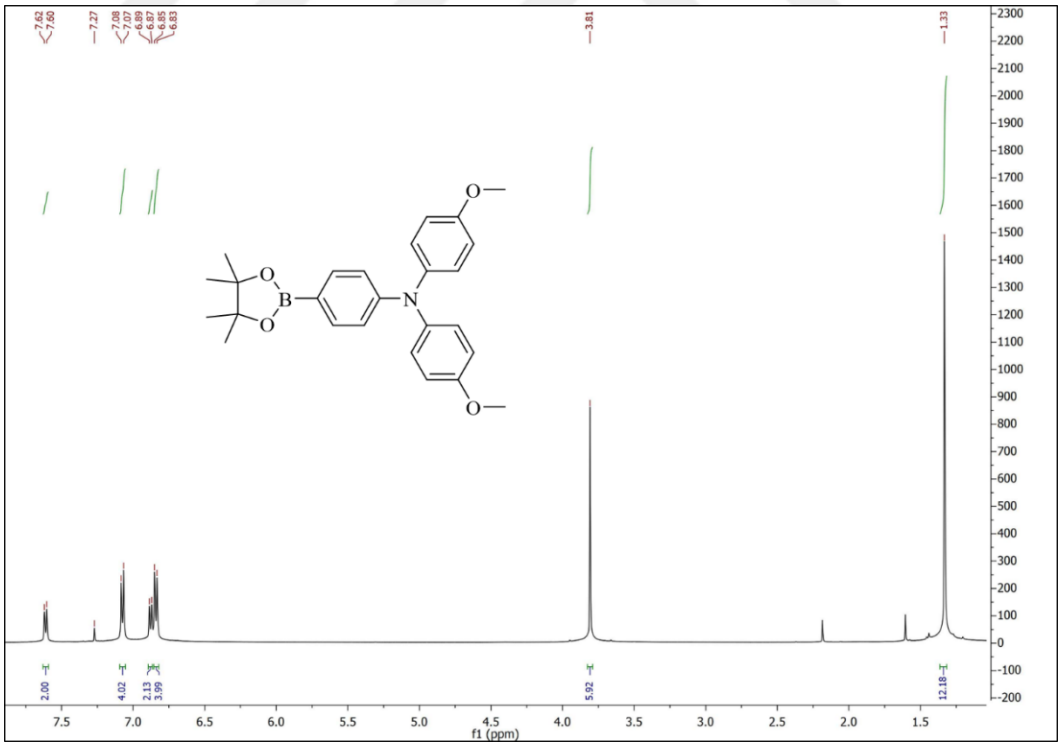

Figure A.4 : ^{1}H-NMR spectra of **7** in $CDCl_3$.

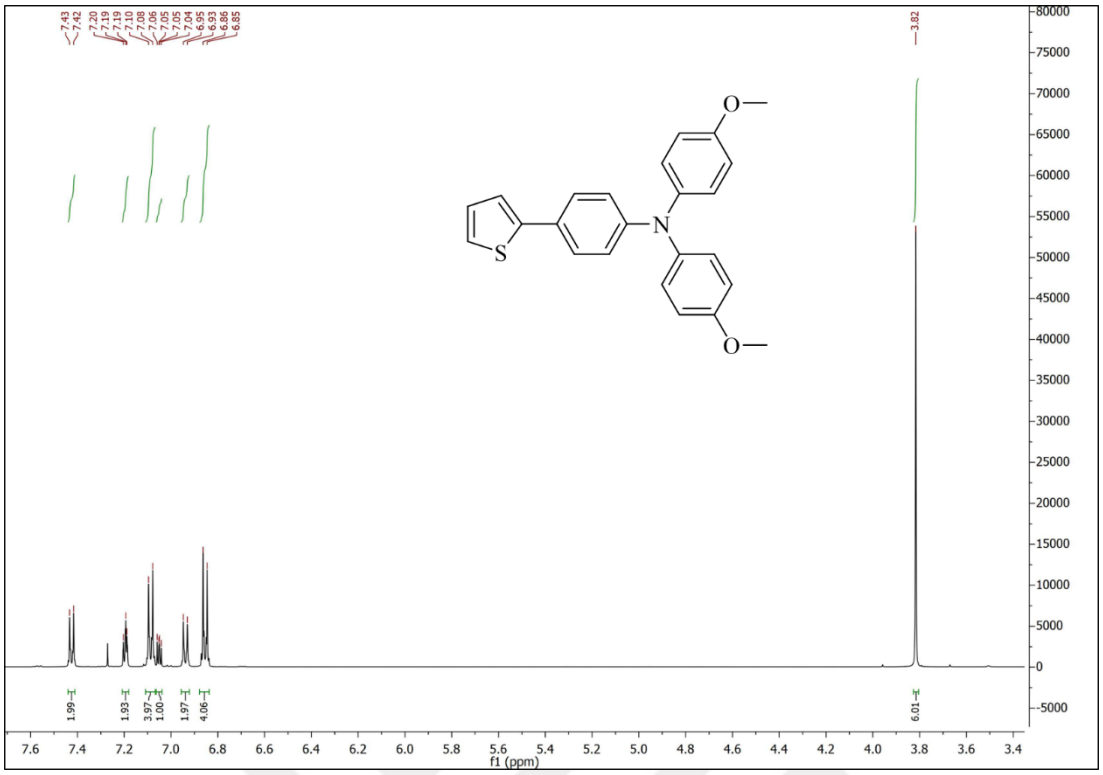

Figure A.5 : ^{1}H-NMR spectra of **9** in $CDCl_3$.

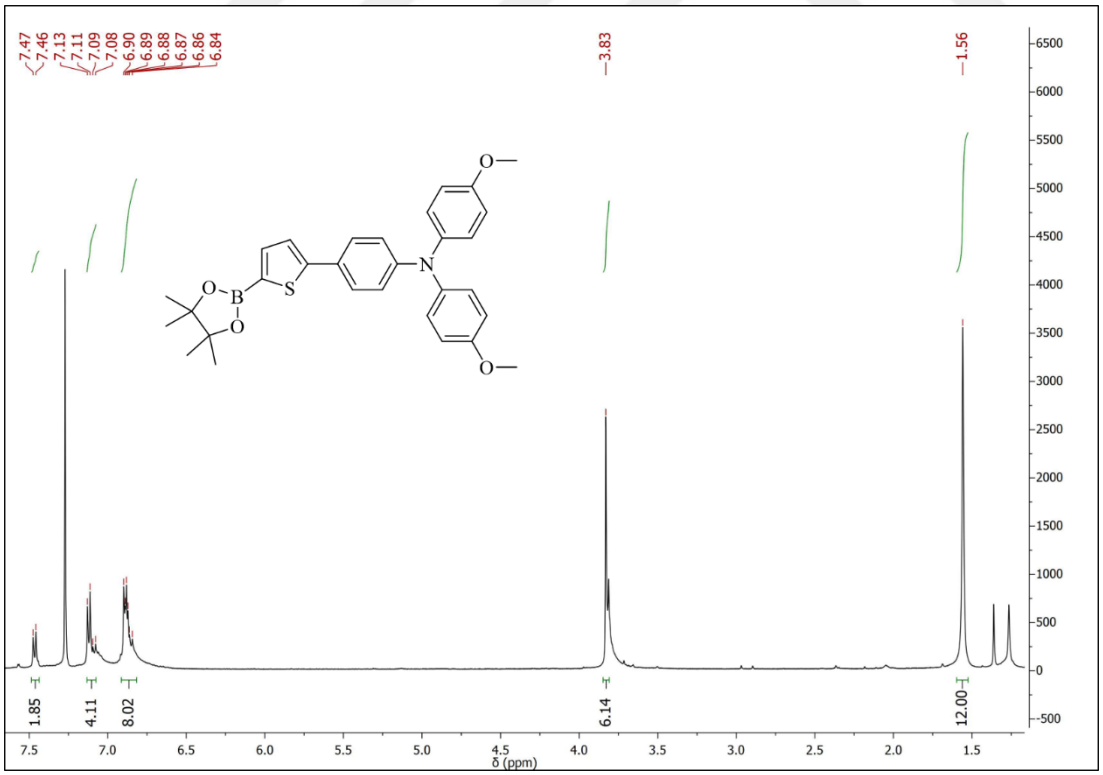

Figure A.6 : ^{1}H-NMR spectra of **10** in $CDCl_3$.

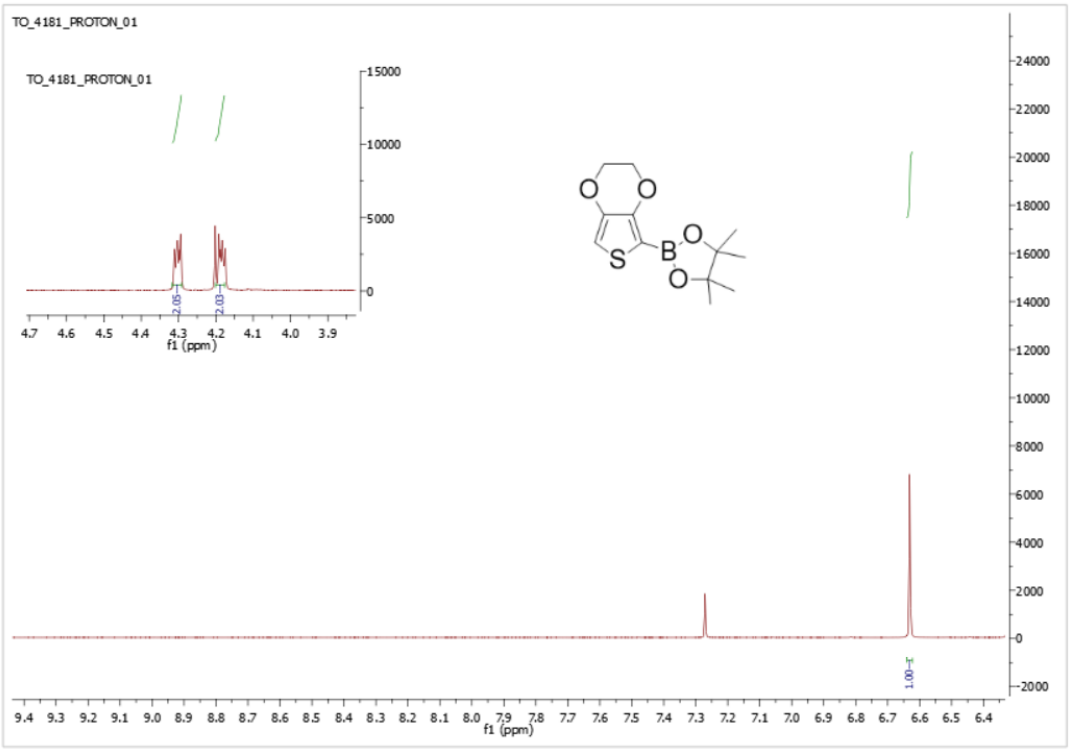

Figure A.7 : ^{1}H-NMR spectra of **12** in $CDCl_3$.

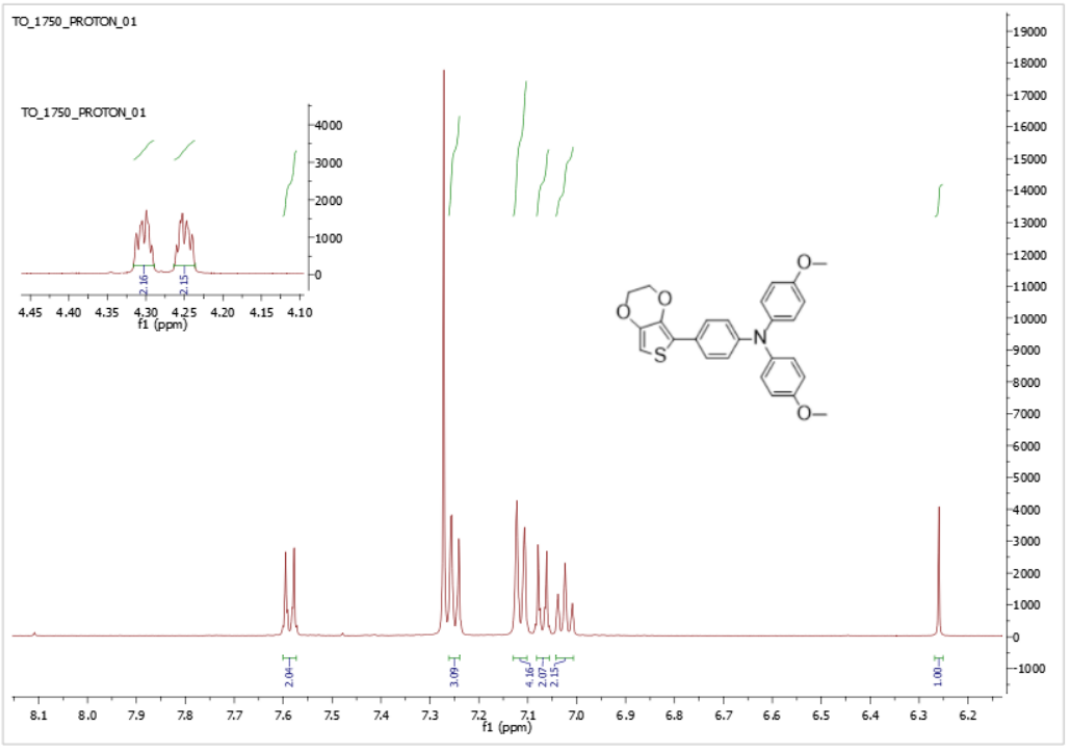

Figure A.8 : ^{1}H-NMR spectra of **13** in $CDCl_3$.

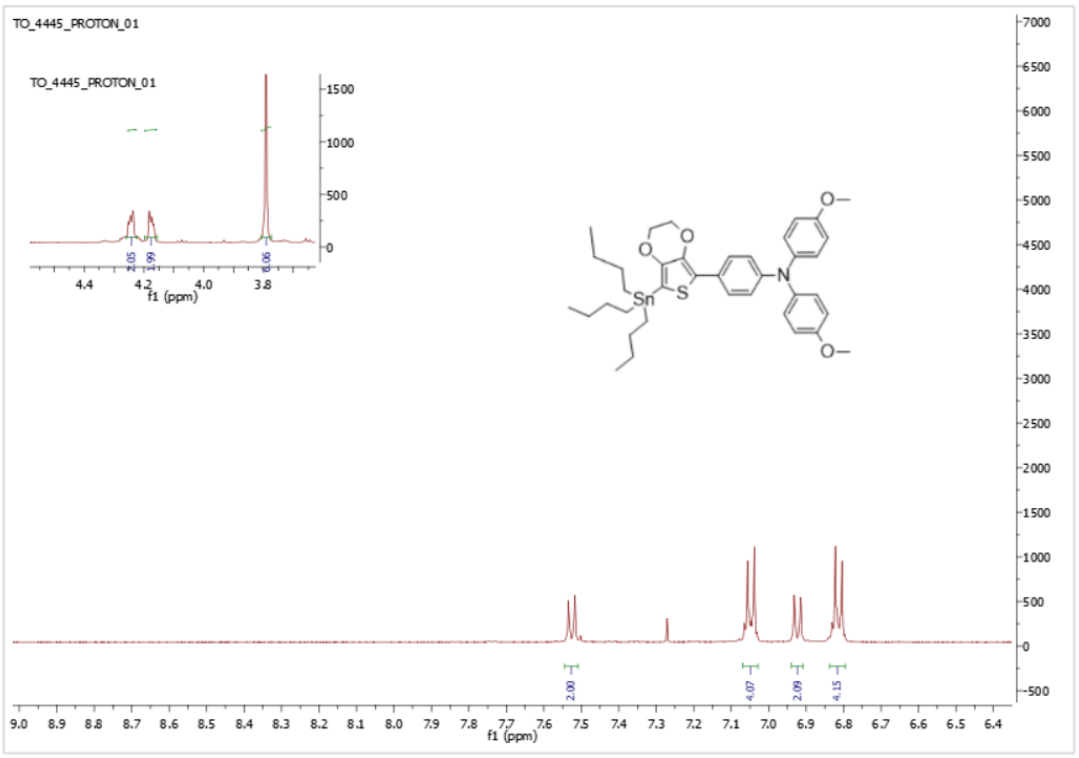

Figure A.9 : ^{1}H-NMR spectra of **14** in $CDCl_3$.

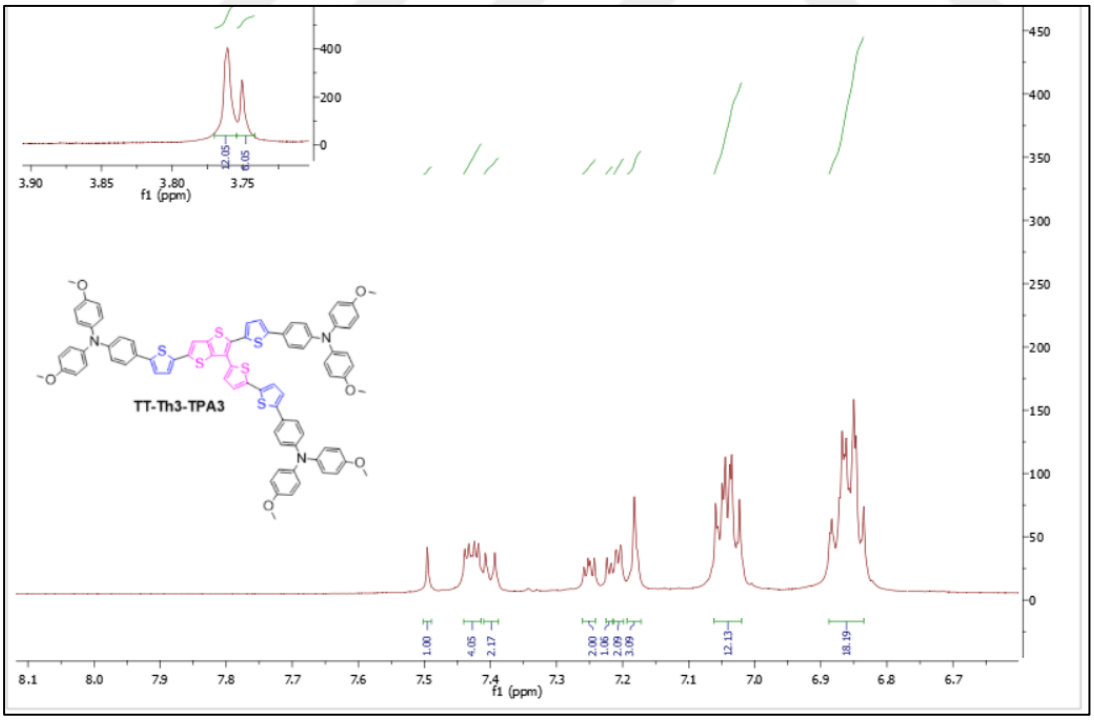

Figure A.10 : ^{1}H-NMR spectra of **TT-Th3-TPA3** in d_8-THF.

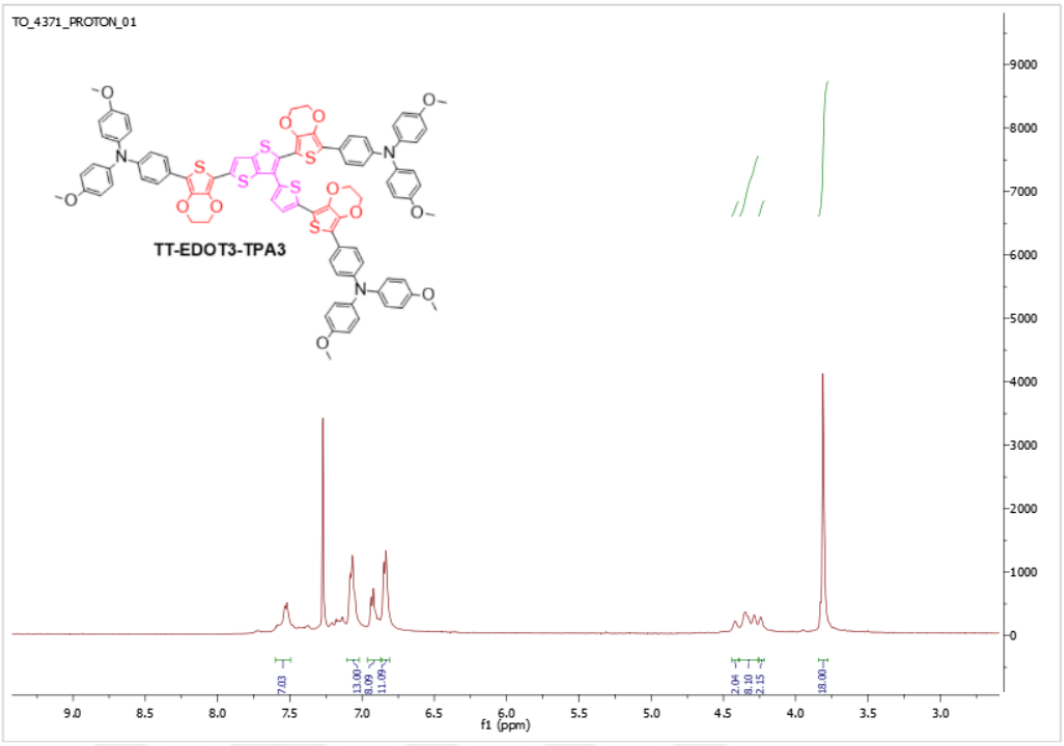

Figure A.11 : ^{1}H-NMR spectra of **TT-EDOT3-TPA3** in $CDCl_3$.

APPENDIX B : Statement text.

03.08.2025

To whom it may concern/Sayın ilgili

The topic I used in my thesis was given to me by my supervisor Prof. Dr. Turan Ozturk. At the end of my thesis, the substances that I synthesized in my MSc/PhD studies can be re-synthesized by others and used for other than the intended purpose in my thesis. I do not claim any rights for the substances used in this way. I accept that my name will neither be included as an author nor be acknowledged in any articles/patents/conferences etc. which are published using the re-synthesized compounds in my thesis other than the purposes specified in my thesis.

Also, taking into account the economic conditions of our country and the infrastructures of our universities. I accept that the spectroscopic data of the substances in my thesis can be used for substances that are re-synthesized and used for the purposes other than those in my thesis, and I accept that my name is not included in any future articles/patents/conferences etc. for the spectroscopic data used as indicated above.

Burada onaylıyorum ki tezimde kullandığım konu danışmanım Prof. Dr. Turan Öztürk tarafından bana verilmiştir. Tezim bitiminde, tez çalışmalarımda sentezlediğim maddeler başkaları tarafından tekrar sentezlenerek tezimde hedeflenen amaç dışında kullanılabilir. Bu şekilde kullanılan maddeler için hiç bir hak talep etmemekteyim. Tezimde belirlenen amaçlar dışında maddelerin kullanılarak çıkarılan makalelerde/patentlerde/konferanslarda vs yazar olarak adımın kullanılmamasını ve teşekkür edilmemesini kabul etmekteyim.

Ayrıca, ülkemiz ekonomik şartlarını ve üniversitelerimiz alt yapıları göz önüne alarak tezimdeki maddelerin spektroskopik datalarının, tekrar sentezlenen ve tezimdeki amaçlar dışında kullanılan maddeler için kullanılmasını kabul ediyorum ve çıkacak makalelerde/patentlerde/konferanslarda vs. adımın kullanılmamasını onaylıyorum.

Your truly/ Saygılarımla

Figure B.1 : Statement text.

CURRICULUM VITAE

Name Surname **: Esra ŞAHİN**

EDUCATION **:**

- **B.Sc.** **:** 2023, Istanbul Technical University, Faculty of Science and Letter, Chemistry Department
- **M.Sc.** **:** 2025, Istanbul Technical University, Graduate School, Chemistry Department

PROFESSIONAL EXPERIENCE AND REWARDS:

- ITU, BAP-MSc Thesis Project, (Project Number: TYLB-2023-45051), Istanbul. Project Name: Tiyenotiyofen Temelli Malzemelerin Sentezi Elektronik ve Optoelektronik Özelliklerinin İncelenmesi
- TUBITAK - 1003 (Project No: 222O472), Kocaeli.
  Project Name: Obtaining High Purity Value Added Basic Bioactive Compounds from Olive Oil Production Residues with National Chromatographic Filler

PUBLICATIONS, PRESENTATIONS AND PATENTS ON THE THESIS:

- "Synthesis and Photophysical Properties of Thienothiophene Derivative Material For Perovskite Solar Cells", **Esra Sahin**, Recep Iscı, Turan Ozturk, Poster: 19th Asian Chemical Congress, Istanbul Technical University, Istanbul, Turkiye, July 9-14, 2023.
- **Sahin, E.**, Isci, R., Donmez, K. B., Cobandede, Z, Eroglu, M. S., Ozturk, T. *Thienothiophene and Single-Wall Carbon Nanotube-Based Hybrid Materials: Design, Photophysical Properties and Constructing High-Performance Supercapacitors*, J. Mater. Chem. C, 2025, https://doi.org/10.1039/d5tc01766a

OTHER PUBLICATIONS, PRESENTATIONS AND PATENTS:

- Ganjehyan, K., **Sahin, E.**, Isci, R., Dastan, A., Erdogan, M. *Higly Conjugated Dibenzosuberenone-Dihydropyridazine Fluorophores: Design, Synthesis and Sensor Properties*, J. Photochem. Photobiol., A, 2025, Under Review.